Poster Session

-Poster Session-

The poster number with "S" is eligible for the Best Student Poster Award nomination.

P01 **Design study of beam injection and extraction at HiSOR-II Booster Synchrotron**

Daisuke Fujita[a], Miho Shimada[b,a], Hiroshi Miyauchi[b,a], Masahiro Katoh[a]

a Hiroshima University
b High Energy Accelerator Research Organization (KEK) , Japan

P02 **Design study of combined-function magnets for HiSOR-II storage ring**

Takaya Narai[a], Christian John[a], Miho Shimada[b,a], Hiroshi Miyauchi[b,a], Masahiro Katoh[a]

a Hiroshima University
b High Energy Accelerator Research Organization (KEK) , Japan

P03 **Experimental Study on Single Electron Storage at UVSOR-Ⅲ in 2025**

Y. Asai[a,d], M. Shimada[b,c], H. Miyauchi[b,c], T. Kaneyasu[d] and M. Katoh[a,c,d]

a Research Institute for Synchrotron Radiation Science (HiSOR), Hiroshima Univ., Japan
b High Energy Accelerator Research Organization (KEK)
c Research Institute for Synchrotron Radiation Science, Hiroshima University,Japan
d UVSOR Synchrotron Facility, Japan

P04 **Design Proposal of a VUV Undulator Beamline for HiSOR-II**

Masashi Arita, Kenya Shimada, Taichi Okuda, Hirofumi Namatame, and Masahiro Katoh

a HiSOR, Hiroshima University, Japan

P05S **Simulation and experimental studies on radiation generation in an electron storage ring**

Runa Murayama[a], Miho Shimada[b,a], Hirohi Miyauchi[b,a], Katoh Masahiro[a]

a Hiroshima University (HiSOR),Japan

b High Energy Accelerator Research Organization (KEK) ,Japan
Institute for Molecular Science, Japan

P06 **BeamCast - A new Operation Status Display System for the HiSOR storage Ring**

Christian John

a Hiroshima University / Research Institute for Synchrotron Radiation Science (HiSOR), Japan

P07 **Doping-Induced Evolution of the Electronic Band Structure in Ni-Doped PdSeTe**

Yogendra Kumar[a], Takahiro Onimaru[b], Yasuyuki Shimura[b], Shinichiro Ideta[a], Kenya Shimada[a]

a Research Institute for Synchrotron Radiation Science (HiSOR), Hiroshima University, Japan
b Graduate School of Advanced Science and Engineering, Hiroshima University, Japan

-Poster Session-

The poster number with "S" is eligible for the Best Student Poster Award nomination.

P08S ARPES Study of Pb Substitution at Bi Sites in Double-Layer Cuprate Bi2212

A. Higuchi[a], Y. Tsubota[b], Y. Miyai[b], S. Nakagawa[c], S. Ishida[d], K. Tanaka[e], H. Eisaki[d], T. Kashiwagi[c], M. Arita[f], S. Kumar[g], K. Shimada[a],[b,f,h,i], S.Ideta[a,b,f]

a Faculty of Science, Hiroshima University, Japan
b Graduate School of Advanced Science and Engineering, Hiroshima University, Japan
c Tsukuba University,Japan
d National Institute of Advanced Industrial Science and Technology (AIST), Japan
e UVSOR-Ⅲ Synchrotron, Institute for Molecular Science, Japan
f Hiroshima Syncrotron Radiation Center (HiSOR), Hiroshima University, Japan
*g Institute of Microelectronics (IME), Agency for Science, Technology and Research (A*STAR), Singapore*
h International Institute for Sustainability with Knotted Chiral Meta Matter (WPI-SKCM2), Japan
i Research Institute for Semiconductor Engineering, (RISE), Hiroshima Univ., Japan

P09S Electronic States in Electron-Doped High-Tc cuprate $Nd_{2-x}Ce_xCuO_4$ investigated by Angle-Resolved and Inverse Photoemission Spectroscopies

H. Yamaguchi[a], Y. Tsubota[a], Y. Miyai[a], M. Atira[b], H. Sato[a,b], D. Song[f], K. Tanaka[e], K. Shimada[a,b,c,d], S. Ideta[a,b]

a Graduate School of Advanced Science and Engineering, Hiroshima University, Japan
b Hiroshima Synchrotron Radiation Center (HiSOR), Hiroshima Univ., Japan
c Research Institute for Semiconductor Engineering, (RISE), Hiroshima Univ., Japan
d International Institute for Sustainability with Knotted Chiral Meta Matter (WPI-SKCM2), Japan
e UVSOR-Ⅲ Synchrotron, Institute for Molecular Science., Japan
f University of British Columbia,Vancouver, Canada

P10S Electronic structure of $TiFe_xS_2$ ($0 \leq x \leq 0.33$) studied by ARPES and XAS

K. Kimura[a], Y. Nakashima[a], Y. Tanimoto[a], Y. Murakami[b], H. Sato[c], M. Arita[c], S. Ideta[c], K. Shimada[c], M. Sawada[c], T. Bizen[d], M. Miyata[d], M. Koyano[d]

a Graduate School of Advanced Science and Engineering, Hiroshima University,, Japan
b Faculty of Science, Hiroshima University, Japan
c Hiroshima Research Institute for Synchrotron Radiation Science, Hiroshima University, Japan
d School of Materials Science, Japan Advanced Institute of Science and Technology, Japan

P11S pH Dependence of Aqueous C2-C4 Dicarboxylic Acids by Soft X-ray Absorption Spectroscopy

Risa Okada[a], Rikuya Adachi[a], Ryosuke Yamamura[a], Taiga Suenaga[a], Takashi Tokushima[b], Masaki Oura[c], Osamu Takahashi[d]

a Chemistry Program, Graduate School of Advanced Science and Engineering, Hiroshima University, Japan
b MAX IV Laboratory, Lund University, Sweden
c RIKEN SPring-8 Center , Japan
d Research Institute for Synchrotron Radiation Science, Hiroshima University, Japan

P12S Hydrogen Bonding Behavior in Response to Concentration Changes in Mixed Solutions of Water and Organic Compounds

Koki Ozeki[a] and Osamu Takahashi[b]

a Graduate School of Advanced Science and Engineering, Hiroshima University.
b Research Institute for Synchrotron Radiation Science, Hiroshima University.

-Poster Session-

The poster number with "S" is eligible for the Best Student Poster Award nomination.

P13 Development of a liquid-filled cell for HiSOR BL06

Misaki Kitajima[a], Yuka Horikawa[a],Hiroaki Yoshida[b], Takashi Tokushima[c] and Osamu Takahashi[d]

a Graduate School of Sciences and Technology for Innovation, Yamaguchi Univ. , Japan
b Graduate School of Advanced Science and Engineering, Hiroshima University,Japan
c MAX,IV Laboratory, Lund University , Sweden
d Research Institute for Synchrotron Radiation Science, Hiroshima University , Japan

P14S Thickness Dependence of Electronic Structure of Bi Thin Films on Au(111).

N. Nishimoto [a], H. Yamaguchi [b], T. Asano [b], Y. Fujisawa [c], K. Sumida [c], H. Sato [c], K. Miyamoto [c] and T. Okuda [c,d,e]

a Department of Physics, Faculty of Science, Hiroshima University, Japan
b Graduate School of Advanced Science and Engineering, Hiroshima University, Japan
c Research Institute for Synchrotron Radiation Science, Hiroshima University, Japan
d International Institute for Sustainability with Knotted Chiral Meta Matter (SKCM^2), Hiroshima University, Japan
e Research Institute for Semiconductor Engineering (RISE), Hiroshima University, Japan

P15 Substrate and Thickness Dependence of Anisotropic Topological Surface States of Bi_2Te_3 Thin Films

R. Yamamoto[a], Y. Fujisawa[b], K. Sumida[b], K. Miyamoto[b], and T. Okuda[b,c,d].

a Graduate School of Advanced Science and Engineering Hiroshima University, Japan
b Research Institute for Synchrotron Radiation Science (HiSOR), Hiroshima University, Japan
c International Institute for Sustainability with Knotted Chiral Meta Matter (WPI-SCKM2), Hiroshima University, Japan
d Research Institute for Semiconductor Engineering (RISE), Hiroshima University, Japan

P16S Development of Spin-ARPES for Electric-Field Response

T. Asano[a], Y. Fujisawa[b] K. Sumida[b], T. Okuda[b,c,d], K. Miyamoto[b]

a Graduate School of Advanced Science and Engineering, Hiroshima University, Japan.
b Research Institute for Synchrotron Radiation Science (HiSOR), Hiroshima University, Japan.
c International Institute for Sustainability with Knotted Chiral Meta Matter (SKCM2), Hiroshima University, Japan.
d Research Institute for Semiconductor Engineering (RISE), Hiroshima University, Japan

P17 VUV-CD Imaging of LLPS Proteins

Kentaro FUJII[a], Kuya AOYAMA[b], Nobuo MAITA[a], Masato KATO[a], Hideaki IWASAWA[c], Koichi MATSUO[b]

a Institute for Quantum Life Science, National Institutes for Quantum Science and Technology (QST)
b HiSOR, Hiroshima University
c Synchrotron Radiation Research center, National Institutes for Quantum Science and Technology (QST)

P18S Variation of Absorption Spectra of Aqueous DMSO Solutions Measured by the Ultraviolet-Attenuated Total Reflection Method

Chika Sugahara[a], Koichi Matsuo[a,b] and Kazumasa Okada[a,b]

a Graduate School of Advanced Science and Engineering, Hiroshima University, Japan
b Research Institute for Synchrotron Radiation Science, Hiroshima University, Japan

P19S Development of Vertical-Imaging Circular Dichroism Apparatus for Measuring Aggregated Samples

Kuya Aoyama[a], Satoshi Hashimoto[a], Mohamed Ibrahim[b], and Koichi Matsuo[a,b]

a Graduate School of Advanced Science and Engineering, Hiroshima University, Japan
b Research Institute for Synchrotron Radiation Science, Hiroshima University, Japan

-Poster Session-

The poster number with "S" is eligible for the Best Student Poster Award nomination.

P20S Dynamic Structural Study of the Antimicrobial Peptide Magainin 2 Interacting with Membranes by Time-Resolved Circular Dichroism Spectroscopy

Miu Yoshimura[a], Satoshi Hashimoto[b], and Koichi Matsuo[a,b]

a Graduate School of Advanced Science and Engineering, Hiroshima University, Japan
b Research Institute for Synchrotron Radiation Science, Hiroshima University, Japan

P21 Investigation of the Wrapping Mechanism of β-Lactoglobulin Around SDS Micelles by Time-Resolved VUVCD and Molecular Dynamics Simulation

Satoshi Hashimoto[a] and Koichi Matsuo[a,b,c]

a Research Institute for Synchrotron Radiation Science Hiroshima University, Japan.
b Graduate School of Advanced Science and Engineering, Hiroshima University. , Japan.
c International Institute for Sustainability with Knotted Chiral Meta Matter (WPI-SKCM²), Hiroshima University. , Japan.

P22 Tracking Calcium-Induced Assembly and Phase Transitions in Sodium Alginate via Circular Dichroism

Tatsuki Haga[a], Satoshi Hashimoto[a], Masaya Yoshida[b], Yudai Ono[b], Takeharu Haino[b], Yasuyuki Maki[c], Koichi Matsuo[a,d], Mohamed Ibrahim[d]

a Graduate School of Advanced Science and Engineering, Hiroshima University. , Japan.
b Department of Chemistry, Graduate School of Advanced Science and Engineering, Hiroshima University, Japan
c Faculty of Science, Kyushu University, Japan
d Research Institute for Synchrotron Radiation Science, HiSOR, Hiroshima University, Japan

P23S Separation and Chiroptical Detection of Biomolecules Using an LC-SRCD System: A Case Study on Amino Acid Profiling

Shunsuke Maeda[a], Satoshi Hashimoto[b], Koichi Matsuo[a,b,c], and Mohamed Ibrahim[b]

a Department of Physics, School of Science, Hiroshima University, Japan
b Research Institute for Synchrotron Radiation Science, HiSOR, Hiroshima University, Japan
c Graduate School of Advanced Science and Engineering, Hiroshima University, Japan

P24S NEXAFS-Study on Thermal Degradation of PM6:Y6 Organic Solar Cell Active Layers

Y. Hanaki[a], S. Wada[a,b] and T. Sekitani[a,b]

a Graduate School of Science and Engineering, Hiroshima University, Japan
b Research Institute for Synchrotron Radiation Science, Hiroshima University, Japan

P25 Order analysis of supported lipid bilayers on gold substrates by soft X-ray absorption spectroscopy

Yuri Ohura[a], Kakuto Yoshioka[a], Shogo Tendo[b], Hayate Inoue[a], Genki Hashimoto[a], and Shin-ichi Wada[a, c]

a Graduate School of Science and Engineering, Hiroshima University, Japan
b National Institute of Technology, Kochi College, Japan
c Research Institute for Synchrotron Radiation Science, Hiroshima University

-Poster Session-

The poster number with "S" is eligible for the Best Student Poster Award nomination.

P26S Position dependence in fluorine-substituted aromatic SAMs studied by X-ray photoemission and Auger electron spectroscopies

Hayate Inoue[a], Yuichiro Kodama[b], Yuri Ohura[a], Kakuto Yoshioka[a], Shogo Tendo[c], Akinobu Niozu[d], Shin-ichi Wada[a,b,e]

a Graduate School of Science and Engineering, Hiroshima University, Japan
b School of Science, Hiroshima University, Japan
c National Institute of Technology, Kochi College, Japan
d Graduate School of Humanities and Social Sciences, Hiroshima University, Japan

P27 Ion Irradiation Induced Frustrated Non-collinear Magnetism In Tetragonally Distorted Cobalt Manganites: Insights From X-Ray Magnetic Circular Dichroism

Aradhana Kumari[a], Masahiro Sawada[a], Vijay Raj Singh[b]

a Research Institute for Synchrotron Radiation Science, Hiroshima University, Japan

b Department of Physics, Central University of South Bihar, India

P28S Tunable competing optical excitation pathways in the topological surface states of Bi_2Te_3

Shin Yokoyama[a, b], Takahito Takeda[a, c], Nagi Suzuki[a], Takuma Iwata[a, b], Ping Zhou[d], Yogendra Kumar[e], Akio Kimura[a, b, f], Koji Miyamoto[e], Taichi Okuda[b, e, f], Mario Novak[g], Uwe Bovensiepen[d], and Kenta Kuroda[a, b, f]

a Graduate School of Advanced Science and Engineering Hiroshima University, Japan
*b International Institute for Sustainability with Knotted Chiral Meta Matter (*WPI- *SKCM2), Hiroshima University, Japan.*
c Department of Chemical System Engineering,The University of Tokyo, Japan
d Faculty of Physics and Center for Nanointegration (CENIDE),University of Duisburg-Essen,Germany
e Research Institute for Synchrotron Radiation Science (HiSOR), Hiroshima University, Japan

f Research Institute for Semiconductor Engineering, Japan

g Department of Physics, Faculty of Science, University of Zagreb, Croatia

P29S Development of Sub-100-fs Time-Resolved Spin-ARPES and Frequency-Domain Analysis of Electronic-Structure Modulation in BiTeBr

Nagi Suzuki[a], Shin Yokoyama[a,b], Ko Sasaki[a,b], Takuma Iwata[a,b], Akio Kimura[a,b,c], Koji Miyamoto[d], Taichi Okuda[b,c,d], Mario Novak[e], and Kenta Kuroda[a,b,c]

a Graduate School of Advanced Science and Engineering Hiroshima University, Japan
b nternational Institute for Sustainability with Knotted Chiral Meta Matter (SKCM2), Hiroshima University, Japan.
c Research Institute for Semiconductor Engineering, Japan.

d Research Institute for Synchrotron Radiation Science (HiSOR), Hiroshima University, Japan.
e Department of Physics, Faculty of Science, University of Zagreb, Croatia

-Poster Session-

The poster number with "S" is eligible for the Best Student Poster Award nomination.

P30 Present status of multi-channel spin detector development

Kazuki Sumida[a], Yuita Fujisawa[a], Koji Miyamoto[a], and Taichi Okuda[a,b,c]

a Research Institute for Synchrotron Radiation Science (HiSOR), Hiroshima University, Japan
b International Institute for Sustainability with Knotted Chiral Meta Matter (WPI-SKCM^2), Japan
c Research Institute for Semiconductor Engineering (RISE), Japan

P31S Observation of Antiferromagnetic Domains in the "Devil's Staircase" of CeSb using Polarizing Microscopy

K. Sasaki[a, b], T. Takeda[a], K. Watanabe[a], T. Iwata[a, b], A. Kimura[a, b, c], H. S. Suzuki[d], K. Kuroda[a, b, c]

a Graduate School of Advanced Science and Engineering, Hiroshima University, Japan
b International Institute for Sustainability with Knotted Chiral Meta Matter (WPI-SKCM2), Japan
c Research Institute for Semiconductor Engineering, Japan
d Institute for Solid State Physics, The University of Tokyo, Japan

P32S Parity-violating antiferromagnetic order leading to asymmetric electronic band structure in LaMnSi

T. Iwata[a], K. Shiraishi[a] , T. Aoyama[a], D. Senba[a], T. Takeda[a], c, Y. Fujisawa[d], M. Nurmamat[a] , K. Nakanishi[a], K. Yamagami[e] , Y. Yanagi[f], T. Yamada[f,] A. Kimura[a,b,g, h], H. Tanida[f], and K. Kuroda[a,b,h]

a Graduate School of Advanced Science and Engineering, Hiroshima University, Japan
b International Institute for Sustainability with Knotted Chiral Meta Matter (WPI-SKCM2), Japan
c Department of Electrical Engineering and Information Systems, The University of Tokyo, Japan
d Research Institute for Synchrotron Radiation Science, Hiroshima University, Japan
e Japan Synchrotron Radiation Research Institute (JASRI), Japan
f Liberal Arts and Sciences, Toyama Prefectural University, Japan
g Synchrotron Radiation Research Center, National Institutes for Quantum Science and Technology (QST), Japan
h Research Institute for Semiconductor Engineering (RISE), Hiroshima University, Japan

P33S Title of the presentation: 'Imaging of orbital angular momentum textures in Weyl semimetal using soft x-ray ARPES'

D. Senba[a], T. Iwata[a,b], K. Ideura[a], N. Suzuki[a], T. Kai[a], T. Takeda[c], K. Yamagami[d], A. Kimura[a,b,e], M. Novak[f], K. Kuroda[a,b,e]

a Graduate School of Advanced Science and Engineering, Hiroshima University, Japan
b International Institute for Sustainability with Knotted Chiral Meta Matter (WPI-SKCM2), Japan
c Department of Electrical Engineering and Information Systems, The University of Tokyo, Japan
d Japan Synchrotron Radiation Research Institute (JASRI), Japan
e Research Institute for Semiconductor Engineering, Japan
f Department of Physics, Faculty of Science, University of Zagreb, Croatia

P34S Theoretical Study on Decay Processes Following Core Excitation

Yuika Watari[a] and Osamu Takahashi[b]

a Graduate School of Advanced Science and Engineering, Hiroshima University
b Research Institute for Synchrotron Radiation Science, Hiroshima University

-Poster Session-

The poster number with "S" is eligible for the Best Student Poster Award nomination.

P35S Analysis of Hydration Structures in Inorganic Salt Solutions using Molecular Dynamics and Molecular Orbital Methods

Ayana Sato [a], Osamu Takahashi [b]

a Chemistry Program,Graduate School of Advanced Science and Engineering, Hiroshima University

b Research Institute for Synchrotron Radiation Science, Hiroshima University

P36S Semiclassical Kramers–Heisenberg Calculations of Soft X-ray Emission Spectroscopy at the First Resonant Excitation

Hikari Sato[a] and Osamu Takahashi[b]

a Graduate School of Advanced Science and Engineering, Hiroshima University
b Research Institute for Synchrotron Radiation Science, Hiroshima University

P37S The electronic structure of 18-crown-6/acetonitrile/metal salt observed by soft X-ray absorption spectroscopy

Yuki Shiro[a, b], Osamu Takahashi[c], Masaki Oura[b], Masanari Nagasaka[d, e] and Yuka Horikawa[a, b]

a Graduate School of Science and Technology for Innovation, Yamaguchi University, Japan
b RIKEN SPring-8 Center, Soft X-ray Spectroscopy Instrumentation Unit, Japan
c Research Institute for Synchrotron Radiation Science, Hiroshima University, Japan
d Institute for Molecular Science, Myodaiji, Japan
e Graduate Institute for Advanced Studies, SOKENDAI, Japan

P38S Synchrotron X-ray Studies on Structure and Electronic States of WO3 Thin Films for Electrochromic Application

Sakshi Tyagi[a], Asokan Kandasami[a], Senthil Kumar Muthusamy[b]

a School of Advanced Engineering, University of Petroleum and Energy Studies, Dehradun, Uttarakhand, India,
b CSIR- National Physical Laboratory, New Delhi, India

P39S Analysis of multiple bosonic couplings in the self-energy of the high-Tc cuprate superconductor $La_{2-x}Sr_xCuO_4$ using Bayesian inference

Rikito Saiki[a], Masaharu Nozaki[a], Gunwoo Kim[a], Daiki Ootsuki[b], Shun Katakami[c], Masato Okada[c], Teppei Yoshida[a]

a Graduate School of Human and Environmental Studies, Kyoto University,Japan
b Research Institute for Interdisciplinary Science, Okayama University,Japan
c Graduate School of Frontier Sciences, The University of Tokyo, Japan

P40S Electronic structure of the Mott–Hubbard compound $SrVO_3$ studied by resonant photoemission spectroscopy

Gunwoo Kim[a], Chihiro Inoue[a], Masaaki Higashino[a], Daiki Ootsuki[b], Hiroshi Kumigashira[c], Shigeki Miyasaka[d], and Teppei Yoshida[a]

a Graduate School of Human and Environmental Studies, Kyoto University, Japan
b Research Institute for Interdisciplinary Science, Okayama University, Japan
c Institute of Multidisciplinary Research for Advanced Materials (IMRAM), Tohoku University,Japan
d Department of Material Science, Graduate School of Science, University of Hyogo, Janan

-Poster Session-

The poster number with "S" is eligible for the Best Student Poster Award nomination.

P41 Band structure of chiral magnet $Yb(Ni,M)_3Al_9$ (M=Pd,Pt) observed by ARPES

Y. Murakami[a], Y. Tanimoto[b], Y. Nakashima[b], K. Kimura[b], H. Sato[c], K. Tanaka[d], K. Yamagami[e], S. Nakamura[f], S. Ohara[f]

a Faculty of Science, Hiroshima University, Japan
b Graduate School of Advanced Science and Engineering, Hiroshima University, Japan
c Hiroshima Research Institute for Synchrotron Radiation Science, Hiroshima University, Japan
d UVSOR synchrotron Facility, Institute for Molecular Science
e Japan Synchrotron Radiation Research Institute
f Japan Graduate School of Engineering, Nagoya Institute of Technology

Design Study of Combined-function Magnets for HiSOR-II Storage Ring

Takaya Narai[a], Christian John[a],
Miho Shimada[b,a], Hiroshi Miyauchi[b,a], Masahiro Katoh[a]

[a]*Hiroshima University*
2-313 Kagamiyama, Higashi-Hiroshima, Hiroshima 739-0046, Japan
[b]*High Energy Accelerator Research Organization (KEK)*
1-1 Oho, Tsukuba, Ibaraki 305-0801, Japan

Keywords: storage ring, magnet.

At Research Institute of Synchrotron Radiation Science, Hiroshima University, we are planning to build an electron storage ring, HiSOR-II, as a successor to the present light source accelerator HiSOR, which is losing reliability and competitiveness due to aging. To achieve high performance while remaining appropriate in size as a university facility, the new storage ring should be as compact as possible. To realize this, we are considering introducing a combined-function magnet that generates multiple magnetic field components with a single magnet. In this article, we report on some results from the preliminary design study of a quadrupole/sextupole combined-function magnet.

There are two schemes to realize a combined-function magnet of this kind. One is to optimize the shape of the magnetic poles. Generally, poles of a single-function magnet is shaped so as to be the equipotential surface of a required magnetic field component. In case of combined-function magnet, it would be a sum of equipotential surfaces of several field components [1]. In this method, a magnetomotive force produce several field components all at once. Therefore, it is advantageous for energy saving. On the other hand, the ratio of the field strengths of those components are fixed and cannot be changed independently. This would give some limitations on the accelerator operation.

Another is to put additional coils on the magnetic poles of a normal quadrupole magnet [2]. In this case, one pair of coils is put on each magnetic pole. One coil is put on the pole face and another near the base of the pole. These two coils produce magnetic fields which consists of dipole field and sextupole field with different ratio in strengths. By adjusting the excitation currents of the coils, the dipole field can be cancelled and consequently only the sextupole field remains. In this scheme, the sextupole field strength can be changed independently from the quadrupole field strength. On the other hand, additional electromotive forces are necessary which is a disadvantage for energy saving. In addition, the coils on the pole face should be water cooled because which have relatively large electric current density because the coils on the pole shape cannot have so large diameter because of the limited space between the pole and the beam pipe. This may increase the construction cost and also would cause water leakage troubles in future.

We are going to merge these two schemes described above to eliminate the disadvantages. The magnet will produce two field components mainly by the pole shape scheme, but it also has additional coils to realize the independent change of the strengths of the two components for certain extent. The details of the magnet design and of the magnetic field simulation are described elsewhere [3]. Here, we just describe their outlines. The target magnetic field is 15 T/m for quadrupole and 100 T/m^2 for sextupole. The bore radius of the magnet was determined so as to fit a beam pipe of an elliptical cross section with the inner diameters of 60 mm in horizontal and 30 mm in vertical and with a 3mm wall thickness. The pole shape was determined to fit to the equipotential surface of the required magnetic field which consists of two components. In this study, the shape of the return yoke and the width of the pole were not well optimized, which were not significant on the field strength. A pair of additional coils are put on each pole as described above.

The magnetic field was calculated by POISSON [4], which is a 2-D simulation code based on the finite element method. First, the simulation was carried out for without the additional coils. The result is shown in

Figure 1 (left). The field lines mostly seem like those of quadrupole field but small asymmetry can be seen, which corresponds to the sextupole components. Then, the simulation was carried out for producing sextupole field only by using additional coils. The current of the coils were determined so that the dipole field at the magnet center was cancelled. The result is shown in Figure.1 (right). It can be seen that, at around the center, pure sextupole field was produced. Finally, the simulation was carried out for exciting both main coil and additional coils. As fixing the current of the main coil and changing those of additional coils, it was confirmed that the field strength of quadrupole is kept constant against the change of the current of the additional coils. The strength of the sextupole field varied by about 3% for the current of the additional coils on the pole face of 20 AT. If the additional coil has 4 turns and 20 A, the adjustability of the sextupole field larger than 10% would be realized.

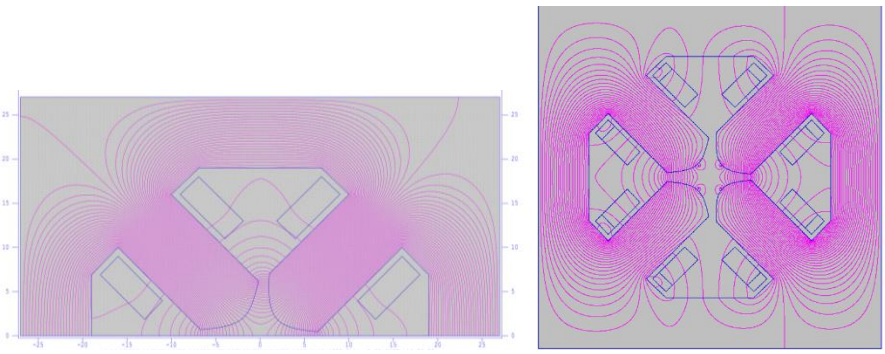

FIGURE 1. Field lines of combined-function magnet. Left; Quadrupole/sextupole combined field produced by pole shaping. Only the upper half of the cross section is shown. Right; Sextupole field produced by additional coils on the pole. The size of the magnet is same as the left figure but full cross section is shown. [3]

REFERENCES

1. "MAX-IV Detailed Design Report on the MAX-IV Facility", https://www.maxiv.lu.se/wp-content/plugins/sharepoint-plugin/ajax/downloadFile.php?site_id=MAXIV&version_series_id=38&repository_id=0fbdb5b5-c377-4ff8-9350-6889fdf4c076
2. J. Yamazaki *et al*., Proc. 13th Symposium on Accelerator Science and Technology, 280-282 (2001).
3. T. Narai, Bachelor Thesis, Hiroshima U. (2026).
4. "POISSON/SUPERFISH Manual", LA-UR-87-126 (1987).

Design Study of Beam Injection and Extraction at HiSOR-II Booster Synchrotron

Daisuke Fujita[a], Miho Shimada[b,a], Hiroshi Miyauchi[b,a], Masahiro Katoh[a]

[a]*Hiroshima University*
2-313 Kagamiyama, Higashi-Hiroshima, Hiroshima 739-0046, Japan
[b]*High Energy Accelerator Research Organization (KEK)*
1-1 Oho, Tsukuba, Ibaraki 305-0801, Japan

Keywords: synchrotron, electron beam, beam transport, injection, extraction.

Nearly 30 years have passed since the construction of the small synchrotron radiation source, HiSOR, at Hiroshima University. In these years, its aging has led to a serious decline in its availability and performance competitiveness. Therefore, the HiSOR-2 project is being proposed, which involves the construction of a new storage ring with a circumference of 44 m and a beam energy of 600 MeV, as well as an injector that will enable top-up operation. One of the options of the plan is to utilize the present HiSOR injector, 150 MeV microtron, as a pre-injector and to construct a new booster synchrotron of 600 MeV. Its circumference will be 22 m, which is exactly a half of the storage ring. The preliminary layout of the accelerator complex of HiSOR-2 is shown in Figure 1 as well as that of the present HiSOR.

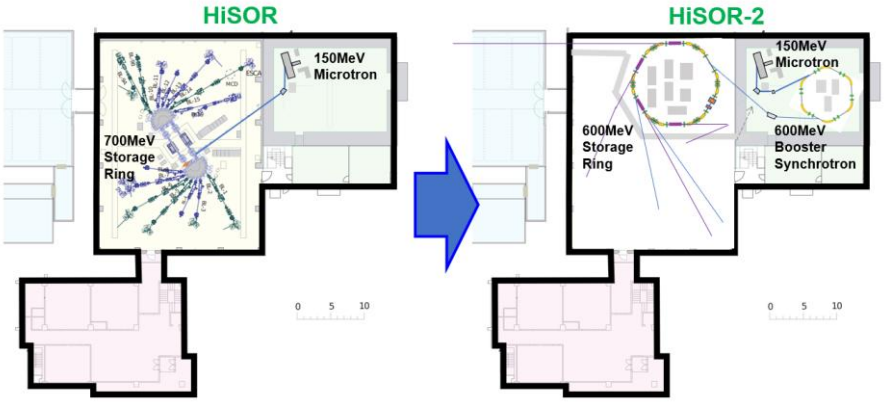

FIGURE 1. Layout of present HiSOR (left) and that of new HiSOR-2 (preliminary) (right).

In this study, we developed a simulation code on electron orbit in a synchrotron using transport matrices to design the beam injection and extraction schemes on the booster synchrotron [1]. In many cases, for the beam injection into a synchrotron, to reduce the oscillation amplitude after the injection, kicker magnets are used to shift the reference orbit of the synchrotron closer to that of the beam transport line. Usually, three or four kicker magnets are used to make a local bump orbit that the reference orbit in a small section of synchrotron is shifted and other sections are not [2]. On the other hand, a simple injection scheme using only one kicker has been applied to a small synchrotron or to early commissioning stage of a large synchrotron [3]. We examined this scheme because this scheme enables us to save the space and the construction cost.

Based on the simulation study, we demonstrated that injection was possible by placing one kicker magnet at the exact opposite side of the beam injection point. By adjusting the kicker strength properly, the injected beam circulates the synchrotron without hitting the wall of the injection septum magnet which is the most limiting the transverse acceptance. An example of the orbit of the injection beam is shown in Fig. 2. Furthermore, we confirmed that the electron beam with the pulse length as long as 0.6 microsecond can be injected, which is thought to be practical.

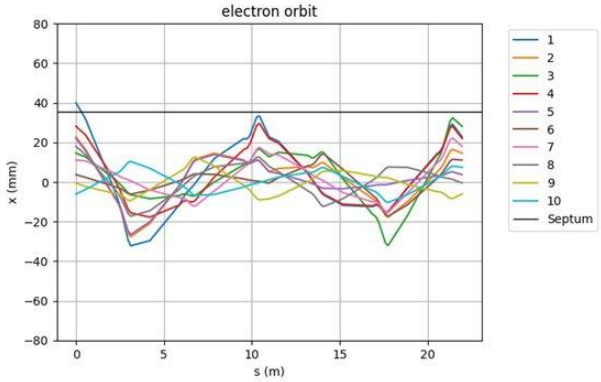

FIGURE 2. An example of the orbit of the injected beam. The horizontal axis is the distance from the injection point. The electron orbit in each turn up to 10 is shown with different colors. The origin is the injection point. The black line indicates the position of the septum wall.

We also made simulation on the beam extraction from the synchrotron. We confirmed that it is possible to extract the circulating beam with one kicker. Because the circumference of the synchrotron is so small, the rise time of the kicker magnet should be faster than about 40 nano-second, otherwise more than half of the beam cannot be extracted.

In summary, we have demonstrated that the injection into the HiSOR-2 booster synchrotron can be made by only one kicker magnet as well as the extraction by another one. The next challenge is to confirm the efficiency of the beam transport as taking into the account the effects of the spatial and energy spread of the electron beam.

REFERENCES

1. D. Fujita, Bachelor Thesis, Hiroshima U. (2026).
2. M. Watanabe *et. al*., “Design on Injector Synchrotron”, UVSOR-7 (1981) (in Japanese)
3. S. C. Leemann, Nucl. Instr. Meth. Phys. Res. A693 (2012) 117–129.

Experimental Study on Single Electron Storage at UVSOR-Ⅲ in 2025

Y. Asai[a,d], M. Shimada[b,c], H. Miyauchi[b,c], T. Kaneyasu[d] and M. Katoh[a,c,d]

[a]*Graduate School of Advanced Science and Engineering Hiroshima University, 1-3-1 Kagamiyama Higashi-Hiroshima 739-8526, Japan*
[b]*High Energy Accelerator Research Organization (KEK), 1-1 Oho Tsukuba 305-0801, Japan*
[c]*Research Institute for Synchrotron Radiation Science, Hiroshima University, 2-313 Kagamiyama Higashi-Hiroshima 739-0046*
[d]*UVSOR Synchrotron Facility, 38 Nishigo-Naka Myodaiji Okazaki 444-8585, Japan*

Keywords: electron, photon, insertion device, undulator, synchrotron radiation, quantum mechanics, machine learning

We have been conducting single-electron storage experiments at UVSOR-III since 2021 with the aim of performing fundamental studies of electromagnetic radiation [1]. At UVSOR-III, single-electron experiments were carried out at beamline BL1U [2, 3] using two identical permanent-magnet APPLE-II undulators, each consisting of 10 periods, and a three-magnet chicane installed between them. These undulators can generate arbitrary elliptical polarization. In this case, for the single-electron measurements they were set to linear horizontal polarization with a central wavelength of 355 nm. The experiments were performed using either a single undulator or both undulators tuned to the same wavelength in an optical-klystron configuration. Undulator radiation in the UV region was extracted into the atmosphere and its intensity was measured using a photomultiplier tube. By applying suitable band-pass filters to suppress background light and a beam scraper to reduce the electron beam intensity, we successfully observed step-function-like intensity changes under few-electron storage conditions with a good signal-to-noise ratio, confirming single-electron storage. Then, we further improved the operational efficiency and automation of the single-electron storage technique and initiated experiments to observe synchrotron radiation from a single electron. As a result, we confirmed that the undulator radiation emitted by a single electron follows a Poisson distribution, where the number of emitted photons per pass is much smaller than unity, in agreement with theoretical predictions based on classical electrodynamics [4].

From this result, it is expected that a single electron passing through the undulator may occasionally emit two photons simultaneously. In recent quantum measurement and sensing technologies, quantum-entangled photon pairs are widely utilized; therefore, the observation of simultaneous two-photon emission events could provide a pathway toward generating entangled photon pairs using synchrotron radiation. To investigate such simultaneous two-photon emission events, experiments were performed using the setup shown in Fig. 1(a), where the coincidence of two photons was examined. In addition, to study the wave–particle duality of photons, a double-slit experiment was carried out using the setup in Fig. 1(b). The latest experimental results will be presented at the symposium.

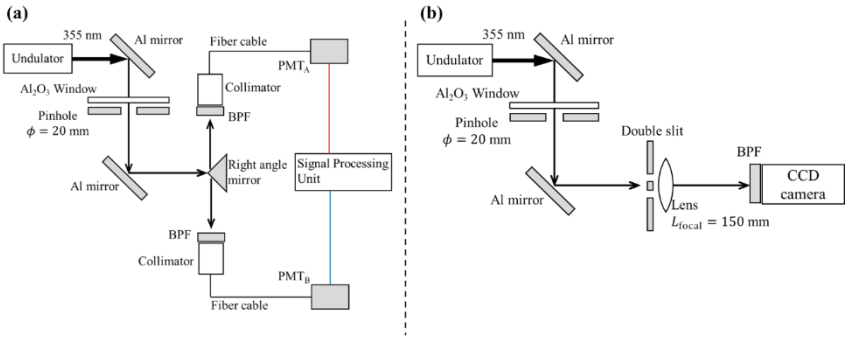

FIGURE 1. The experimental setup.

REFERENCES

1. Y. Asai, M. Shimada, H. Miyauchi, and M. Katoh, “Experimental Study on Single Electron Storage in 2024” presented at *The 29th Hiroshima International Symposium on Synchrotron Radiation* (2025)
2. M. Katoh, H. Ota, J. Yamazaki, K. Hayashi, Y. Okano, E. Salehi, Y. Taira, A. Mano, M. Fujimoto, Y. Takashima, M. Hosaka, F. Sakamoto, T. Kaneyasu, and H. Zen, *Journal of Physics*: Conference Series **2687**, 032005 (2024)
3. T. Kaneyasu, Y. Hikosaka, S. Wada, H. Ota, H. Iwayama, K. Shimizu, M. Fujimoto, and M. Katoh, *Synchrotron. Journal of Physics*: Conference Series **3010**, 012086 (2025)
4. K. J. Kim, “CHARACTERISTICS OF SYNCHROTRON RADIATION” in *Physics of Particle Accelerators: Fermilab Summer School, 1987; Cornell Summer School, 1988*, edited by M. Month and M. Dienes., AIP Conference Proceedings 184, American Institute of Physics, New York, 1989, pp. 565-632.

Design Proposal of a VUV Undulator Beamline for HiSOR-II

Masashi Arita, Kenya Shimada, Taichi Okuda, Hirofumi Namatame, and Masahiro Katoh

[a]*HiSOR, Hiroshima University, 2-313 Kagami-yama, Higashi-Hiroshima, Hiroshima 739-0046, Japan*

Keywords: Beamline, HiSOR-II

A new 600 MeV synchrotron radiation ring, HiSOR-II, is currently being planned at Hiroshima University as an upgrade of the existing HiSOR facility. We are developing a high-resolution undulator beamline dedicated to ARPES and Spin-ARPES experiments. A 56 mm period APPLE-II undulator will be installed in a two-meter-long straight section as the photon source. The expected photon energy range is 7.4–250 eV for horizontally and vertically linear polarization and 5–55 eV for circular polarization [1], which is comparable to that of the present HiSOR BL-1 beamline.

Although the emittance of HiSOR-II is 17.6 nm·rad, the relatively low beam energy results in a comparatively large electron beam size, and consequently a large photon source size. At a photon energy of 50 eV, simulations predict FWHM source sizes of 645 µm horizontally and 147 µm vertically. The angular divergences (RMS) are estimated to be 100 µrad horizontally and 88 µrad vertically [1,2]. In order to achieve high energy resolution over a wide photon energy range under these source conditions, several monochromator concepts were investigated by means of ray-tracing simulations [2]. Among them, a divergent-beam incidence variable-line-space (VLS) plane grating monochromator (d-VLSPGM) was selected because of its large design flexibility in the magnification factor *Cff* and its potential for high resolving power over a wide energy range. Considering the relatively large source size and the expected long-term beam fluctuations during top-up operation in a compact storage ring, a front-end focusing system with an entrance slit was adopted. The total beamline length from the source point to the experimental focus point is approximately 40 m, which corresponds to the maximum available length in the planned HiSOR-II ring hall. The pre-focusing optics and the refocusing optics are each designed to occupy approximately 8 m, while the distance between the entrance and exit slits is kept within 24 m.

The beamline layout is shown in Figure 1, and the optical parameters are summarized in Table 1. The pre-focusing system consists of a horizontally deflecting toroidal mirror (M0). With a vertical demagnification factor of 0.4, the vertical beam size at the entrance slit is reduced to 75 µm in FWHM at 50 eV. In the horizontal direction, the beam is collimated before entering the monochromator section. A plane mirror (M1) is used to vary the included angle in the range of 153° to 168° and to direct the beam onto the VLS plane grating (Gr). Three gratings are assumed to cover the photon energy range from 10 to 260 eV. The VLS parameters were optimized to achieve target energy resolutions of less than 1 meV at 20 eV and 50 eV, and approximately 5 meV at 150 eV, as summarized in Table 2. After diffraction, the horizontally collimated beam is focused onto the exit slit position by a cylindrical mirror (M2) placed upstream of the exit slit.

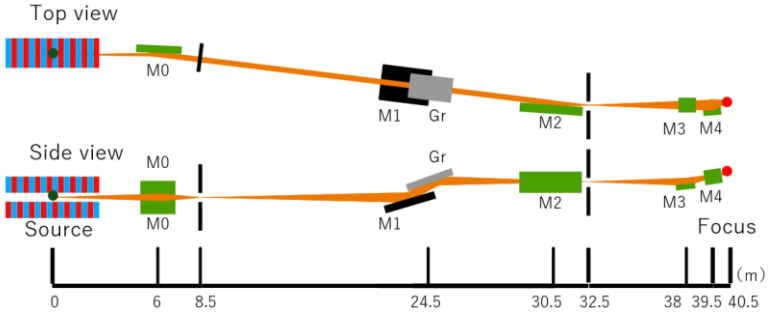

FIGURE 1. d-VLSPGM beamline layout.

TABLE 1. Parameters of the optical elements

Opt. element	Figure	Direction	Angle(deg.)	Slope error (μrad)
M0	Toroidal	Horizontal	88	0.5/2
M1	Plane	Vertical	153-168(Include)	0.5/2
Gr	VLS-Plane G	Vertical	Variable	0.2/2
M2	Cylindrical	Horizontal	88	0.5/2
M3	Elliptical cylinder	Vertical	88	0.2/2
M4	Elliptical cylinder	Horizontal	88	0.2/2

TABLE 2. Parameters of the Gratings

Gratings	VLS parameters n10(Groove density L/mm), n20, n30	Energy Range (eV)	*Cff*
GL	300, 0.0984837, 1.04468×10^{-5}	10-36	2.3 @ 10eV
GM	1200, 0.344057, 3.83313×10^{-5}	27-120	3 @ 27eV
GL	2000, 0.636682, 6.80726×10^{-5}	55-256	2.4 @ 100eV

To evaluate the energy resolution at a photon energy of 50 eV, three closely spaced photon energies of 49.999 eV, 50.000 eV, and 50.001 eV were introduced through a fully opened entrance slit. Figure 2a shows the simulated intensity distributions at the exit slit. The results demonstrate that the three photon energies are clearly resolved. When the exit slit width is set to 20 μm, the estimated energy resolution is 1.07 meV (FWHM) at 50 eV.

Recent ARPES experiments increasingly require a smaller beam spot size at the sample position. Therefore, the beam from the exit slit is focused using a Kirkpatrick–Baez configuration consisting of two elliptical cylindrical mirrors. The vertical and horizontal demagnification factors are designed to be 0.55 and 0.13, respectively. Figure 2b shows the simulated beam spot at the sample position, showing that a spot size of 31.4 μm horizontally and 8.5 μm vertically in FWHM can be achieved. These results demonstrate that the proposed beamline design can provide both high energy resolution and a sufficiently small spot size for advanced ARPES and Spin-ARPES experiments. Further reduction of the horizontal spot size is expected through additional optimization of the K-B mirror configuration.

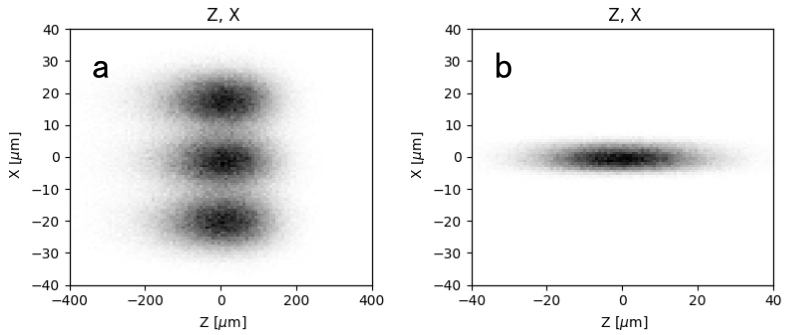

FIGURE 2. (a) Simulated energy dispersion for photon energies of 49.999, 50.000, and 50.001 eV at the exit slit. **(b)** Simulated beam spot at the sample position with FWHM sizes of 31.4 μm (horizontal) and 8.5 μm (vertical).

REFERENCES

1. L. Rebuffi and M. S. del Rio, Proc. SPIE 10388,169 (2017).
2. T. Tanaka and H. Kitamura, J. Synchrotron Radiat. 8, 1221 (2001).

Simulation and Experimental Studies on Radiation Generation in an Electron Storage Ring

Runa Murayama[a], Miho Shimada[b,a], Hirohi Miyauchi[b,a], Katoh Masahiro[a]

[a]*Hiroshima University (HiSOR)*
2-313 Kagamiyama, Higashi-Hiroshima, Hiroshima 739-0046, Japan
[b]*High Energy Accelerator Research Organization (KEK)*
1-1 Oho, Tsukuba, Ibaraki 305-0801, Japan

Keywords: storage ring, radiation protection, electron, positron, gamma-ray, neutron

The synchrotron radiation source at Hiroshima University, HiSOR which was constructed nearly 30 years ago, has been facing serious challenges, including a decline in competitiveness due to construction and commissioning of new generation light sources with higher-performance as well as a reduction in operational availability caused by aging of the facility. In response to these issues, the construction of a successor facility, HiSOR-2, is being planned.

In many electron storage rings used as synchrotron light sources have shielding walls surrounding them. However, the current machine, HiSOR, does not have such shielding wall. It has two huge bending magnets of 180 degrees. Their iron cores are H-shaped and the return yokes of outer sides play the role of shielding wall. However, its successor, HiSOR-2, will not employ such specially designed bending magnets but instead will use bending magnets of normal shape and standard size. As a result, the shielding effect provided by the yoke of the bending magnets will not be expected. Therefore, it is being considered to surround the accelerator with shielding walls. To save the construction cost, a rational scheme of radiation protection is required.

As the first step of our study on the radiation protection for HiSOR-2, we are investigating the shielding effects of accelerator components, particularly those of the magnets. We constructed a simple model of a part of a storage ring consisting of a straight section followed by a bending section, as shown in Figure 1. In this model, we consider collisions between stored high energy electrons and residual gas molecules in the vacuum chamber. The collision would result in changes in the momentum and energy of an electron and would significantly change its orbit. When this change is larger than some threshold, the electron finally hits the vacuum chamber wall and generate electromagnetic showers which contain gamma-rays, electrons and positrons. In addition, gamma rays are also produced via bremsstrahlung when the electron collides with the gas molecules. The gamma-rays produce neutrons when they hit some materials. The behavior of their propagation in air provides fundamental knowledge necessary for considerations of radiation protection.

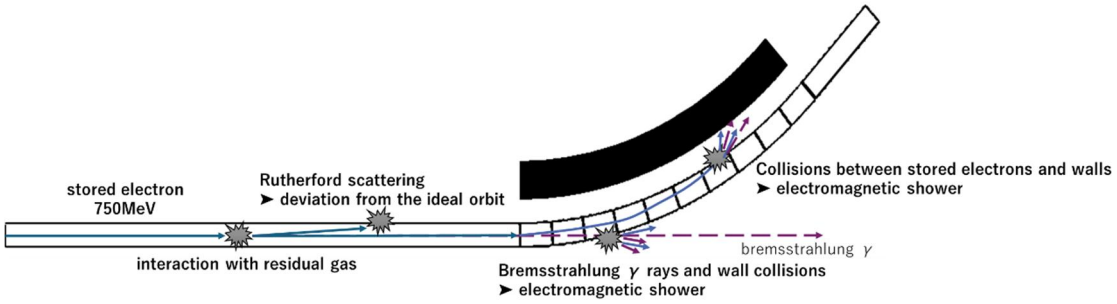

FIGURE 1. Beam loss mechanisms due to residual gas interactions

The simulations were performed using PHITS (Version 3.350) [1]. The simulation model consists of a C-shaped bending magnet with a yoke of iron and coils of copper and vacuum chamber (beam pipe) of SUS.

The model is based on the UVSOR electron storage ring, which is a typical low energy synchrotron light source [2]. In the model, the vacuum chamber is filled with monoxide (CO) gas of an appropriate pressure. Electrons running on the reference orbit come into the system. Some of them collide with residual gas at the straight section and deviate from their original orbit. The effect of the magnetic field is included in the simulation. Therefore, the electrons that lose energy are largely deflected in the bending magnet section. An example of the simulation result is shown in Figure 2, where the flux of the radiation is indicated by color. Generation and propagation of the radiation are clearly seen in the result.

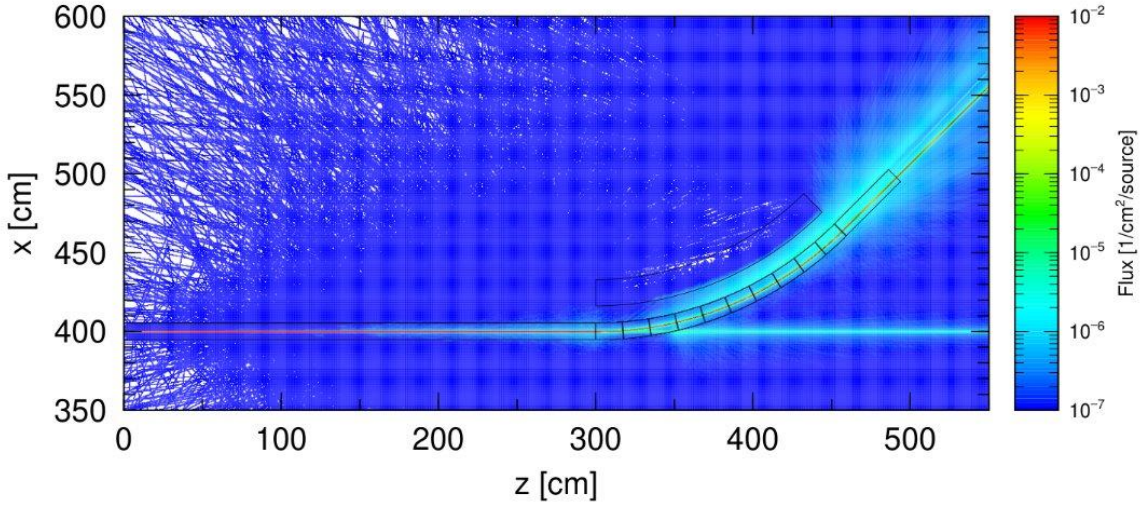

FIGURE 2. An example of simulation result. The flux of the radiation composed of mainly electrons and gamma-ray are indicated by color.

In parallel to the simulation study, a measurement study at the UVSOR storage ring is going on using Gafchromic films. Comparisons between the measurements and the simulation results are being conducted. The results will be reported in near future.

.

REFERENCES

1. T. Sato *et al*., ***J. Nucl. Sci. Technol***. 61, 127-135 (2024)
2. H. Ota *et al*., ***J. Phys.: Conf. Ser***. 2380(1) 012003-012003 (2022)

BeamCast – A New Operation Status Display System for the HiSOR Storage Ring

Christian John

[a]*Hiroshima University / Research Institute for Synchrotron Radiation Science (HiSOR), Kagamiyama 1-3-1, Higashihiroshima, Japan*

Keywords: Accelerator, Synchrotron, Storage Ring, Operation Status, Beam Current, Beam Lifetime

On the 30th anniversary of the Hiroshima Synchrotron facility (HiSOR) a new operation status display system shall be developed. A preliminary version of this system – called BeamCast beta – has been commissioned in early February 2026. Herewith I report on the project's progress, discuss the system's functionalities contrasted by its physical limitations, and explore some options for HiSOR's future endeavors.

First, we examine the web interface and its dedicated features which are shown in **Fig. 1**. The basic requirements that have been put on this system include automatic measurement functionality, live display of the stored current and correlated beam lifetime, as well as an operator comment window.

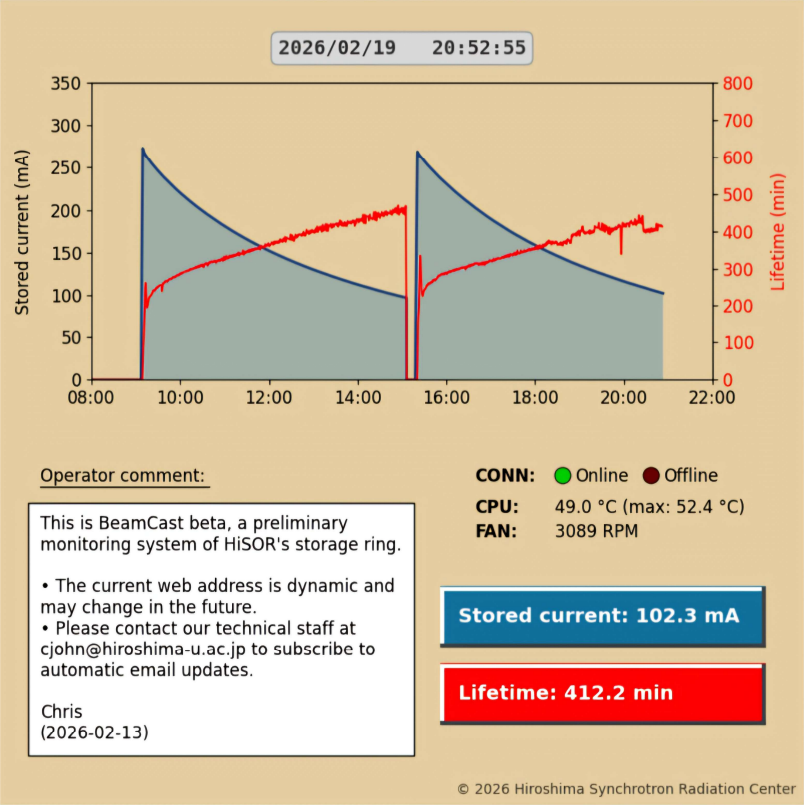

FIGURE 1. Web interface showing the preliminary layout of the status display during a live measurement.

The core monitoring capability is twofold: a diagram filling the upper half with a fixed time frame ranging from 8 A.M. to 10 P.M, and framed 24-hours digital displays in the lower right corner – both indicating the stored current in units of mA (blue) and the lifetime in minutes (red). Furthermore, the parameters of the processing unit – essentially a single-board computer (SBC) – are also monitored: the SCPI-handshake between the SBC and the digital multimeter (CONN) is indicated visually by two status lights, the CPU

temperature and max temperature in degrees Celsius, as well as the fan speed in RPM. In addition to that, the operator of the accelerator may leave a short note for the beamline users: up to 10×42 characters plus a bracketed date are hosted by a dedicated comment box in the lower left corner. This technical esemble of live status panels is complemented by a framed date and time window on top of the diagram.

Next, we review this modest status display system on a flow chart (**Fig. 2**). A converter provides an output signal that is proportional to the stored current. A SIGLENT SDM3055 multimeter measures the low-voltage signal and sends data upon SCPI-request to a Raspberry Pi 5 equipped with a 64-bit ARM Cortex-A76 CPU. The SBC logs the measured values for a finite time in a CSV-file, processes them, and generates a PNG-image. Upon browser request, the flask-based server sends the image to the client (pull-principle). This process repeats every 15 seconds via an automatically triggered HTTP request. To ensure secure data transfer, an encrypted communication channel (TLS) is established between server and an HTTPS gateway.

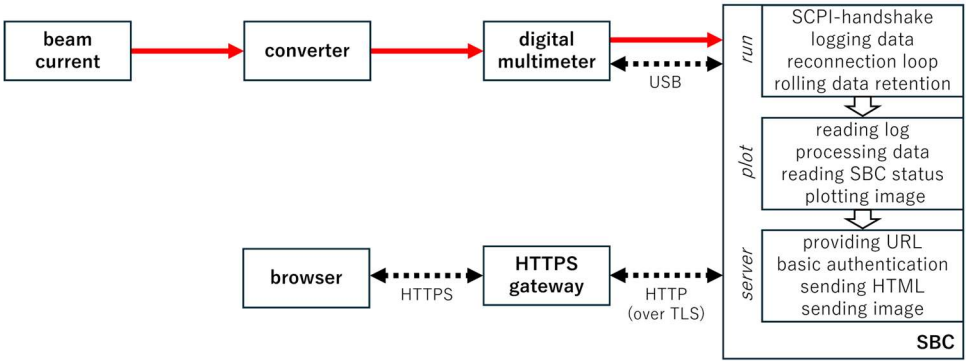

FIGURE 2. Flow chart showing the physical signal (red arrow), communication layer (dotted arrow), and data processing (short arrow).

Now, we analyze some of the data processing structures that underpin the entire data output (**Table 1**). To satisfy automation, the Raspberry Pi OS starts service routines on startup to call scripts that carry out various tasks divided into three groups: run, plot, and server.

TABLE 1. Some data processing functions. The service files can be found in the directory /etc/systemd/system/.

Function	Data processing algorithm	Service-file
Calibration of stored current	current_ma = voltage * 50	beamcast-run.service
Clipping of negative stored current	i.append(max(0.0, val))	beamcast-plot.service
Calculation of beam lifetime over three sampling steps	I1 = i_array[idx] I2 = i_array[idx+3] tau = -dt / (np.log(I2 / I1))	
Averaging of beam lifetime over five samples (window = 5)	kernel = np.ones(window) / window lifetime = np.convolve(lifetime, kernel, …)	
Centering of beam lifetime value	t_lifetime = [t[k] + (t[k+3] - t[k]) / 2]	

A fixed calibration factor relates signal voltage to stored current, while negative values are clipped to zero as they are not meaningful and may arise from signal noise or microampere-order offsets. Logging intervals are 15 seconds long and the CSV-file is truncated after three days. A logarithmic function is used to reflect the exponential decay of the stored electron beam, where the input values of I_1 and I_2 are separated by three sampling steps to reduce fluctuations in the signal. Then, a moving average filter over five sampling steps is applied and the lifetime value is centered to its corresponding time frame.
Furthermore, health and connectivity of the SBC as well as a dedicated JSON-file containing the operator comment are read out. Ultimately, all the generated data is plotted into a PNG-file (see Fig. 1) which is overwritten every 15 seconds.

Finally, we discuss the limitations and outlook of the presented system. BeamCast beta is based on a dynamic web URL which may change upon gateway reconnection. To compensate for that, an email service has been set up to inform subscribers automatically. When finalized, the system will be transferred to a static domain. Integrating a dedicated user counter or a vacuum readout function is a conceivable option for future extensions.

Doping-Induced Evolution of the Electronic Band Structure in Ni-Doped PdSeTe

Yogendra Kumar[1], Takahiro Onimaru[2], Yasuyuki Shimura [2], Shinichiro Ideta[1], Kenya Shimada[1]

[1]*Research Institute for Synchrotron Radiation Science (HiSOR), Hiroshima University, Higashi-Hiroshima 739-0046, Japan*
[2]*Graduate School of Advanced Science and Engineering, Hiroshima University, Higashi-Hiroshima 739-8526, Japan*

Keywords: Electronic structure, First-principles calculations, Spin-orbit, coupling, Dirac/Weyl semimetal, Superconductivity, Surface states, Topological materials, Topological superconductor.

The interplay between superconductivity and topology in 111-type transition-metal dichalcogenides (TMDCs) provides a promising platform for realizing topological superconductivity [4-6]. PdSeTe exhibits enhanced superconductivity (Tc ≈ 3.2 K) [1] while preserving topological surface states. In contrast, partial substitution of Pd with Ni completely suppresses superconductivity, despite nearly identical crystal symmetry and overall band dispersion. This striking contrast offers a unique opportunity to isolate the microscopic ingredients governing superconductivity.

In this study, we investigate the doping-induced evolution of the electronic structure in Ni-doped PdSeTe using high-resolution synchrotron ARPES and first-principles calculations that include spin-orbit coupling. Our measurements reveal that, although the global band topology and Dirac-like surface states remain robust under Ni substitution, subtle yet critical modifications occur in the orbital character and Fermi-surface topology. Density functional theory (DFT) calculations indicate that replacing Pd 4d orbitals with more localized Ni 3d orbitals modifies hybridization strength and effective spin-orbit coupling, thereby redistributing spectral weight near the Fermi level.

These results demonstrate that superconductivity in PdSeTe is highly sensitive to transition-metal orbital character rather than lattice symmetry alone. Our findings establish Ni substitution as a powerful tuning parameter for disentangling orbital, spin-orbit, and lattice contributions, and provide key insights into the microscopic conditions required for superconductivity in topological TMDCs.

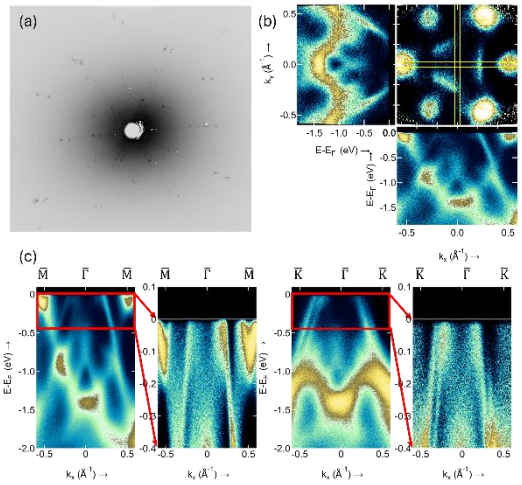

FIGURE 1. (a-c) Laue and *ARPES measurements on Ni-doped PdSeTe confirm the lattice symmetry and topological surface states similar to PdSeTe.*

REFERENCES

[1]. **Y. Kumar et al.**, *Enhanced Superconductivity with Preserved Topological States in PdSeTe*, **Phys. Rev. Research 7**, 013174 (2025).
[2]. **H.-J. Noh et al.**, *Experimental Realization of Type-II Dirac Fermions in $PdTe_2$*, **Phys. Rev. Lett. 119**, 016401 (2017).
[3]. **P. K. Das et al.**, *Bulk superconductivity in type-II Dirac semimetal $PdTe_2$*, **Phys. Rev. B 97**, 014523 (2018).
[4]. **M. Z. Hasan and C. L. Kane**, *Colloquium: Topological insulators*, **Rev. Mod. Phys. 82**, 3045 (2010).
[5]. **N. P. Armitage, E. J. Mele, and A. Vishwanath**, *Weyl and Dirac semimetals in three-dimensional solids*, **Rev. Mod. Phys. 90**, 015001 (2018).
[6]. **M. Sato and Y. Ando**, *Topological superconductors: a review*, **Rep. Prog. Phys. 80**, 076501 (2017).

ARPES Study of Pb Substitution at Bi Sites in Double-Layer Cuprate Bi2212

A. Higuchi[a], Y. Tsubota[b], Y. Miyai[b], S. Nakagawa[c], S. Ishida[d], K. Tanaka[e], H. Eisaki[d], T. Kashiwagi[c], M. Arita[f], S. Kumar[g], K. Shimada[a,b,f,h,i], S.Ideta[a,b,f]

[a]*Faculty of Science, Hiroshima University, Higashi-Hiroshima 739-0046, Japan*

[b]*Graduate School of Advanced Science and Engineering, Hiroshima University, Higashi-Hiroshima 739-0046, Japan*

[c]*Tsukuba University, Tsukuba 305-8577, Japan*

[d]*National Institute of Advanced Industrial Science and Technology (AIST), Tsukuba 305-8560, Japan*

[e]*UVSOR-Ⅲ Synchrotron, Institute for Molecular Science, Okazaki 444-8585, Japan*

[f]*Hiroshima Syncrotron Radiation Center (HiSOR), Hiroshima University, Higashi-Hiroshima 739-0046, Japan*

[g]*Institute of Microelectronics (IME), Agency for Science, Technology and Research (A*STAR), Singapore 138632*

[h]*International Institute for Sustainability with Knotted Chiral Meta Matter (WPI-SKCM^2), Higashi-Hiroshima 739-8526, Japan*

[i]*Research Institute for Semiconductor Engineering, (RISE), Hiroshima Univ., Higashi-Hiroshima 739-8527, Japan*

Keywords: ARPES, high- T_c cuprate superconductors, Bi2212

High-T_c cuprate superconductors show the highest superconducting transition temperatures (T_c) under ambient pressure. However, the mechanism of superconductivity remains unclear. These materials are characterized by CuO_2 planes in which superconductivity emerges when charge carriers are doped into the plane with an antiferromagnetic phase. The superconducting properties are typically explained using an electronic phase diagram, which illustrates the relationship between T_c and carrier concentration. It is well known that there is a typical phase diagram, which is referred to as a “universal phase diagram”[1,2]. The optimal hole concentration is around 0.16. This empirical phase diagram has been used to estimate carrier concentration from T_c. However, recent studies have reported that there is a deviation from the universal phase diagram, suggesting that the phase diagram may depend on composition and preparation conditions of the sample [3,4, 5, 6].

A bilayer hole-doped cuprate, $Bi_2Sr_2CaCu_2O_{8+\delta}$ (Bi2212), allows a systematic control of carrier concentration through oxygen content and chemical substitution. However, the Pb substitution at the Bi site modifies the charge balance and suppresses the structural modulation, and therefore, the hole concentration shifts toward the overdoped regime. Additionally, subsequent reduction annealing is necessary to optimize the T_c of Pb-substituted Bi2212, which makes it difficult to determine carrier concentration solely from T_c. Angle-resolved photoemission spectroscopy (ARPES) provides a direct probe of the electronic structure in a solid. The Fermi surface area measured by ARPES can be used to estimate carrier concentration based on the Luttinger sum rule, offering a more quantitative approach than empirical relations.

In this study, we have performed ARPES measurements on Pb-substituted and slightly overdoped Bi2212 with T_c of ~90 K. Our experimental results indicate that samples with similar T_c can exhibit noticeably

different carrier concentrations. In the poster presentation, we will show our ARPES data and discuss reasons for the discrepancy between the universal phase diagram and our revised version.

REFERENCES

1. M. R. Presland *et al*., Physica C **176,** 95–105, (1991).
2. S. D. Obertelli, J. R. Cooper, and J. L. Tallon., Phys. Rev. B **46**, 14928 (1992).
3. T. Honma *et al*., Phys. Rev. B **70**, 214517 (2004).
4. T. Honma *et al*., Phys. Rev. B **77**, 184520 (2008).
5. H. Sakamoto *et al*., JPSJ **85**, 104710 (2016).
6. I.K. Drozdov *et al*., Nat. Commun. **9**, 5210 (2018).

Electronic States in Electron-Doped High-T_c cuprate $Nd_{2-x}Ce_xCuO_4$ investigated by Angle-Resolved and Inverse Photoemission Spectroscopies

H. Yamaguchi[a], Y. Tsubota[a], Y. Miyai[a], M. Arita[b], H. Sato[a,b], D. Song[f], K. Tanaka[e], K. Shimada[a,b,c,d], S. Ideta[a,b]

[a]*Graduate School of Advanced Science and Engineering, Hiroshima Univ., Higashi-Hiroshima 739-0046, Japan*
[b]*Research Institute for Synchrotron Radiation Science, Hiroshima Univ., Higashi-Hiroshima 739-0046, Japan*
[c]*Research Institute for Semiconductor Engineering, (RISE), Hiroshima Univ., Higashi-Hiroshima 739-8527, Japan*
[d]*International Institute for Sustainability with Knotted Chiral Meta Matter (WPI-SKCM^2), Higashi-Hiroshima 739-8526, Japan*
[e]*UVSOR-III Synchrotron, Institute for Molecular Science., Okazaki, Aichi 444-8585, Japan*
[f]*University of British Columbia,Vancouver, BCV 6T1Z4, Canada*

Keywords: cuprate superconductors, charge fluctuation, electronic structure, ARPES, IPES

The mechanism of superconductivity in conventional superconductors is understood to involve the formation of Cooper pairs via phonons, which is explained by BCS theory. In contrast with "low-temperature" superconductors, cuprate "high-temperature" superconductors were discovered in 1986, which show the highest superconducting transition temperatures (T_c), however, as for elucidations of their pairing mechanism, both experimental and theoretical studies have not been achieved yet. One of the most urgent issues in clarifying the mechanism of high-T_c cuprate superconductivity is to understand the origin, namely, boson that mediates Cooper pairing. While electron-boson interactions and strong electron correlations are believed to contribute to the origin of high-T_c cuprate superconductivity [1–3], there is less research into the origin of the boson and the pairing mechanism in electron-doped cuprates than in hole-doped ones. Therefore, to deepen the understanding of the microscopic mechanism of superconductivity through observations of the electronic states in electron-doped cuprates, we have investigated the electronic structure of $Nd_{2-x}Ce_xCuO_4$ (NCCO), one of the electron-doped high-T_c cuprate superconductors, using angle-resolved photoemission spectroscopy (ARPES) and angle-resolved inverse photoemission spectroscopy (AR-IPES).

In this study, we experimentally performed ARPES and AR-IPES studies to investigate the presence of an emergent band structure arising from the coupling between quantum charge fluctuations and quasiparticles in high-T_c cuprate superconductors. Furthermore, by comparing our experimental results of the electronic structure and calculations obtained from density functional theory (DFT) and dynamical mean-field theory (DMFT) calculations [6].

In addition, to study an insight of the ground state of NCCO, we have studied temperature dependent ARPES study for the spectral weight (Z_k) of the quasiparticle band along the nodal direction in ARPES spectra. A previous theoretical study suggested that if resonating-valence-bond-like electron correlations are involved, Z_k changes markedly across T_c in the ground state in strongly correlated electron systems such as cuprate superconductors [5]. This prediction has been verified by the temperature dependence of Z_k reported for hole-doped cuprates [4], and it could offer a new way of understanding the ground state of electron-doped cuprate superconductors.

In the poster presentation, based on experimentally obtained spectra of the electronic structure of NCCO, we discuss the verification of quantum charge fluctuations, including theoretical calculations (DFT+DMFT) and the temperature dependence of the Z_k spectrum.

REFERENCES

1 A. Lanzara *et al*., Nature **412**, 510 (2001).
2 J. P. Carbotte *et al*., Nature **401**, 354 (1999).
3 H. F. Fong *et al*., Phys. Rev. Lett. **75**, 316 (1995).
4 S. Kudo *et al*., Phys. Rev. B **92**, 195135 (2015).
5 C.-P. Chou *et al*, J. Phys. Chem. Solids **69**, 2993–2995 (2008).
6 H. Yamaguchi *et al*., arXiv:2505.12639.

Electronic structure of Fe_xTiS_2 ($x = 0 \leq x \leq 0.33$) studied by ARPES and XAS

K. Kimura[a], Y. Nakashima[a], Y. Tanimoto[a], Y. Murakami[b], H. Sato[c], M. Arita[c], S. Ideta[c], K. Shimada[c], M. Sawada[c], T. Bizen[d], M. Miyata[d], M. Koyano[d]

[a]*Graduate School of Advanced Science and Engineering, Hiroshima University, Higashi-Hiroshima 739-8526, Japan*
[b]*Faculty of Science, Hiroshima University, Higashi-Hiroshima 739-8526, Japan*
[c]*Hiroshima Research Institute for Synchrotron Radiation Science, Hiroshima University, Higashi-Hiroshima 739-0046, Japan*
[d]*School of Materials Science, Japan Advanced Institute of Science and Technology, Nomi 923-1292, Japan*

Keywords: intercalation, superlattice, angle resolved photoemission spectroscopy

1*T*-TiS_2 is non-magnetic layered material with 1*T*-CdI_2-type crystal structure. The hexagonal layer of Ti ions is sandwiched between the two hexagonal layers of S ions and the Ti ion is octahedrally coordinated with six S ions. The S-Ti-S triple layers are covalently bonded and these TiS_2 triple layers are weakly coupled with van der Waals (vdW) force. In the vdW gap located between the TiS_2 layers, the other 3*d* transition-metal *M* can be intercalated as M_xTiS_2. Among them, Fe_xTiS_2 exhibits a wide variety of magnetic properties [1]. With increasing the Fe concentration from $x = 0$, the cluster spin grass (CG) state with the Ising spins is found for $x < 0.20$. After exhibiting the antiferromagnetic (AFM) state from $x = 0.20$ to 0.28, the CG state is again realized for $0.28 < x < 0.38$ and the AFM state for $0.38 < x < 0.50$. Above $x = 0.50$, the ferrimagnetic behavior is observed. On the other hand, the Fe ions intercalated in the vdW gap between the TiS_2 layers occupy the octahedral site surrounded by six S ions. X-ray studies reveal the Fe random distribution for $x < 0.20$, while the formation of $2\sqrt{3}a \times 2a \times 2c$ superlattices due to the Fe ordering for $x = 0.25$ and $\sqrt{3}a \times \sqrt{3}a \times 2c$ superlattice for $x = 0.33$. The rich magnetic states of Fe_xTiS_2 are expected to link to the change in electronic band structure due to the Fe intercalation. In this study, we carried out angle-resolved photoemission spectroscopy (ARPES) and soft X-ray absorption spectroscopy (XAS) at the Ti 2*p* edge to investigate the electronic structure of Fe_xTiS_2 ($0 \leq x \leq 0.33$) at beamlines BL-1, BL-7 and BL-9A, and BL-14 of HiSOR, respectively.

Figures 1(a) and 1(b) show the ARPES spectra along the Γ-*M* direction for TiS_2 and $Fe_{0.33}TiS_2$, respectively, measured at 20 K using *p*-polarized light with a photon energy of $h\nu = 66$ eV. In TiS_2, an upward-dispersing band derived from S 3*p* orbitals is observed around the Γ point, while an electron pocket originating from Ti 3*d* orbitals appears around the *M* point. The Ti 3*d* electron pocket exhibits significantly reduced intensity under *s*-polarized light, indicating that it predominantly consists of the Ti $3d_{z^2}$ orbital component. In $Fe_{0.33}TiS_2$, both the S 3*p* and Ti 3*d* bands shift toward higher binding energies, demonstrating electron doping into the TiS_2 layers induced by Fe intercalation. From the observed Fermi surface volume, the electron doping level is estimated to be approximately 0.54 electrons per intercalated Fe ion. In addition, a dispersive Fe 3*d*-derived band emerges in the 0.2 - 0.8 eV binding energy range. This band exhibits band folding approximately at 0.6 k_M as well as at the *M* point, reflecting the formation of an in-plane $\sqrt{3}a \times \sqrt{3}a$ superlattice structure between the TiS_2 layers. Photon-energy-dependent ARPES measurements further reveal that both the Fe 3*d* and S 3*p* bands disperse along the Γ-*A* (k_z) direction. Notably, the Fe 3*d* band shows a periodicity half that of the S 3*p* band, consistent with the formation of a 2*c* superlattice structure along the out-of-plane direction.

Figure 2 presents Ti 2*p* XAS spectra of Fe_xTiS_2 ($0 \leq x \leq 0.33$) measured at 300 K. The spectral line shape evolves continuously with increasing Fe concentration. For $x = 0$ (TiS_2), the Ti $2p_{3/2}$ absorption region exhibits two peaks at 456.4 and 458.6 eV. As the Fe content increases, the lower-energy peak intensity decreases and becomes a shoulder at $x = 0.33$. In the Ti $2p_{1/2}$ region, two peaks at 462.2 and 464.3 eV for $x = 0$ gradually merge into a single peak at $x = 0.33$ due to enhanced spectral weight between them. The spectral

shape at $x = 0$ closely resembles that of $CaTiO_3$ (Ti^{4+}) [2], indicating that Ti is nearly tetravalent in TiS_2. In contrast, the spectrum at $x = 0.33$ is similar to that reported for mixed-valent $Y_{0.61}Ca_{0.39}TiO_3$ [2], suggesting the coexistence of Ti^{3+} and Ti^{4+} states. These results indicate that the Ti valence evolves from predominantly Ti^{4+} toward Ti^{3+} with increasing Fe intercalation, in good agreement with the electron-doping behavior inferred from ARPES measurements.

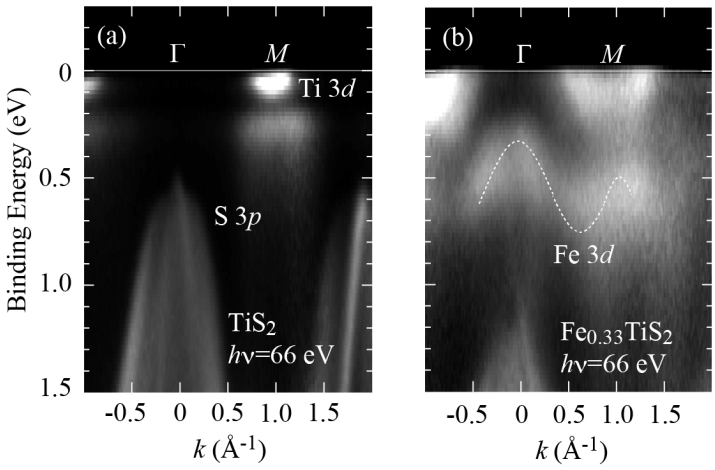

FIGURE 1. ARPES intensity plots of (a) TiS_2 and (b) $Fe_{0.33}TiS_2$ measured at $h\nu = 66$ eV and $T = 20$ K along the Γ-M direction. Dashed line in (b) is guide for the eye for the Fe 3d band.

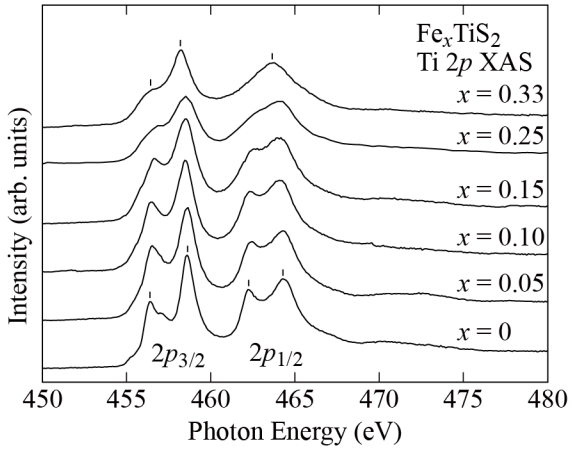

FIGURE 2. Ti 2p XAS spectra of Fe_xTiS_2 ($0 \leq x \leq 0.33$) measured at 300 K.

REFERENCES

1. N. V. Selezneva, E. M. Sherokalova, A. Podlesnyak, M. Frontzek and N. V. Baranov, Phys. Rev. Mater. **7**, 014401 (2023).
2. M. Arita, H. Sato, M. Higashi, K. Yoshikawa, K. Shimada, M. Sawada, Y. Ueda, H. Namatame, M. Taniguchi, S.-i. Fujiomori, Y. Saitoh, M. Tsubota, F. Iga and T. Takabatake, J. Phys. Soc. Jpn. **76**, 074720 (2007).

pH Dependence of Aqueous C2-C4 Dicarboxylic Acids by Soft X-ray Absorption Spectroscopy

Risa Okada[a], Rikuya Adachi[a], Ryosuke Yamamura[a], Taiga Suenaga[a], Takashi Tokushima[b], Masaki Oura[c], Osamu Takahashi[d]

[a]*Chemistry Program, Graduate School of Advanced Science and Engineering, Hiroshima University, 1-3-1 Kagamiyama, Higashihiroshima City, Hiroshima 739-8526, Japan*
[b]*MAX IV Laboratory, Lund University, Fotongatan 2, 224 84 Lund, Sweden*
[c]*RIKEN SPring-8 Center, Sayo-Cho, Sayo, Hyogo 679-5148, Japan*
[d] *Research Institute for Synchrotron Radiation Science, Hiroshima University, 2-313 Kagamiyama, Higashihiroshima City, Hiroshima 739-0046, Japan*

Keywords: Soft X-ray absorption spectroscopy, DFT, Intramolecular hydrogen bond

Soft X-ray absorption spectroscopy (XAS) is a spectroscopic technique that observes the excitation of inner-shell electrons to outer shells when X-rays are incident on a material. Because the absorption energy varies significantly depending on the element, element-selective excitation is possible. Since the 21st century, advances in measurement technology have enabled spectral measurements of soft X-ray absorption spectroscopy in liquid samples. XAS studies have been conducted on liquid samples such as water, alcohols, and aqueous solutions of organic acids. The behavior of substances in liquids is more complex than in the gas phase or solid state owing to intermolecular interactions. Furthermore, by varying the pH of the solution, changes due to the valence states can be observed. Our research group previously reported that the peak shift observed at approximately 532 eV in the pH-dependent XAS spectrum of oxalic acid, originating from the carbonyl oxygen, indicates resonance effects between the two carboxyl groups [1]. In this study, following the oxalic acid work, we targeted malonic, succinic, and maleic acids as our molecules of interest. Dicarboxylic acids play a crucial role in the metabolic pathways of living organisms. They also exist in the atmosphere and soil, with low-molecular-weight dicarboxylic acids such as oxalic, malonic, and succinic acids being abundant in atmospheric aerosols. Theoretical calculations of the pH-dependent XAS spectra of aqueous solutions of malonic, succinic, and maleic acids were performed, and the spectra were analyzed.

After conducting conformational searches using the CONFLEX program, structural optimization and vibrational frequency calculations were performed using Gaussian. The most stable conformation was determined by comparing the energies of the different conformations. To account for stabilization via hydrogen bonding with water molecules, conformational search calculations were performed for one dicarboxylic acid molecule and multiple water molecules in the system.

MD simulations were conducted using GROMACS. The force constants for bond stretching and bending, and bond angle changes required for the simulation were calculated by plotting the energy change when the bond length was varied by 0.01 Å or the bond angle by 2° and, then fitting the data to a quadratic function. The

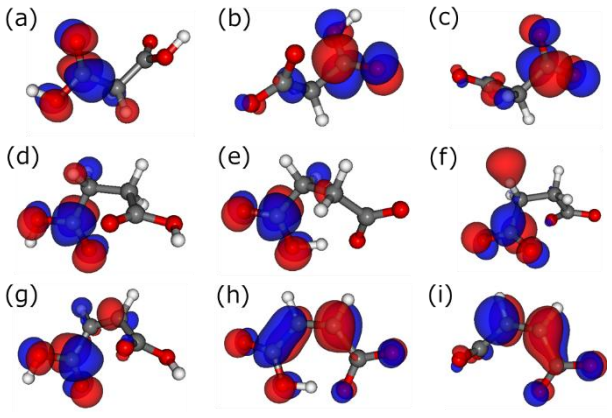

FIGURE 1. π* orbital of (a) neutral (b) anionic (c) dianionic malonic acid and (d) neutral (e) anionic (f) dianionic succinic acid and (g) neutral (h) anionic (i) dianionic maleic acid.

charge parameters were obtained using the RESP method with Gaussian. Simulations were performed at 300 K with a time step of 0.1 fs for 20 ps in the NVT ensemble, followed by 10 ns in the NPT ensemble. From the MD simulation results, a cluster structure composed of one dicarboxylic acid molecule and surrounding water molecules was obtained. XAS calculations were performed using deMon2k. The obtained line spectrum was convolved with a Gaussian function and averaged to obtain the theoretical spectrum.

Figure 1 shows the most stable conformations and π* orbitals of the excited states of neutral, anionic, and dianionic malonic, succinic, and maleic acids. For neutral maleic acid, the conformation with intramolecular hydrogen bonding was the most stable in a single molecule. However, when water molecules were arranged around it, the conformation without intramolecular hydrogen bonding became stable because of stabilization via hydrogen bonding with the water molecules. Figure 2 shows the XAS spectra obtained for the most stable conformations. Theoretical calculations reproduced the relative energy of the first peak in the XAS spectrum. With increasing pH, a high-energy shift of approximately 0.3 eV was observed in the malonic acid aqueous solution and approximately 0.2 eV in the succinic acid aqueous solution, respectively. This is thought to result from the deprotonation of the carboxyl group, similar to the behavior observed in acetic acid aqueous solutions [2]. In contrast, in the maleic acid aqueous solution, the peak for anionic maleic acid appeared at a lower energy than the peaks for neutral and dianionic maleic acids. This differs from the spectrum of oxalic acid aqueous solution, where those for dianionic oxalic acid shows a large high-energy shift. This peak behavior is thought to result from the stereoisomerism adopted by maleic acid in aqueous solutions, which varies with its valence. Anionic maleic acid adopts a planar conformation owing to intramolecular hydrogen bonding, leading to delocalization of the π* orbital via resonance (Figure 1). Consequently, compared to neutral and dianionic maleic acids where no π* orbital resonance is observed owing to the twisting of the carboxyl group, the peak of anionic maleic acid appears at a lower energy. Malonic and succinic acids did not adopt planar conformation. Consequently, the π* orbital localizes on one side of the carboxyl group, and thus, it does not exhibit the same peak behavior as maleic acid. The steric arrangement between the two carboxyl groups is thought to contribute to the peak behavior observed in the pH-dependent XAS spectra.

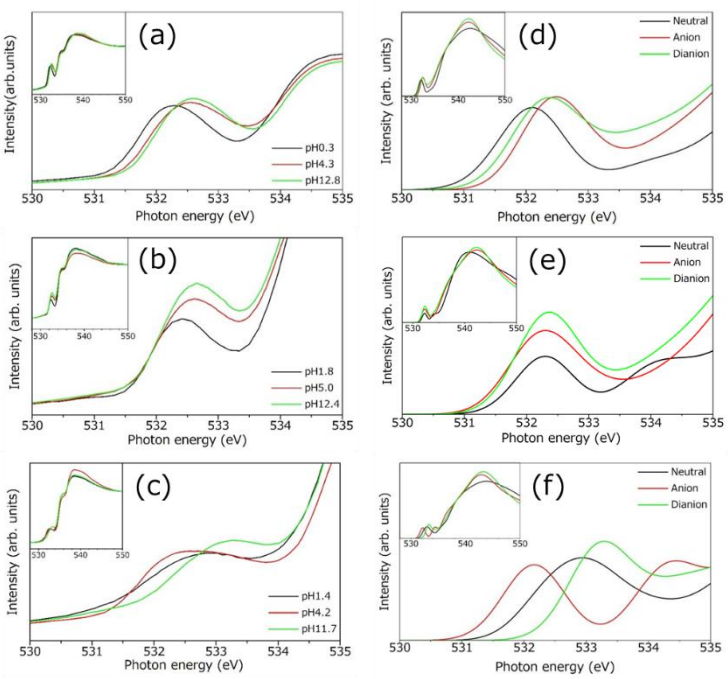

FIGURE 2. Experimental XAS spectra of aqueous (a)malonic (b)succinic (c)maleic acid and theoretical XAS spectra of aqueous (d)malonic (e)succinic (f)maleic acid.

REFERENCES

1. Y. Horikawa, T. Tokushima, Y. Harada, O. Takahashi, A. Chainani, Y. Senba, H. Ohashi, A. Hiraya and S. Shin, Identification of valence electronic states of aqueous acetic acid in acid–base equilibrium using site-selective X-ray emission spectroscopy, *Phys. Chem. Chem. Phys*., **11**, 8676-8679 (2009).
2. R. Yamamura, T. Suenaga, M. Oura, T. Tokushima and O. Takahashi, pH dependence of aqueous oxalic acid observed by X-ray absorption and emission spectroscopy, *Chem. Phys. Lett*., **738**, 136895 (2020).

Hydrogen Bonding Behavior in Response to Concentration Changes in Mixed Solutions of Water and Organic Compounds

Koki Ozeki[a] and Osamu Takahashi[b]

[a]*Graduate School of Advanced Science and Engineering, Hiroshima University.*
[b]*Research Institute for Synchrotron Radiation Science, Hiroshima University.*

Keywords: Molecular dynamics (MD) simulation, Fourier Transform Infrared Spectroscopy (FT-IR), X-ray absorption spectroscopy (XAS), computational chemistry

Aqueous mixtures are complexly intermingled within a solution owing to the effects of intermolecular interactions and polarization effects. Among these, hydrogen bonding is extremely important in governing the physicochemical properties of aqueous solutions. A deeper understanding of its nature is expected to lead to applications in various research fields. In this study, we investigated the behavior of hydrogen bonds in mixtures of water and organic compounds using Fourier-transform infrared spectroscopy (FTIR) and theoretical calculations. Pyridine and 3-methylpyridine (3MP) were selected as the organic compounds. For these compounds, it is known that OH...N hydrogen bonds are forming between the nitrogen atom bearing the nonbonding electron pair on the pyridine ring and the water molecules in the aqueous solution.

First, attenuated total reflection (ATR) FT-IR measurements were performed using water/3MP mixed solutions at various concentrations. As the water ratio increased, the in-plane angular vibration peak of the pyridine ring corresponding to the 1029 cm^{-1} vibration (Figure 1) shifted to the high-frequency side. This peak shift was also observed in other organic compounds containing a pyridine ring. Because hydrogen bonds formed with smaller dipole moments are weaker, experiments using chloroform as the solvent were conducted. The peak shift was smaller than that observed with water, leading us to conclude that this peak change is attributable to hydrogen bonding.

Next, multiple aqueous solution models (50,000 molecules in total) were created by varying the concentrations of water and pyridine molecules. Molecular dynamics (MD) simulations were then performed under NPT ensembles at room temperature. After equilibration, calculating the solution concentrations revealed discrepancies between the simulated values and experimental data. Therefore, we introduced the Charge-On-Particle (COP) model and reran the MD simulations. The results showed less molecular bias compared to before introducing the COP model, and the solution density values were closer to the experimental values, achieving more accurate solution modeling (Figure2).

Additionally, we constructed an apparatus for measuring X-ray absorption spectroscopy (XAS) of liquid samples at HiSOR's BL-6 (Figure3). Moving forward, we aim to advance research on the concentration dependence of water and organic compounds in XAS from both computational and experimental perspectives.

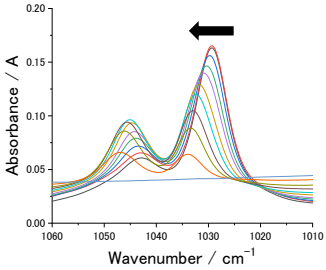

Figure1 ATR FT-IR spectra of water/3MP mixture

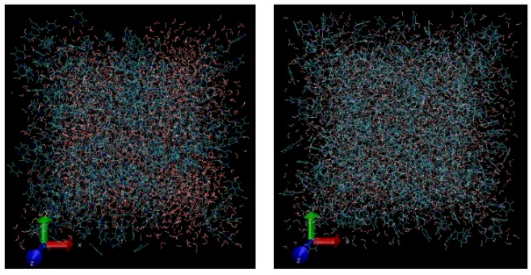

Figure2 Water solution model before cop model implementation (left) and after implementation (right)

Figure3 BL-6 Experimental Facility

Development of a liquid-filled cell for HiSOR BL06

Misaki Kitajima[a], Yuka Horikawa[a], Hiroaki Yoshida[b], Takashi Tokushima[c] and Osamu Takahashi[d]

[a]*Graduate School of Sciences and Technology for Innovation, Yamaguchi Univ.*
1677-1 Yoshida, Yamaguchi, Yamaguchi 753-8512 Japan
[b]*Graduate School of Advanced Science and Engineering, Hiroshima University*
1-3-1 Kagamiyama, Higashi-Hiroshima, Hiroshima 739-8526 Japan
[c]*MAX,IV Laboratory, Lund University*
Fotongatan 2, 224 84 Lund, Sweden
[d]*Research Institute for Synchrotron Radiation Science, Hiroshima University*
1-3-1 Kagamiyama, Higashi-Hiroshima, Hiroshima 739-8526 Japan

Keywords: Liquid-filled cell, Saturation effect correction.

The development of soft X-ray-transmissive thin-film windows has brought significant advancements to soft X-ray absorption spectroscopy (XAS) of liquids. Currently, several methods are employed: SPring-8 BL17SU and NanoTerasu BL07 utilize solution flow cells to measure fluorescence yield through a single window. In contrast, UVSOR BL03U uses a transmission-type cell with two windows sandwiching a thin liquid layer to measure light transmittance. While solution flow cells allow for easy sample exchange under atmospheric pressure, they require large sample volumes for pumping and suffer from spectral distortion due to the saturation effect. Conversely, while transmission-type cells provide true spectral shapes following the Beer-Lambert law, controlling the gas pressure to adjust the liquid film thickness remains a challenge.

To address these issues, we designed a liquid cell for HiSOR BL06 that enables easy installation with minimal sample volume while allowing for the correction of spectral distortion. First, we adopted a sealed-cell structure. By eliminating pump-driven flow, we removed concerns regarding liquid leakage and cleaning during sample exchange, thereby minimizing the required sample volume. To facilitate rapid sample replacement, the area surrounding the cell is housed in a low-vacuum chamber, allowing for easy vacuum purging and evacuation during measurements. Furthermore, to introduce soft X-rays propagating through high vacuum, the end of the high-vacuum chamber was designed with a nozzle shape, using a thin film at the tip to partition the high-vacuum and low-vacuum sections.

The system is designed for fluorescence yield (FY) measurements using photodiodes (PDs). By installing two PDs, we increased the signal intensity and enabled the correction of the saturation effect by varying their installation angles. We have previously demonstrated that by formulating the fluorescence intensity measured by a PD, the correct absorption spectrum can be retrieved from experimental spectra using concentration-dependent data [1]. This method allows us to determine parameters representing the degree of spectral distortion—governed by experimental conditions (such as the PD angle and solid angle) and the solvent—thereby correcting the observed spectra.

However, concentration-based correction has limitations: the molecular state may change with concentration, and preparing multiple samples is costly. Therefore, we have attempted a new approach: performing measurements at different fluorescence detection angles to enable spectral shape correction using a single sample in a single experimental setup.

Figure 1 shows O K-edge XA spectra of acetic acid in hexane solution normalized by heights of the first resonance peak (a) and the spectra after correction for saturation effects (b) [1]. The width of the first resonance peak around 532.2 eV is all the same after saturation correction, indicating that the correction is successful.

Figure 2 shows schematic diagram of the BL06 terminal equipment (left) and a photo of the low-vacuum chamber (right).

Figure 3 shows the cross-section of soft X-ray emission nozzle and photodiode mount installed in the low vacuum chamber. By setting the detection angles to 40° and 80°, two types of absorption spectra are acquired, and correction is performed using these two data.

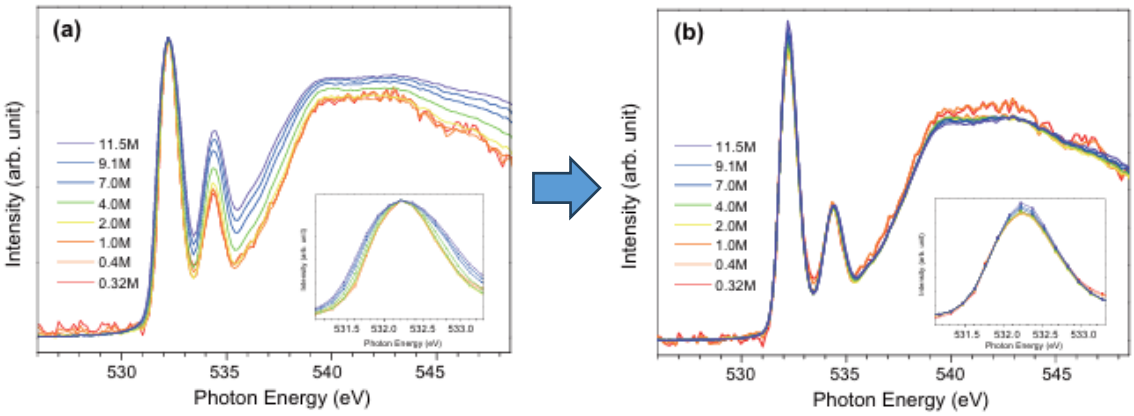

FIGURE 1. (a) O K-edge XA spectra of acetic acid in hexane solution normalized by heights of the first resonance peak. (b) The spectra after correction for saturation effects. [1]

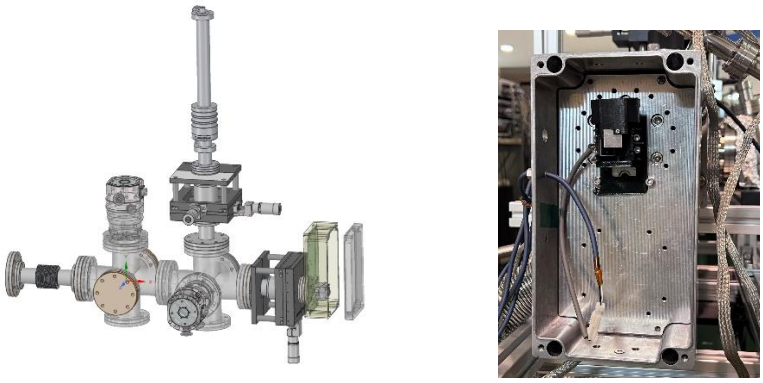

FIGURE 2. Schematic diagram of the BL06 terminal equipment (left) and a photo of the low-vacuum chamber (right)

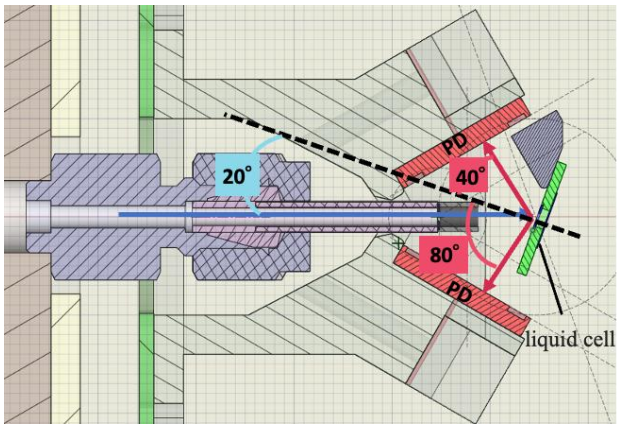

FIGURE 3. Cross-section of soft X-ray emission nozzle and photodiode mount

REFERENCES

1. Y. Horikawa, H. Arai, T. Tokushima and S. Shin, *Chemical Physics Letters* **522**, 33 (2012).

Thickness Dependence of Electronic Structure of Bi Thin Films on Au(111)

N. Nishimoto [a], H. Yamaguchi [b], T. Asano [b], Y. Fujisawa [c], K. Sumida [c], H. Sato [c], K. Miyamoto [c] and T. Okuda [c,d,e]

[a] *Department of Physics, Faculty of Science, Hiroshima University, 1-3-1 Kagamiyama, Higashi-Hiroshima 739-8526, Japan.*
[b] *Graduate School of Advanced Science and Engineering, Hiroshima University, 1-3-1 Kagamiyama, Higashi-Hiroshima 739-8526, Japan.*
[c] *Research Institute for Synchrotron Radiation Science, Hiroshima University, 1-3-1 Kagamiyama, Higashi-Hiroshima 739-8526, Japan.*
[d] *International Institute for Sustainability with Knotted Chiral Meta Matter (SKCM²), Hiroshima University, 1-3-1 Kagamiyama, Hiroshima 739-8526, Japan.*
[e] *Research Institute for Semiconductor Engineering (RISE), Hiroshima University, 1-4-2 Kagamiyama, Higashi-Hiroshima, 739-8527, Japan.*

Keywords: Spin-Orbit Coupling, Quasi-one-dimensional structure, ARPES

Bismuth (Bi) is a heavy element and has been extensively studied in solid-state physics due to its unique electronic properties arising from its strong spin-orbit coupling (SOC). In monolayer and few-layer Bi ultra-thin films, strong SOC is predicted to induce band inversion, causing a phase transition from a semi-metallic state to a two-dimensional topological insulator [1]. While it is well known that Bi forms surface alloys with giant Rashba splitting on Ag(111) and Cu(111) substrates [2,3], the growth of Bi on Au(111) exhibits a distinct behavior. Instead of alloying, Bi on Au(111) forms various complex surface structures depending on the coverage [4]. Although reported coverage values vary in the literature, it is generally accepted that a (5×5) low-temperature adsorption phase is formed below 0.6 ML, a $\left(\sqrt{37} \times \sqrt{37}\right)R25.3^{\circ}$ structure is formed up to 0.8 ML, and a quasi-one-dimensional $(p \times \sqrt{3})$ stripe structure is formed up to 1 ML. In the thick film regime, Bi(110) is formed. Regarding the $(p \times \sqrt{3})$ structure, previous studies have proposed a long-period Moiré model in which the periodicity p evolves as 5, 8, 11, and 14 with increasing coverage [5]. In this study, we aimed to comprehensively elucidate the relationship between surface structures and electronic structures in the Bi/Au(111) system.

A clean Au(111) surface was obtained by repeated cycles of Ar-ion sputtering (1.5 kV) and annealing (1000 K). Bi deposition was performed by molecular beam epitaxy (MBE) using a Knudsen cell (K-cell) under ultra-high vacuum conditions ($\sim 10^{-8}$ Pa). We identified the surface structures by comparing experimental Low-Energy Electron Diffraction (LEED) patterns with simulations based on structural models from previous studies. Specifically, the periodicity p of the $(p \times \sqrt{3})$ structures was identified based on the relative size of the characteristic triangular patterns observed in the LEED images (Figure 1(a)-(c)). The Angle-Resolved Photoemission Spectroscopy (ARPES) measurements were carried out at HiSOR BL-7 using p-polarized light with photon energies of $h\nu = 20 \sim 70$ eV at temperatures below 100 K.

ARPES results revealed a Bi-derived surface state band (SSB) within the projected bulk band gap of Au, located near the $\overline{\mathrm{K}}$ point. We clarified that the SSB systematically shifts to larger k-values as the periodicity p increases (Figure 2(a)-(d)). Furthermore, the constant energy contour exhibits a triangular shape centered at the $\overline{\mathrm{K}}$ point. Regarding the dispersion along the k_y direction (parallel to the stripes), we revealed that it forms a characteristic band structure where electron-like and hole-like bands overlap and disperses with a variation in effective mass as k_x (perpendicular to the stripes) increases (Figure 3). In addition, we investigated the electronic states of other surface structures and compared the experimental results with band calculations. The details will be discussed in the poster presentation.

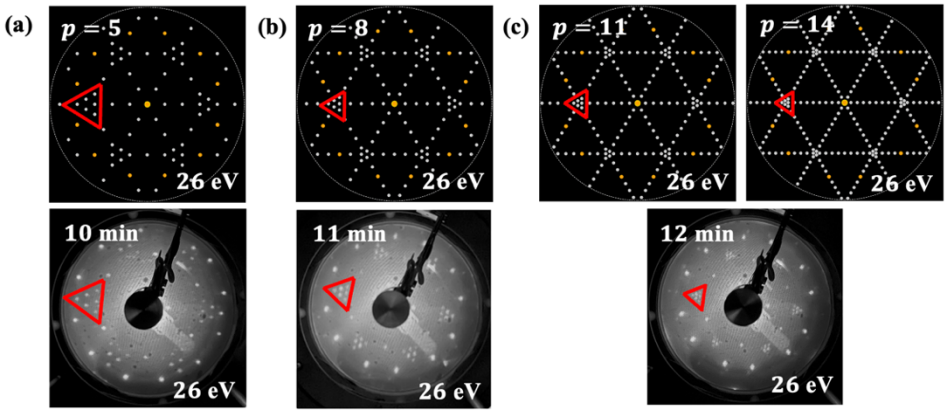

Figure 1. Comparison between experimental and simulated LEED patterns: (a) $(5 \times \sqrt{3})$; (b) $(8 \times \sqrt{3})$; (c) $(14 \times \sqrt{3})$

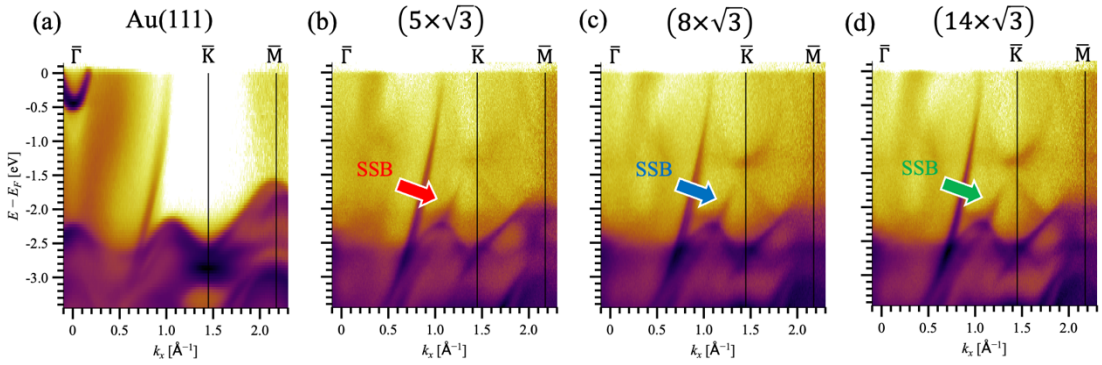

Figure 2. ARPES spectra measured at $h\nu = 44$eV along the $\bar{\Gamma} - \bar{\mathrm{K}} - \bar{\mathrm{M}}$(Au) direction: (a) $(5 \times \sqrt{3})$; (b) $(8 \times \sqrt{3})$; (c) $(14 \times \sqrt{3})$

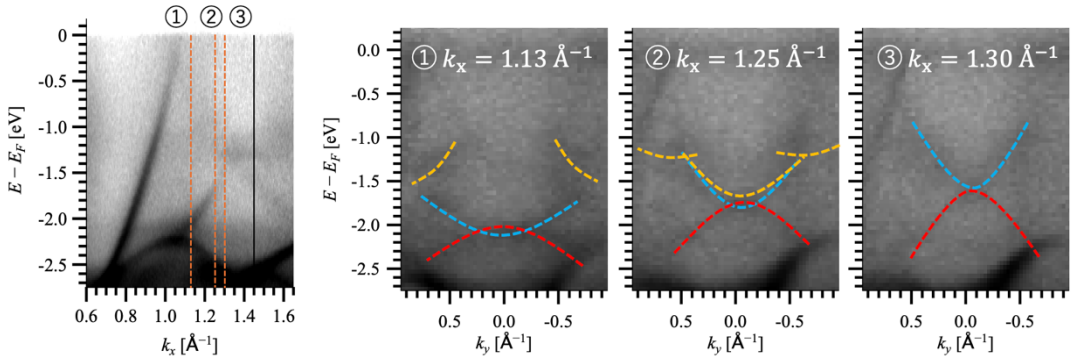

Figure 3. ARPES spectra of the $(5 \times \sqrt{3})$ structure along the k_y direction measured at the k_x positions indicated by ①–③.

REFERENCES

1. S. Murakami, Phys. Rev. Lett. **97**, 236805 (2006).
2. C. R. Ast, J. Henk, A. Ernst, L. Moreschini, M. C. Falub, D. Pacilé, P. Bruno, K. Kern, and M. Grioni, Phys. Rev. Lett. **98**, 186807 (2007).
3. H. Bentmann, T. Kuzumaki, G. Bihlmayer, S. Blügel, E. V. Chulkov, F. Reinert, and K. Sakamoto, Phys. Rev. B **84**, 115426 (2011).
4. N. Kawakami, C.-L. Lin, K. Kawahara, M. Kawai, R. Arafune, and N. Takagi, Phys. Rev. B **96**, 205402 (2017).
5. P. V. Vicente, T. Weiss, D. Meier, W. Zhao, S. Tömekce, M. G. Cuxart, B. P. Klein, D. A. Duncan, T.-L. Lee, A. C. Papageorgiou, M. Muntwiler, A. P. Seitsonen, W. Auwärter, P. Feulner, J. V. Barth, and F. Allegretti, Phys. Rev. Materials **8**, 104001 (2024).

Substrate and Thickness Dependence of Anisotropic Topological Surface States of Bi_2Te_3 Thin Films

R. Yamamoto[a], Y. Fujisawa[b], K. Sumida[b], K. Miyamoto[b], and T. Okuda[b,c,d].

[a]*Graduate School of Advanced Science and Engineering Hiroshima University, 1-3-1 Kagamiyama Higashi-Hiroshima 739-8526, Japan*
[b]*Research Institute for Synchrotron Radiation Science (HiSOR), Hiroshima University, 2-313 Kagamiyama, Higashi-Hiroshima 739-0046, Japan*
[c]*International Institute for Sustainability with Knotted Chiral Meta Matter (WPI-SCKM2), Hiroshima University, 2-313 Kagamiyama, Higashi-Hiroshima 739-0046, Japan*
[d]*Research Institute for Semiconductor Engineering (RISE), Hiroshima University, 1-4-2 Kagamiyama, Higashi-Hiroshima 739-8527, Japan*

Keywords: Enter keywords. Topological surface states, Vicinal Si surface, Anisotropy of band structure, Bi_2Te_3 film

Topological insulators (TIs) have spin-polarized metallic surface states called topological surface states (TSS). As in Fig. 1(a), in TSS, the spin direction of electrons is locked by their momentum resulting in the helical spin-texture. The unique helical spin-texture is considered to prohibit complete backscattering by non-magnetic impurities. This property is expected to realize long spin coherent length and applied for spintronics devices. However, other backscattering passes except for the complete backscattering are not prohibited completely [Fig.1(a)]. One possible approach to overcome this problem is to modify the surface band structure into an anisotropic form [Fig.1 (b)]. An anisotropic surface band can deform the spin texture into a configuration that further suppresses backscattering, potentially extending the average spin relaxation length. Furthermore, if an ideal one-dimensional anisotropic band structure could be realized, all backscattering processes would be completely prohibited [Fig. 1(c)].

It is reported that Bi_2Te_3, representative TI, can be grown as thin films on Si(111) surface and its band dispersion exhibits a clear thickness dependence [1]. In addition, studies on the Au(788) surface, which exhibits a regular one-dimensional step array of the Au(111) plane, have demonstrated the discretized one-dimensional band dispersion induced by quantum confinement effects [2]. Therefore, by depositing Bi_2Te_3 on the substrate possessing one-dimensional step array of Si(111) plane, it is expected that anisotropic one-dimensional TSS induced by confinement effect as same as Au(788) is observed. In this study, Bi_2Te_3 was deposited on a Si(557) substrate featuring a Si(111) step array with a terrace width of approximately 1.8 nm. We aimed to realize a one-dimensional Bi_2Te_3 crystal structure and to investigate the resulting modulation of its topological surface states.

Sample preparation and measurements were performed at beamline BL-9B of HiSOR. Bi_2Te_3 thin films were grown on both Si(111) and Si(557) substrates. To investigate thickness dependence, we attempted to fabricate wedge-shaped Bi_2Te_3 films. After the growth, the surface band structure was measured by angle-resolved photoemission spectroscopy (ARPES).

Fig. 2(a) and (b) show the Fermi surface of 6-QL Bi_2Te_3 films grown on Si(111) and Si(557) substrates, respectively. For the film on Si(111), an isotropic hexagonal Fermi surface with warping was clearly observed. On the Si(557) substrate, although an anisotropic Fermi surface was expected, no clear anisotropy was also detected.

It has been reported that the wave function of the topological surface states in Bi_2Te_3 extends more than approximately 1 nm from the crystal surface [3]. Since the step height of a typical Si(557) substrate is about 0.32 nm, which is smaller than the spatial extent of the Bi_2Te_3 surface-state wave function, the confinement effect might have been insufficient, resulting in an apparently isotropic band structure. To enhance the confinement potential between steps, we intentionally induced a step bunching on the Si(557) substrate, which is expected to increase the substrate-derived step potential and strengthen the confinement effect. Step bunching was successfully obtained by annealing the Si(557) substrate at 850 °C for 1.5 hours after flash annealing.

Fig. 2(c) shows the Fermi surface of the 6-QL Bi_2Te_3 film grown on the bunched Si(557) substrate. Unlike the case of the non-bunched Si(557) substrate, a clear anisotropy is observed. These results demonstrate that anisotropic topological surface states were successfully realized on the bunched Si(557) substrate. In addition, we investigated the thickness dependence of the anisotropy using wedge-shaped Bi_2Te_3 films. As a result, stronger anisotropy is observed in the 1-QL film than in the 6-QL film, suggesting stronger confinement of the TSS in the thinner film.

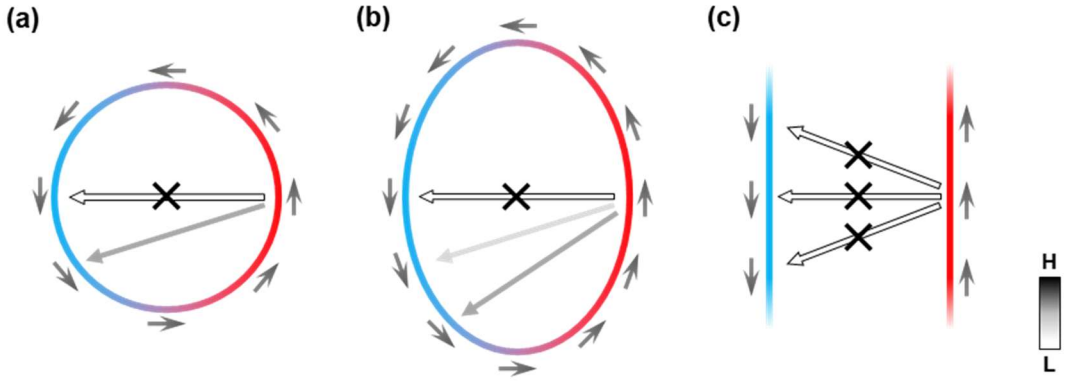

FIGURE 1. Schematic spin-texture of (a) isotropic, (b) anisotropic, and (c) one-dimensional Fermi surfaces (c) of topological insulators.

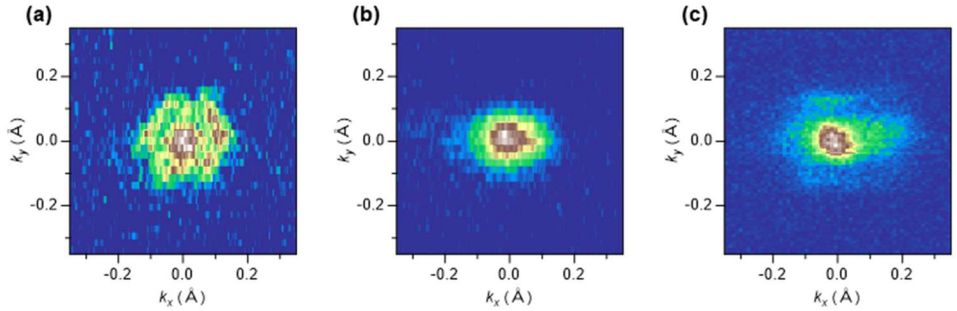

FIGURE 2. The Fermi surface of 6-QL Bi_2Te_3 film grown on (a)Si(111), (b)Si(557) and (c)bunched Si(557).

REFERENCES

[1] S. Hatta *et al.* Sci Rep. **11**, 5742 (2021).
[2] A, Mugarza *et al*., Phys. Rev. Lett. **87**, 107601 (2001).
[3] Sergey V. Eremeev *et al*., nat. commun. **3**, 635 (2012).

Development of Spin-ARPES for Electric-Field Response

T. Asano[a] , Y. Fujisawa[b], K. Sumida[b], T. Okuda[b,c,d], K. Miyamoto[b]

[a] *Graduate School of Advanced Science and Engineering, Hiroshima University, 1-3-1 Kagamiyama, Higashi-Hiroshima 739-8526, Japan.*
[b] *Research Institute for Synchrotron Radiation Science (HiSOR), Hiroshima University 2-313 Kagamiyama, Higashi-Hiroshima 739-0046, Japan.*
[c] *International Institute for Sustainability with Knotted Chiral Meta Matter (SKCM^2), Hiroshima University, 1-3-1 Kagamiyama, Hiroshima 739-8526, Japan.*
[d] *Research Institute for Semiconductor Engineering (RISE), Hiroshima University, 1-4-2 Kagamiyama, Higashi-Hiroshima, 739-8527, Japan.*

Keywords: Spin-ARPES, Electric-Field Response, Spin Hall effect, Lock-in system.

Spin-ARPES using synchrotron radiation is a well-established and powerful method for observing spin-dependent electronic structures in equilibrium conditions. Recently, *operando* spin-ARPES under static electric fields has been reported [1], demonstrating the possibility of probing electronic structures under an applied electric bias.

However, expanding such approaches to dynamic measurements remains highly challenging. This is because only a very small fraction of electrons participates in spin-transport dynamics, whereas most electrons contribute only to the equilibrium electronic background. As a result, the electric-field-induced spin accumulation, for example in spin Hall effect, appears as an extremely weak component buried in a large equilibrium background, making its direct detection intrinsically difficult.

To overcome this limitation, we developed a spin-ARPES system capable of probing electric-field-induced spin accumulation in spin Hall effect under current modulation. To extract the minute spin-dependent response synchronized with the applied periodic electric field, we implemented a digital lock-in analysis scheme in both hardware and software. This approach enables selective detection of the periodic component associated with the spin accumulation while suppressing the overwhelming equilibrium background.

To demonstrate the feasibility of this approach, we applied this methodology to a polycrystalline Pt thin film, a prototypical material exhibiting a strong spin Hall effect [2]. By analyzing the synchronized signal in the complex plane, we extracted both its amplitude and phase. Experimental results and quantitative analysis will be presented in the poster.

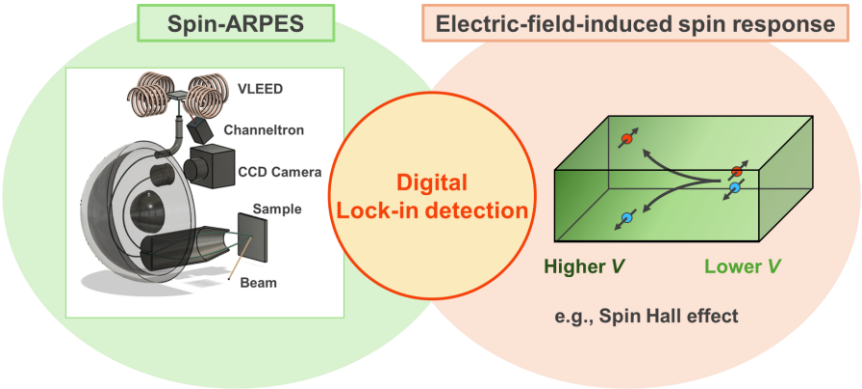

FIGURE 1. Conceptual diagram of current-modulated spin-ARPES.
Digital lock-in detection bridges spin-ARPES measurements and electric-field-induced spin accumulation associated with the

Spin Hall effect.

REFERENCES

1. J. Krempaský, et al., Phys. Rev. X **8**, 021067 (2018).
2. G. Y. Guo, *et al*., Phys. Rev. Lett. **100**, 096401 (2008).

VUV-CD Imaging of LLPS Proteins

Kentaro FUJII[a], Kuya AOYAMA[b], Nobuo MAITA[a], Masato KATO[a], Hideaki IWASAWA[c], Koichi MATSUO[b]

a1:Institute for Quantum Life Science, National Institutes for Quantum Science and Technology (QST)

b2:HiSOR, Hiroshima University

c:Synchrotron Radiation Research center, National Institutes for Quantum Science and Technology (QST)

Keywords: Liquid-Liquid Phase Separation (LLPS), VUV-CD, microscopy

Proteins that undergo liquid–liquid phase separation (LLPS), such as (FUS), have been implicated in neurodegenerative diseases like amyotrophic lateral sclerosis (ALS) and frontotemporal dementia (FTD) [1, 2]. However, the relationship between phase separation behavior and protein structure remains poorly understood. Clarifying how protein structural properties relate to their droplet state is essential for advancing knowledge of the molecular mechanisms underlying these diseases.

Our recent studies using vacuum-ultraviolet circular dichroism (VUV-CD) spectroscopy have demonstrated that the structure of FUS-LC changes in response to LLPS [3]. In the dispersed state, the protein is predominantly disordered, while its β-strand content increases upon phase separation. The emergence and development of amyloid-like β-structures into fibrillar assemblies are believed to contribute to the pathogenesis of neurodegenerative diseases. However, direct evidence linking these structural transitions to disease mechanisms remains lacking. A significant limitation has been the millimeter-scale footprint of the synchrotron radiation beam used for CD measurements, which has hindered quantitative evaluation of structural changes specifically within the droplets.

This study analyzed structural changes within FUS droplets using a synchrotron microbeam with a diameter smaller than the droplet size. The droplet state of FUS was reproduced, and scanning measurements were conducted using the newly installed microbeam VUV-CD imaging system at BL12. Protein samples were prepared to remain dispersed at room temperature and to form droplets below 5℃. The droplets were also observed by an optical microscope (Figure). The sample cell was scanned with a VUV beam focused to several tens of micrometers. CD spectra were successfully obtained from regions presumed to be within the droplets. Ongoing experimental trials aim to quantify changes in CD spectral intensity within the droplet phase.

FIGURE 1. The picture of LLPS of FUS-LC below 5°C.

REFERENCES

1. M. Kato, et al., Cell **149** (2018)753-767.
2. Y. Lin, et al., Proc. Nat. Aca. Sci. **17** (2020) 28727-28734.
3. K. Fujii, et al., Chrality, **36** (2024) e23707.

Variation of Absorption Spectra of Aqueous DMSO Solutions Measured by the Ultraviolet–Attenuated-Total-Reflection Method

Chika Sugahara[a], Koichi Matsuo[a,b] and Kazumasa Okada[a,b]

[a] *Graduate School of Advanced Science and Engineering, Hiroshima University, 1-3-1 Kagamiyama, Higashi-Hiroshima 739-8526*
[b] *Research Institute for Synchrotron Radiation Science, Hiroshima University, 2-313 Kagamiyama, Higashi-Hiroshima 739-0046*

Keywords: Ultraviolet–ATR method, aqueous DMSO solution, hydration structure

Dimethyl sulfoxide (DMSO) is a famous solvent for biologists and organic chemists. It is well known that DMSO is miscible with water and has cryoprotection effect. Hydration structure of the aqueous DMSO solution changes greatly with the concentration. In the dilute region, DMSO works as a structure maker of water, but as the concentration increases, it behaves as a structure breaker [1]. The hydration structure has been discussed with various methods [2–4]. The UV absorption spectroscopy can be a good method to reveal the electronic structure of hydrated DMSO. However, large absorption of DMSO in the UV region makes it difficult to measure spectra with conventional methods. To prevent this problem, we employ the ultraviolet–attenuated-total-reflection method. In this study, we measure a series of absorption spectra of aqueous DMSO solutions with a systematic change of the concentration.

The experiments were performed on the beamline for vacuum-ultraviolet circular dichroism spectroscopy, BL-12. We nearly made a housing for a prism with two wings for suppressing stray light. The prism for this study was made of synthetic fused silica and inserted in the housing box in an inverted triangular manner. The box was then placed along the light axis so as to satisfy the total reflection conditions. The samples were dropped on the top face of the prism. Finally, a cover glass was placed on the sample, and the box was closed with a lid. The sample chamber was purged with nitrogen gas. The wavelength range for the measurements was 180–280 nm, and the spectrum of liquid water was used as a reference. The sample of aqueous DMSO solutions was prepared with molar fraction of DMSO ranging from 0.01 to 0.10. The reagent DMSO was obtained commercially from FUJIFILM Wako Pure Chemical Corp., Japan.

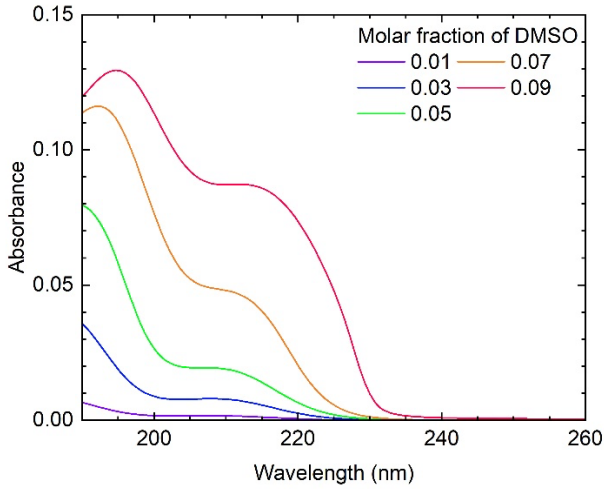

FIGURE 1. Ultraviolet–ATR absorption spectra of aqueous DMSO solutions measured for a series of molar fraction of DMSO.

The obtained spectra have strongly concentration-dependent, as shown in Fig. 1. Two peaks of absorption bands shift to the longer wavelength side in a non-linear way. The spectrum for $x_D = 0.09$ is apparently

different from the others.

Quantitative analysis of spectra is carried out by the principal component analysis (PCA). For analysis, data in the range $x_D < 0.09$, where the intensity of spectra increases monotonically, is used. The results of PCA are shown in Fig. 2. The measured spectra are well explained by three components (PC1–PC3). The primary component (PC1) of the vector resembles the spectrum for $x_D = 0.07$. The score of PC1 would be in a straight line as expected by Beer's law, but the line deviates upward. In fact, the score is proportional to the square of the molar concentration of DMSO. This indicates the existence of the DNSO dimer.

Based on the behavior of the scores, the hydration structure can be divided into three regions. The first region covers the dilute solution under 1.96 mol/L. The second region ranges from 1.96 to 2.81 mol/L. The higher concentration solutions form the third region. The boundaries are in accord with the change in hydration structure reported by Refs. [2–4].

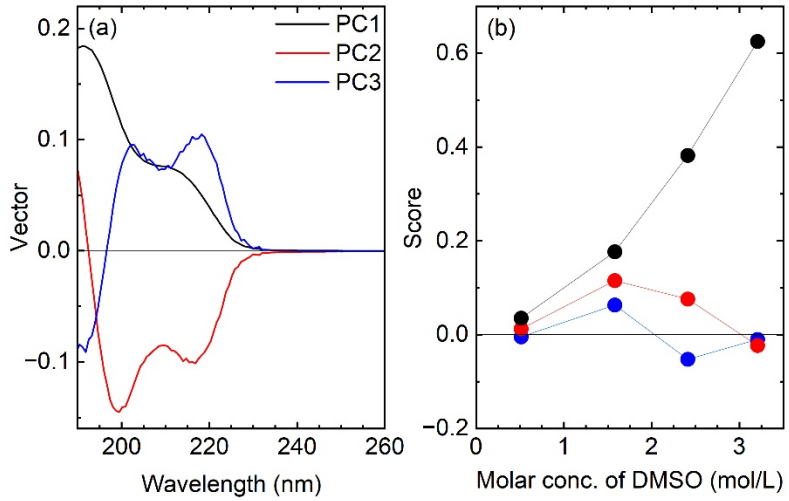

FIGURE 2. Spectral components (a) and scores (b) obtained by PCA for the UV absorption spectral data shown in Fig. 1. The explained variance ratio of PC1–PC3 are 96.2, 2.9 and 0.8%, respectively.

REFERENCES

1. I. I. Vaisman and M. L. Berkowitz, *J. Am. Chem. Soc.* **114**, 7889–7896 (1992).
2. K. Mizuno, S. Imafuji, T. Ochi, T. Ohta and S. Maeda, *J. Phys. Chem. B* **104**, 11001–11005 (2000).
3. D. N. Shin, J. W. Wijnen, J. B. F. N. Engberts and A. Wakisaka, *J. Phys. Chem. B* **105**, 6759–6762 (2001).
4. S. Roy, S. Banerjee, N. Biyani, B. Jana and B. Bagchi, *J. Phys. Chem. B* **115**, 685–692 (2011).
5. K. Matsuo, T. Fukuyama, R. Yonehara, H. Namatame, M. Taniguchi and K. Gekko, *J. Electron Spectrosc. Relat. Phenom.* **144–147**, 1023–1025 (2005).

Development of Vertical-Imaging Circular Dichroism Apparatus for Characterizing the Structure of Aggregated Biomolecules

Kuya Aoyama[a], Satoshi Hashimoto[a], Mohamed Ibrahim[b], and Koichi Matsuo[a,b]

[a]*Graduate School of Advanced Science and Engineering, Hiroshima University*
[b]*Research Institute for Synchrotron Radiation Science, Hiroshima University*

Keywords: Circular Dichroism, Equipment Development

Circular dichroism (CD) measurements in the vacuum-ultraviolet region using synchrotron radiation are widely utilized for the precise structural and functional research of biomolecules in solutions. However, CD measurements of solid and semi-solid biomolecules, such as amyloid fibrils (which are causative materials of Alzheimer's disease), liquid-liquid phase separation involved in cellular and biological function regulation, and polymer hydrogels, remain technically difficult. The reasons are as follows:

1. For solid samples such as aggregates, accurate CD measurements are difficult because anisotropic optical effects, including linear dichroism (LD) and linear birefringence (LB), interfere with the CD signals.

2. Since the beam size is larger than that of the aggregates, the obtained CD spectrum reflects an averaged signal including both aggregated and non-aggregated samples within the beam spot.

In this study, to resolve these issues, we developed vertical-imaging circular dichroism apparatus (ViCD) by the usage of new optical system [1] which can eliminate sample anisotropy and by the installation of focusing mirrors which can minimize the beam spots and realize the spatially resolved measurements.

To verify the performance of the new optical system, first, we measured the CD spectrum of camphor sulfonic acid solution, a standard CD sample, using new system and confirmed an intensity ratio of 1:2 at 290 nm and 190 nm, and second, we measured the CD spectrum of some L-alanine thin films prepared by a vacuum deposition method and confirmed the elimination of anisotropy effects such as LD and LB. Further, we conducted spatially resolved measurements using focusing mirrors for the alginate-gum arabic gel and characterized structurally heterogeneous regions depending on high gum arabic concentration.

These results demonstrate that the ViCD system developed here successfully visualizes the spatial heterogeneity of solid and semi-solid biomolecules without interference from anisotropy.

REFERENCE

1. G. E. Jellison and F. A. Modine "Two-modulator generalized ellipsometry:theory" *Appl. Opt.* **36**(31) 8190-8198 (1997)

Dynamic Structural Study of the Antimicrobial Peptide Magainin 2 Interacting with Membranes by Time-Resolved Circular Dichroism Spectroscopy

Miu Yoshimura[a], Satoshi Hashimoto[b], and Koichi Matsuo[a,b]

[a]*Department of Physics, Faculty of Science, Hiroshima University, 1-3-1 Kagamiyama, Higashi-Hiroshima 739-8526, Japan*
[b]*Research Institute for Synchrotron Radiation Science, Hiroshima University, 2-313 Kagamiyama, Higashi-Hiroshima 739-0046, Japan*

Keywords: Antimicrobial peptide, Magainin 2, Membrane interaction, Secondary structure, Time-resolved measurement, Vacuum-ultraviolet circular dichroism

Antimicrobial peptides (AMPs) have attracted considerable attention as next-generation therapeutic agents to combat antimicrobial resistance. Magainin 2 (M2), originally isolated from the African clawed frog (*Xenopus laevis*)(1), is one of important AMPs and exhibits antimicrobial activity by interacting with bacterial membranes, assembling and forming pores on the membrane surface, which induces the disruption of membrane (2). However, the membrane interaction and pore-formation mechanisms remain controversial, and it is therefore necessary to elucidate the structural changes of M2 upon interaction with the membrane. In this study, we investigated the structural dynamics of M2 interacting with model lipid membranes (composed of phospholipid molecules with anionic or neutral head group) using time-resolved vacuum-ultraviolet circular dichroism (TR-VUVCD) spectroscopy.

M2 peptide and membrane (anionic and neutral) solutions were respectively prepared and the both were rapidly mixed with a microfluidic mixer (3). The CD spectra after mixing were measured in the time range from sub-seconds to several tens of seconds, and exhibited that CD spectra commonly showed that the conformation of M2 changed from a random coil (native, N state) to an α-helix–rich structure (membrane-bound, MB state). However, in the case of anionic membranes, the spectral transition from N to M states completed within 0.2 seconds, while in neutral membranes, the transition to the M state required approximately 70 seconds. Kinetic analysis of the TR data set for the M2-neutral membrane interaction was performed using global fitting, revealing the presence of an intermediate state (I state). Further, the secondary structure analysis showed a stepwise increase in α-helical content in the order of N, I, and M states. To obtain the structural insights and membrane interaction sites at the amino-acid residue level, molecular dynamics (MD) simulations were conducted for the helical structure of M2 in the presence of neutral or anionic membranes (4). The simulation results on the membrane affinity and structural stability of M2, depending on membrane type, were consistent with the TR-VUVCD experimental results. Further, MD simulations disclosed that the electrostatic interactions played crucial roles in the early stage of membrane interaction and the hydrophobic interactions contributed to the formation of stable helical structure of M2 in the membrane. Thus, the integrated TR-VUVCD and MD analyses showed that M2 undergoes distinct membrane interaction mechanisms depending on the charge conditions of lipid headgroups prior to pore formation.

REFERENCES

1. Zasloff, M., *Proc. Natl. Acad. Sci. USA*, **84**, 5449–5453 (1987).
2. Matsuzaki, K., *et al*., *Biochemistry*, **36**, 2104–2111 (1997).
3. Hashimoto, S. and Matsuo, K., *Anal. Chem.*, **96**, 10524–10533 (2024).
4. Kumashiro, M., Izumi, Y., and Matsuo, K., *Proteins*, **89**, 1251–1261 (2021).

Investigation of the Wrapping Mechanism of β-Lactoglobulin Around SDS Micelles by Time-Resolved VUVCD and Molecular Dynamics Simulation

Satoshi Hashimoto[a] and Koichi Matsuo[a,b,c]

[a]*Research Institute for Synchrotron Radiation Science, Hiroshima University, 2-313 Kagamiyama, Higashi-Hiroshima 739-0046, Japan*
[b]*Graduate School of Advanced Science and Engineering, Hiroshima University, 1-3-1 Kagamiyama, Higashi-Hiroshima 739-8526, Japan*
[c]*International Institute for Sustainability with Knotted Chiral Meta Matter (WPI-SKCM^2), Hiroshima University, 2-313 Kagamiyama, Higashi-Hiroshima 739-0046, Japan*

Keywords: Circular dichroism, Interface-induced conformational change, Secondary structures, Time-resolved measurement

Water-soluble proteins often undergo structural transitions induced by interactions with membrane interfaces, expressing biological functions such as drug transport and amyloid fibril formation[1,2]. Surfactants have been widely used as membrane mimics and adapted as a practical model for studying these interactions. In this study, we investigated the interaction between β-lactoglobulin (bLG), a model membrane-binding protein, and sodium dodecyl sulfate (SDS), an anionic surfactant, using time-resolved (TR-) VUVCD to elucidate the structural transition mechanism from the native (N-) to micelle-bound (MB-) state[3,4].

TR-VUVCD spectra of bLG were recorded in the 0.2–120 s range with 0.2 s resolution, revealing a transition from β-strand–rich to α-helix–rich structures (corresponding to N- and MB-states, respectively) (FIGURE). Kinetic analysis identified two intermediates, showing a stepwise increase in helical content. Molecular dynamics (MD) simulations based on these data further clarified the interaction mechanism, where initial electrostatic attraction facilitates approach to the micelle surface, followed by hydrophobic stabilization. These findings enabled us to propose a model for SDS micelle wrapping by bLG.

Our study demonstrates that combining TR-VUVCD and MD simulation is a powerful approach for probing protein–surfactant interactions and membrane-associated protein dynamics.

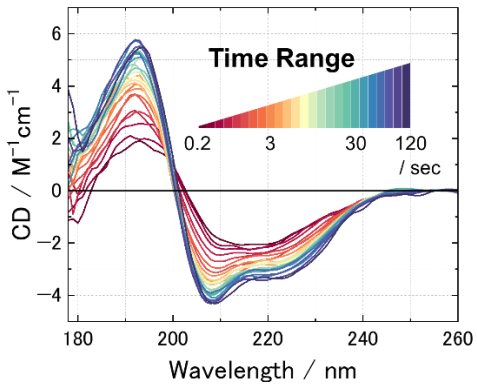

FIGURE. TR-VUVCD spectra of bLG during the interaction with SDS micelles, measured from 0.2 to 120 s.

REFERENCES

1. K. Matsuo, K. Kumashiro, K. Gekko, *Chirality* **32**, 594-604 (2020)
2. R. Imaura, Y. Kawata, K. Matsuo, *Langmuir* **40**, 20537–20549 (2024)
3. S. Hashimoto and K. Matsuo, *Anal. Chem.* **96**, 10524-10533 (2024)
4. J. M. Pedersen, J. Lyngsø, T. Zinn, D. E. Otzen, J. S. Pedersen, *Chem. Sci.* **11**, 699-712 (2020)

Tracking Calcium-Induced Assembly and Phase Transitions in Sodium Alginate via Circular Dichroism

Tatsuki Haga[a], Satoshi Hashimoto[a], Masaya Yoshida[b], Yudai Ono[b], Takeharu Haino[b], Yasuyuki Maki[c], Koichi Matsuo[a,d], Mohamed Ibrahim[d]

[a]*Graduate School of Advanced Science and Engineering, Hiroshima University, Higashi-Hiroshima 739-8526, Japan.*
[b]*Department of Chemistry, Graduate School of Advanced Science and Engineering, Hiroshima University, Higashi-Hiroshima 739-8526, Japan.*
[c]*Faculty of Science, Kyushu University, Fukuoka 819-0395, Japan.*
[d]*Research Institute for Synchrotron Radiation Science, HiSOR, Hiroshima University, Higashi-Hiroshima 739-0046, Japan.*

Keywords: Sodium alginate, Synchrotron radiation, Hydrogel assembly, Phase diagram.

Sodium alginate (SA) forms ionically crosslinked hydrogels in the presence of divalent cations through coordination with guluronic acid (G) blocks [1-2]. Despite extensive studies on alginate gelation, the early - molecular events governing nucleation and intermediate assembly remain insufficiently understood due to the limited sensitivity of conventional techniques to early-stage conformational changes [3-5].

In this work, conventional circular dichroism (CD) and synchrotron radiation circular dichroism (SRCD) were used to monitor Ca^{2+}-induced conformational changes and phase transitions of SA in solution and hydrogel states.

The mannuronic/guluronic (M/G) ratio of the investigated SA was determined from CD spectral features, revealing a slightly M-rich composition (M/G ≈ 1.32). Systematic titration of Ca^{2+} (0–4.0 mM) across SA concentrations (1.0–6.0 mg/mL) showed sigmoidal variations in CD ellipticity, enabling identification of transition points associated with nucleation and the onset of the intermediate phase. At SA concentrations ≤ 2.0 mg/mL, the CD spectra reached a plateau after the stoichiometric Ca^{2+}–GG coordination limit, indicating completion of early assembly stage. For instance, at SA = 2.0 mg/mL, sigmoidal curve reached a plateau with a transition point at approximately 2.75 mM Ca^{2+} (**Figure 1a,b**). Transition points obtained at different SA concentrations were then plotted in the phase diagram together with the minimum gelation concentration (MGC) values (**Figure 1c**).

To validate these findings, complementary FTIR-ATR, SAXS, and AFM analyses were performed. FTIR spectra of dried films confirmed Ca^{2+} coordination through splitting and red-shift of the carboxylate band, while SAXS and AFM revealed fibrillar growth and network formation (*data not shown*).

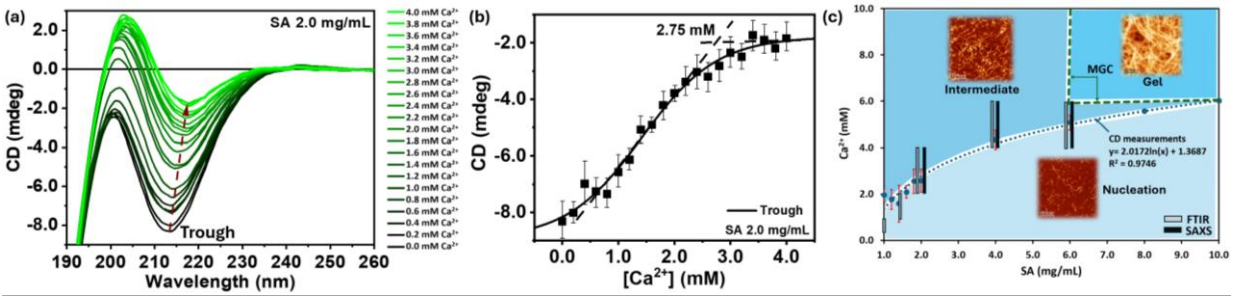

FIGURE 1. (a) CD spectra showing Ca^{2+}-induced assembly of SA (2.0 mg/mL) in the non-gel state; (b) the corresponding ellipticity changes at the trough (λ ≈ 210-215nm) derived from panel (a), highlighting the transition point for 2.0 mg/mL at the plateau region (~2.75 mM Ca^{2+}); and (c) the SA–Ca^{2+} phase diagram derived from CD transition points across various SA and Ca^{2+} concentrations, with SAXS, FTIR, and AFM results overlaid to demonstrate cross-technique consistency.

Transition boundaries obtained from all techniques showed consistent concentration-dependent trends, confirming that CD is highly sensitive to early nucleation events in solution. This multi-technique approach provides a unified phase diagram for the SA–Ca^{2+} system and highlights the capability of SRCD to detect subtle conformational rearrangements during early hydrogel assembly (**Figure 1c**). The results contribute to a deeper understanding of alginate gel formation relevant to biomaterials, drug delivery, and tissue engineering applications.

REFERENCES

1. L. Cao, W. Lu, A. Mata, K. Nishinari and Y. Fang, *Carbohydr. Polym.*, 2020, **242**, 116389.
2. H. Wang, Y. Wan, W. Wang, W. Lia, and Jie Zhu, *Int. J. Food Prop.*, 2018, **21**, 1995-2006.
3. E. R. Morris, D. A. Rees and D. Thom, *Carbohydr. Res.*, 1980, **81**, 305–314.
4. D. Thom, G. T. Grant, E. R. Morris and D. A. Rees, *Carbohydr. Res.*, 1982, **100**, 29–42.
5. S. J. Khouri and V. Buss, *Biophys. Chem.*, 2011, **2**, 380–385.

Separation and Chiroptical Detection of Biomolecules Using an LC-SRCD System: A Case Study on Amino Acid Profiling

Shunsuke Maeda[a], Satoshi Hashimoto[b], Koichi Matsuo[a,b,c], and Mohamed Ibrahim[b]

[a]*Department of Physics, School of Science, Hiroshima University, Higashi-Hiroshima 739-0046, Japan*
[b]*Research Institute for Synchrotron Radiation Science, HiSOR, Hiroshima University, Higashi-Hiroshima 739-0046, Japan*
[c]*Graduate School of Advanced Science and Engineering, Hiroshima University, Higashi-Hiroshima 739-8526, Japan*

Keywords: LC-SRCD, Synchrotron radiation, Chiroptical analysis, Chromatographic separation, Conformational analysis

Circular dichroism (CD) spectroscopy is a powerful tool for analyzing the stereochemical structures of chiral molecules. However, conventional CD instruments are typically limited to the ultraviolet (UV) region (>190 nm). Consequently, acquiring structural information for molecules that have characteristic absorption bands in the vacuum-ultraviolet (VUV) region, such as saccharides and amino acids, remains challenging [1, 2]. In the present study, a high-intensity synchrotron radiation source at the Hiroshima Synchrotron Radiation Center (HiSOR) is utilized to develop an integrated system combining High-Performance Liquid Chromatography (HPLC) with a VUV-CD spectrophotometer [3].

A specialized flow-cell system capable of meeting the requirements of VUV measurements while coupled to an HPLC unit has been installed at BL12. The system's performance was evaluated through real-time separation and analysis of amino acids (*this study*) and sugars (*currently under investigation*).

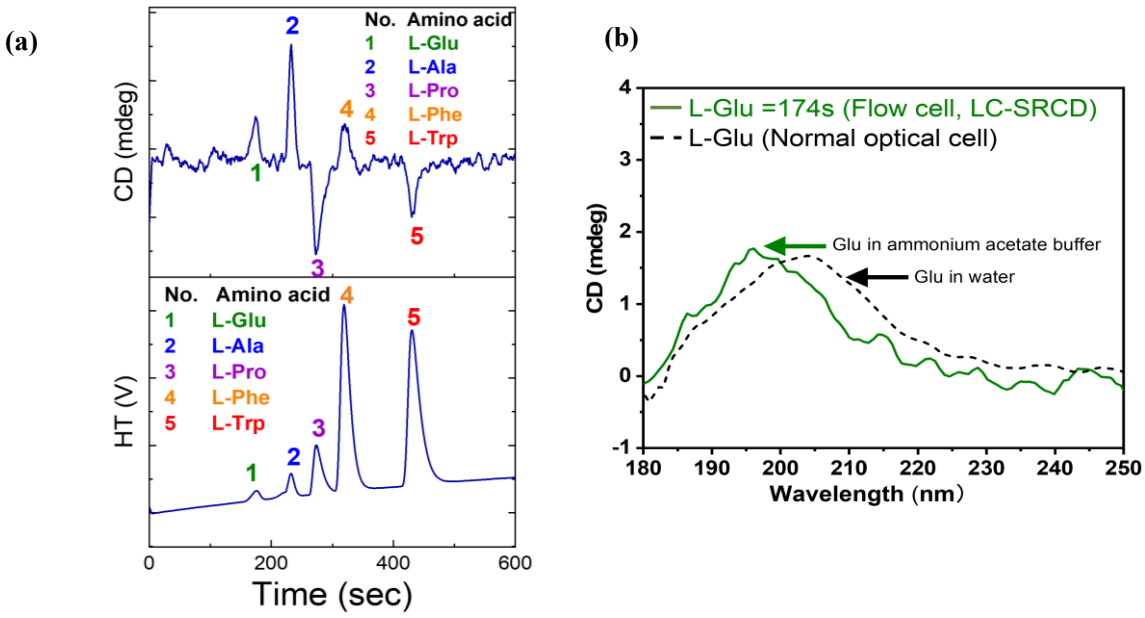

FIGURE 1. LC–SRCD separation and conformational study of an amino acid mixture: (a) online monitoring of the LC separation of five amino acids; and (c) CD spectrum of L-Glu separated by LC and simultaneously monitored by CD, compared with the conventional CD spectrum.

The results demonstrated that the integrated LC–SRCD system successfully separated five amino acids namely L-glutamic acid (L-Glu), L-alanine (L-Ala), L-proline (L-Pro), L-phenylalanine (L-Phe), and L-tryptophan (L-Trp) while simultaneously recording their CD spectra in the VUV region down to ~170 nm (**Figure 1a,b**). This development enables the direct identification and structural analysis of chiral compounds in complex mixtures, offering a novel analytical approach for biochemical and pharmaceutical research. Future work will focus on separating mixtures of sugars, upgrading the LC–SRCD system to be fully automated, and improving the signal-to-noise ratio.

REFERENCES

1. K. Gekko, *Biophys. Physicobiol.*, 2019, **16**, 41–58.
2. K. Matsuo, Y. Matsushima, T. Fukuyama, S. Senba, and K. Gekko, *Chem. Lett.*, 2002, **31**, 826–827.
3. N. Ojima, K. Sakai, K. Matsuo, and K. Gekko, *Chem. Lett.*, 2001, **30**, 522–523.

NEXAFS-Study on Thermal Degradation of PM6:Y6 Organic Solar Cell Active Layers

Y. Hanaki[a], S. Wada[a,b] and T. Sekitani[a,b]

a.Graduate School of Advanced Science and Engineering, Hiroshima University
b.Research Institute for Synchrotrom Radiation Science, Hiroshima University

Keywords: Organic Sokar Cell, NEXAFS

In recent years, environmental and energy issues such as global warming and the depletion of fossil fuel resources have become increasingly serious, leading to growing worldwide interest in renewable energy, including solar power generation. Among various photovoltaic technologies, organic solar cells (OSCs) have attracted considerable attention as next-generation solar cells because of their advantages, such as low cost, light weight, and mechanical flexibility. Currently, the power conversion efficiency of OSCs has improved to around 20%, which is comparable to that of conventional silicon-based inorganic solar cells[1]. However, their long-term stability remains a significant challenge.

Due to the intrinsic properties of organic materials, OSCs are susceptible to degradation caused by various external environmental factors, such as light, heat, oxygen, and moisture, resulting in performance deterioration. In particular, under actual operating conditions, solar cells are exposed to high temperatures due to continuous solar irradiation, making thermal degradation unavoidable. Nevertheless, the effects of thermal stress on the active layer structure and the donor/acceptor interface[2], as well as the underlying degradation mechanisms, have not yet been fully clarified. Therefore, a detailed understanding of the thermal degradation process in OSCs is essential for their practical application.

Previous studies have suggested that thermal degradation mainly originates from changes in the phase-separated structure and crystallinity of the active layer. However, under high-temperature conditions, possible changes in the molecular backbone and functional groups cannot be ruled out. In this study, to clarify the origin of thermal degradation in the widely used PM6:Y6 system, near-edge X-ray absorption fine structure (NEXAFS) measurements were carried out at BL-13 of HiSOR.

In the experiments, solutions of PM6, Y6, and a PM6:Y6 blend were spin-coated onto Au substrates to prepare thin-film samples, and their NEXAFS spectra were measured. The samples were then thermally aged by heating them on a hot plate at 150 ° C for 24 hours. After thermal treatment, NEXAFS spectra were measured again and compared with those obtained before heating to investigate thermally induced degradation. As an example, the C 1s NEXAFS spectra of pristine Y6 and thermally aged Y6 are shown in Figure 1. The spectra reveal differences in polarization dependence before and after thermal treatment, indicating that a change in molecular orientation occurred in Y6.

The results of this study demonstrate that the degree of thermal degradation differs between PM6 and Y6. While PM6 shows no significant change, Y6 exhibits a pronounced change in molecular orientation. This difference is considered to originate from the disparity in glass transition temperatures between PM6 and Y6[3]. Furthermore, in the PM6:Y6 blend film, the possibility of intramolecular twisting in Y6 molecules was suggested[4].

These findings indicate that thermal degradation involves both orientation changes associated with the glass transition temperature and structural changes in the molecular backbone, such as intramolecular twisting. This provides a new perspective on thermal degradation mechanisms, extending beyond the conventional understanding that thermal degradation is primarily governed by physical changes.

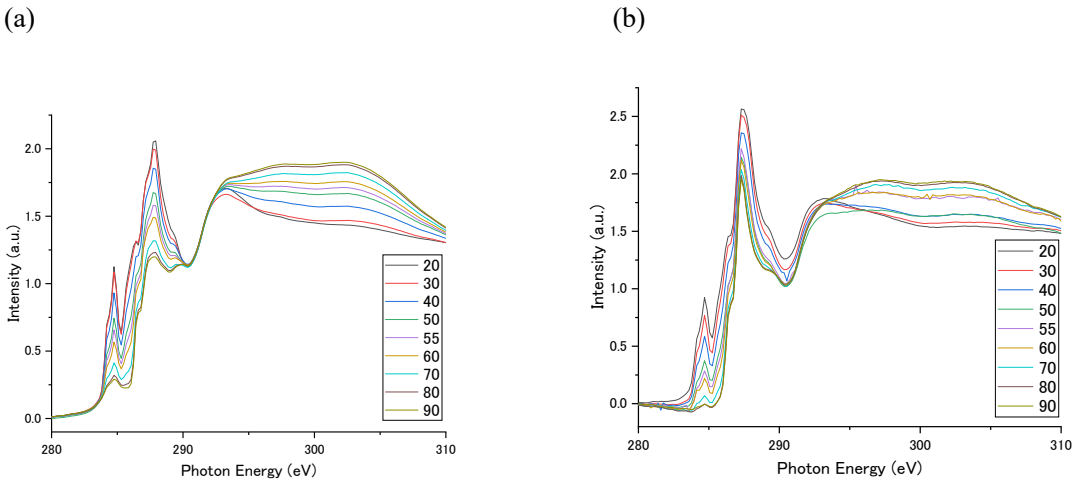

Figure 1. C 1s NEXAFS spectra of (a) pristine Y6 and (b) Y6 after 24 hours of thermal annealing.

REFERENCES

[1] Chen, C. *et al. Nat Commun* **15**, 6865 (2024).

[2] Cheng, P. & Zhan, X. *Chem. Soc. Rev.* **45**, 2544–2582 (2016).

[3] Alam, S. *et al. Adv Funct Materials* **34**, 2308076 (2024).

[4] Pratik, S. M., Kupgan, G., Brédas, J.-L. & Coropceanu, V. *Energy Environ. Sci.* **18**, 841–852 (2025).

Order analysis of supported lipid bilayers on gold substrates by soft X-ray absorption spectroscopy

Yuri Ohura[a], Kakuto Yoshioka[a], Shogo Tendo[b], Hayate Inoue[a], Genki Hashimoto[a], and Shin-ichi Wada[a, c]

[a]*Graduate School of Science and Engineering, Hiroshima University Higashi-Hiroshima 739-8526, Japan*
[b] *National Institute of Technology, Kochi College, Nankoku 783-8508, Japan*
[c]*Research Institute for Synchrotron Radiation Science, Hiroshima University Higashi-Hiroshima 739-0046, Japan*

Keywords: Phospholipids, XAS (X-ray absorption spectroscopy), NEXAFS(near edge X-ray absorption fine structure), Linear polarization

In this study, supported phospholipid bilayers formed on gold substrates were used as model biological membranes, and the molecular orientation and ordering of lipid molecules within the membranes were evaluated at the molecular level using near-edge X-ray absorption fine structure (NEXAFS) spectroscopy and X-ray photoelectron spectroscopy (XPS).

Lipid bilayers are the fundamental structural units of biological membranes and consist of lipid molecules arranged in opposing layers. Their molecular orientation and membrane order are closely related to physical properties such as membrane stability and barrier performance. In highly ordered membranes, hydrocarbon chains are densely packed, resulting in high barrier properties, whereas in less ordered membranes, packing is loose and the membranes exhibit high fluidity. In living systems, membranes with different properties are formed even though they share the same bilayer structure—for example, flexible cell membranes and barrier-function intercellular lipids in the stratum corneum. Accordingly, the dominant lipid species and the number of stacked bilayers vary depending on the biological environment.

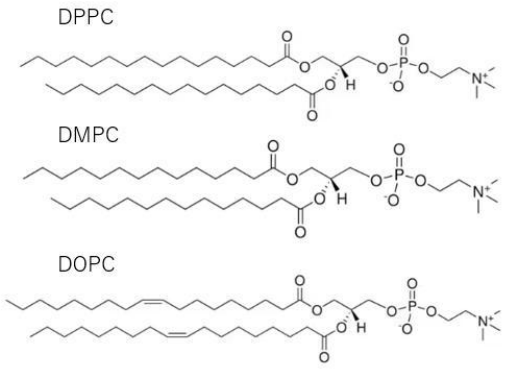

FIGURE 1. Schematic illustration of lipid molecules, DPPC (16:0), DMPC (14:0), and DOPC (18:1). The values in parentheses indicate hydrocarbon chain length and degree of unsaturation.

In this study, a model system of substrate-supported lipid membranes was employed to quantitatively clarify how lipid molecular species and membrane layer number affect membrane structure and order.

DPPC, DMPC, and DOPC phospholipids (Fig. 1), which differ in molecular length and degree of unsaturation, were used as samples, and multilamellar lipid bilayers were prepared on gold substrates by spin coating. Single lipid bilayers were also prepared by hydration treatment of the multilamellar. Film thickness was evaluated by XPS to confirm formation of single bilayers.

NEXAFS measurements were mainly conducted at the carbon K-edge. As shown in Fig. 2, differences in stacking and membrane constituent molecules resulted in different changes in spectral intensity at each X-ray incidence angle. By analyzing this angle dependence and using Rydberg and σ*(C–C) transitions, the tilt angle of the membranes was evaluated. Furthermore, focusing on the difference in orientation between these two transitions, this difference was interpreted as reflecting random components within the hydrocarbon chains, and thus the ordering of hydrocarbon chains in the lipid membranes was assessed.

As a result, in multilayers, DPPC and DMPC containing saturated hydrocarbon chains exhibited high ordering of approximately 80%, whereas DOPC containing unsaturated hydrocarbon chains showed a lower

ordering of about 70%. This is attributed to reduced packing in DOPC membranes due to double bonds. In addition, comparison between single bilayers and multilayers revealed that ordering of hydrocarbon chains decreased by about 10% in single bilayers. The higher ordering observed in multilayers is considered to result from suppression of vertical membrane fluctuations due to stacking. These findings reflect the enhancement of membrane order caused by multilayer formation in biological environments.

This study demonstrates that the effects of lipid molecular unsaturation and membrane layer number (single vs multilayer) on hydrocarbon chain ordering in lipid bilayers can be evaluated using NEXAFS with a consistent metric. The results clarify how factors such as molecular composition and stacking influence membrane order and contribute to understanding biological membrane.

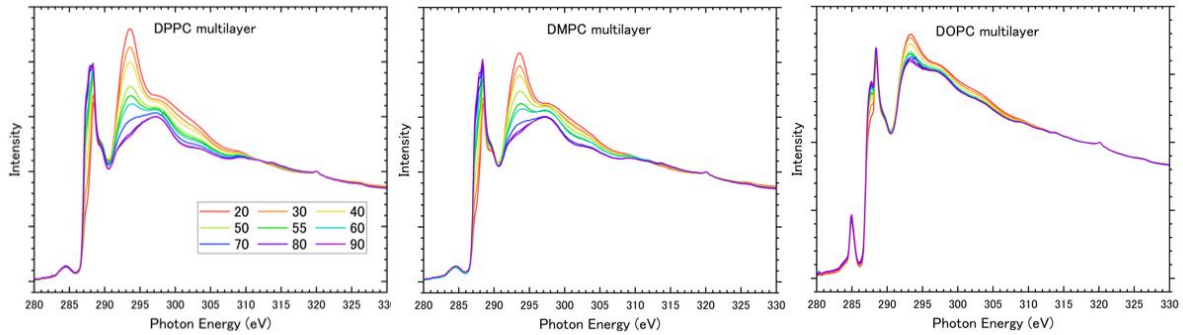

FIGURE 2. NEXAFS spectra measured for DPPC, DMPC, and DOPC multilayers with varying incidence angles from 20° to 90°. Differences in angular dependence are observed.

Position dependence in fluorine-substituted aromatic SAMs studied by X-ray photoemission and Auger electron spectroscopies

Hayate Inoue[a], Yuichiro Kodama[b], Yuri Ohura[a], Kakuto Yoshioka[a], Shogo Tendo[c], Akinobu Niozu[d], Shin-ichi Wada[a,b,e]

[a]*Graduate School of Advanced Science and Engineering, Hiroshima University, Higashi-Hiroshima 739-8526, Japan*
[b]*School of Science, Hiroshima University, Higashi-Hiroshima 739-8526, Japan*
[c]*National Institute of Technology, Kochi College, Nankoku 783-8508, Japan*
[d]*Graduate School of Humanities and Social Sciences, Hiroshima University, Higashi-Hiroshima 739-8524, Japan*
[e]*Research Institute for Synchrotron Radiation Science, Hiroshima University, Higashi-Hiroshima 739-0046, Japan*

Keywords: Self-assembled monolayers (SAMs), X-ray photoemission spectroscopy, Auger electron spectroscopy.

In recent years, the development of organic materials for electronic and optoelectronic devices has attracted significant attention. To realize the industrial application of these materials, optimizing their charge transport properties is crucial. This requires elucidating intramolecular charge transfer dynamics. Consequently, research has focused on various organic molecules, particularly aromatic molecules where electron transfer is facilitated by π-conjugation. In particular, fluorine substitution has been suggested as a potential method for controlling charge transfer properties. For instance, it has been reported that asymmetric fluorine substitution within a molecule can induce diode characteristics.

In our previous study, we quantitatively evaluated charge transfer by tracking the relaxation process following soft X-ray core-level resonant excitation. We adopted self-assembled monolayers (SAMs) as a platform, where the photo-absorbing terminal groups are arranged at the outermost surface. By introducing a methyl ester group at the terminus, we were able to generate excited electrons at the terminal moiety through O 1s resonant excitation, allowing for the efficient observation of intramolecular charge transport processes. Using biphenyl SAMs with different fluorine substitution positions on Au substrates (as shown in Figure 1), we found that the charge transfer time for MFB was approximately 1 fs faster than that for MBF. However, the significance of this difference and the detailed mechanism behind it remain unclear. Therefore, in this study, we investigated the effect of fluorine substitution on the electronic states of the molecules using X-ray Photoemission Spectroscopy (XPS) and Auger Electron Spectroscopy (AES) of the F 1s core level.

Two types of fluorine-substituted SAMs were prepared by immersing gold substrates in 1 mM ethanol solutions of each sample for 24 hours, followed by rinsing with ethanol. Near-edge X-ray absorption fine structure (NEXAFS), X-ray photoemission spectroscopy (XPS), and Auger electron spectroscopy (AES) measurements were performed on the prepared SAMs at HiSOR BL-13. All measurements were conducted at room temperature. NEXAFS measurements were carried out at the carbon and fluorine K-edges in the total electron yield (TEY) mode. The incidence angle of soft X-rays relative to the substrate surface was varied from 20° to 90° in 10° steps for the C K-edge, and set to 20°, 55°, and 90° for the F K-edge. For XPS measurements, the incident photon energy was set to 907 eV. The

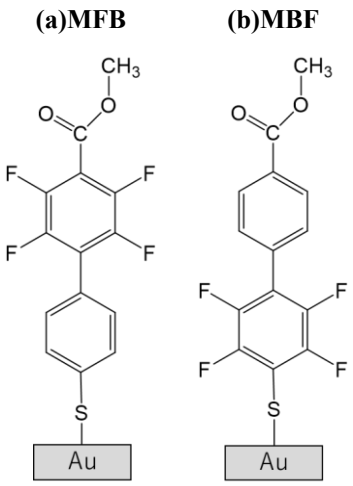

FIGURE 1. Schematic drawings of molecular structures of (a)MFB, and (b)MBF SAMs.

binding energy of the F 1s region was calibrated using the O 1s peak observed in the same spectrum. The reference binding energy of the O 1s peak was determined based on the Au $4f_{7/2}$ peak (84.0 eV) in a separately measured spectrum containing both O 1s and Au 4f peaks. AES measurements were performed at the following three excitation energies: (i) 696 eV, corresponding to the F 1s to π_1^*(C-F) resonant excitation where resonant Auger decay competes with the charge transfer process; (ii) 703 eV, which is sufficiently higher than the ionization potential (IP) to induce normal Auger decay; and (iii) 688 eV in the pre-edge region of the F K-edge to subtract the photoelectron component.

In the C K-edge NEXAFS spectra, π^* peaks were primarily observed in the photon energy region below the ionization potential (IP) (pre-edge region), while σ^* peaks were observed in the region above the IP (post-edge region). The absorption intensity of the π^* peak was maximized at an incidence angle of 90°, whereas that of the σ^* peak was maximized at 20°. These results indicate that both MFB and MBF molecules are oriented upright with respect to the gold substrates.

In the F K-edge region, π_1^*, σ^*, and π_2^* peaks were observed in this order from the lower photon energy side. This suggests that the π-conjugated structure extends to the vicinity of the fluorine atoms.

Next, in the XPS measurements, single-component F 1s peaks were observed at 686.4 eV for MFB and 685.6 eV for MBF, showing a chemical shift of approximately 0.8 eV. This difference in binding energy is attributed to the screening effect from the substrate resulting from the different fluorine substitution positions, as well as differences in the local chemical environment.

Comparing the AES spectra shown in Fig. 2, significant differences in spectral shape were observed in the 650–660 eV region. Specifically, the spectral intensity on the higher kinetic energy side, which corresponds to resonant Auger decay, was relatively lower for MBF compared to MFB. This suggests that the charge transfer process from a F atom is more dominant in MBF, indicating a faster charge transfer time. This result is consistent with the trend reported in previous studies, where the charge transfer time decreases as the excitation site becomes closer to the substrate [1].

This study demonstrates that AES measurements using F 1s excitation, in addition to the conventional O 1s excitation, are useful for evaluating intramolecular charge transfer dynamics. In the future, quantitative evaluation of charge transfer times in fluorine-substituted systems is expected to be achieved by performing Core-hole clock analysis using reference molecular systems where no charge transfer occurs.

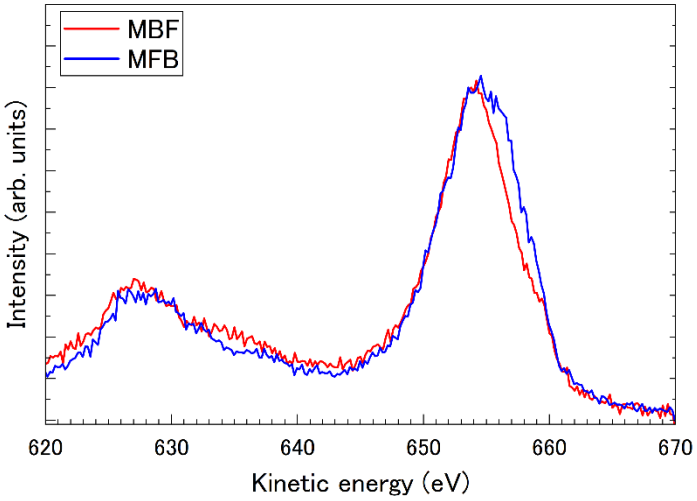

FIGURE 2. AES spectra of MBF (red) and MFB (blue).

REFERENCES

1. S. Tendo *et al*. Phys. Chem. Chem. Phys., **27**, 388 (2025).

Ion Irradiation Induced Frustrated Non-collinear Magnetism in Tetragonally Distorted Cobalt Manganites: Insights from X-ray Magnetic Circular Dichroism

Aradhana Kumari[1], Masahiro Sawada[1], Vijay Raj Singh[2]

[1]*Research Institute for Synchrotron Radiation Science, Hiroshima University, Higashi-hiroshima, Hiroshima, 739-8530, Japan*
[2]*Department of Physics, Central University of South Bihar, Gaya, 824236, Bihar, India*

Keywords: Spinel oxides, Swift heavy ion irradiation, X-ray magnetic circular dichroism

The rapid advancement of multifunctional devices has stimulated considerable interest in materials whose physical properties can be precisely tuned through external perturbations. Among these, spinel oxides represent an exceptional class due to the strong coupling among lattice, charge, spin, and orbital degrees of freedom. Such intricate interactions often give rise to competing ground states, magnetic frustration, and non-collinear spin configurations, making spinel magnetic structure highly sensitive to external stimuli including magnetic fields, chemical substitution, pressure, and irradiation [1-5]. Consequently, they provide an ideal platform for investigating defect-property correlations in strongly correlated systems. In this context, swift heavy ion (SHI) irradiation has emerged as a powerful non-equilibrium approach for tailoring the structural, electronic, and magnetic properties of complex oxides via controlled defect engineering. By carefully tuning irradiation parameters such as ion beam species, energy, and fluence, SHI processing enables access to metastable defect configurations that are difficult to achieve through conventional chemical doping or thermal treatments. In the SHI regime, energy loss occurs predominantly through electronic stopping, producing intense electronic excitation along the ion trajectory. In complex oxides, this process can induce localized lattice modification, defect generation, and cation redistribution, thereby strongly influencing structural and functional characteristics [6-8].

To quantify these effects in tetragonal $CoMn_2O_4$ under 100 MeV ^{107}Ag ion irradiation, comprehensive structural, electronic, and magnetic characterizations were performed using complementary diffraction, magnetometry, and element-selective x-ray spectroscopic techniques, supported by SRIM-TRIM Monte Carlo simulations. The combined influence of SHI irradiation and cumulative fluence leads to a pronounced increase in oxygen-vacancy concentration, accompanied by associated cation vacancies, because electronic stopping dominates nuclear stopping by approximately two orders of magnitude in the beam scattering process in $CoMn_2O_4$ target. Structural analyses reveal that although the $I4_1/amd$ crystal framework is preserved, irradiation introduces substantial lattice strain, local symmetry distortions, and cation redistribution. Magnetic measurements demonstrate defect-driven responses characterized by field-aligned moments and short-range correlations indicative of superparamagnetic-like behavior. X-ray absorption spectroscopy confirms that Mn and Co oxidation states remain largely unchanged, whereas x-ray magnetic circular dichroism reveals modified spin polarization with antiparallel dichroic signatures, evidencing inter-sublattice antiferromagnetic coupling. Concurrently, O K-edge spectra show a redistribution of spectral weight between t_{2g} and e_g-derived states, signifying irradiation-induced tuning of metal-oxygen hybridization. Overall, these results demonstrate that lattice-induced electronic reconstruction and defect-modified exchange pathways govern the magnetic behavior, establishing ion irradiation as a versatile tool for tailoring functional responses in frustrated correlated oxides.

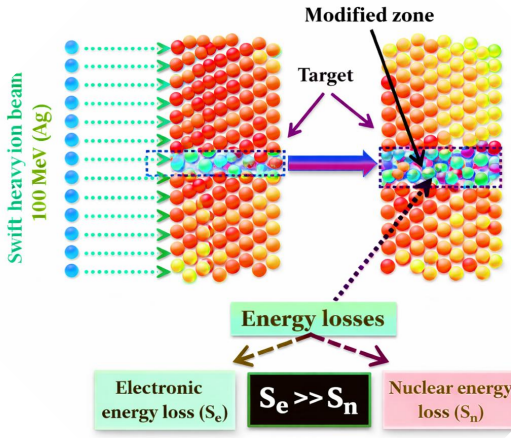

FIGURE 1. The Schematic illustrations of swift heavy ion beam interaction with matter.

REFERENCES

1. S.S. Islam *et al*., "Unconventional superparamagnetic behavior in the modified cubic spinel compound $LiNi_{0.5}Mn_{1.5}O_4$", *Physical Review B*, **102**, 134433 (2020).
2. J. S. Kang *et al*., "Soft x-ray absorption spectroscopy and magnetic circular dichroism study of the valence and spin states in spinel $MnFe_2O_4$", *Physical Review B*, **77**, 035121 (2008).
3. V. K. Verma *et al*., "Orbital magnetic moments in $FeCr_2S_4$ studied by x-ray magnetic circular dichroism", *Physical Review B*, **112**, 104444 (2025).
4. B. Poojitha *et al*., "Spin-phonon coupling in ferrimagnet spinel $CoMn_2O_4$", *Journal of Chemical Physics*, **156**, 184701 (2022).
5. S. Sen *et al*., "Tuning the structural, electronic and magnetic properties of $CoFe_2O_4$ thin films via swift heavy ion irradiation", *Ceramic International*, **52**, 1096-1105 (2026).
6. M. Satalkar *et al*., "Swift heavy ion irradiated spinel ferrite: A cheap radiation resistant material", *Nuclear Instruments and Methods in Physics Research B,* **379***,* 235-241 (2016).
7. J. P. Singh *et al.,* "Raman and Fourier-transform infrared spectroscopic study of nanosized zinc ferrite irradiated with 200 MeV Ag^{15+} beam", *Journal of Alloys and Compounds,* **551**, 370-375 (2013).
8. R. Charak *et al.,* "Mechanistic insights into anisotropy and magnetoresistance control in cobalt ferrite thin films by swift heavy ion irradiation", *AIP Advances*, 16, 025123 (2026).

Tunable Competing Optical Excitation Pathways in the Topological Surface States of Bi_2Te_3

Shin Yokoyama[a, b], Takahito Takeda[a, c], Nagi Suzuki[a], Takuma Iwata[a, b], Ping Zhou[d], Yogendra Kumar[e], Akio Kimura[a, b, f], Koji Miyamoto[e], Taichi Okuda[b, e, f], Mario Novak[g], Uwe Bovensiepen[d], and Kenta Kuroda[a, b, f]

[a]*Graduate School of Advanced Science and Engineering, Hiroshima University, Higashi-Hiroshima, Hiroshima 739-8526, Japan*
[b]*International Institute for Sustainability with Knotted Chiral Meta Matter (WPI-SKCM2), Hiroshima University, Higashi-Hiroshima, Hiroshima 739-8526, Japan*
[c]*Department of Chemical System Engineering, The University of Tokyo, Bunkyo-ku, Tokyo 113-8656, Japan*
[d]*Faculty of Physics and Center for Nanointegration (CENIDE), University of Duisburg-Essen, 47057 Duisburg, Germany*
[e]*Research Institute for Synchrotron Radiation Science (HiSOR), Hiroshima University, 739-0046 Higashi-Hiroshima, Japan*
[f]*Research Institute for Semiconductor Engineering, 1-4-2 Kagamiyama, Higashi-Hiroshima, Hiroshima 739-8527, Japan*
[g]*Department of Physics, Faculty of Science, University of Zagreb, 10000 Zagreb, Croatia*

Keywords: Angle-resolved photoemission spectroscopy, Coherent optical response, Optospintronics, Two-photon photoemission spectroscopy, Topological insulator, Ultrafast phenomenon

Topological insulators (TIs) have topological surface states (TSSs) that exhibit Dirac-cone-like dispersion and helical spin textures in momentum space [1]. The ultrafast optical spin response of such TSSs has attracted considerable attention in optospintronics, which aims at optical control of spin-polarized electrons. While various optical responses of TSSs have been reported, elucidating their ultrafast mechanisms requires an understanding of optical coupling involving unoccupied intermediate states. Pump-probe time- and angle-resolved photoemission spectroscopy (tr-ARPES) has been widely employed to study nonequilibrium population dynamics of TSSs in energy and momentum space [2]. By contrast, owing to its intrinsically coherent multiphoton excitation, angle-resolved two-photon photoemission spectroscopy (2PPE-ARPES) directly probes transient optical coupling via unoccupied intermediate states and the associated dephasing dynamics within an ultrashort pulse. Under resonant conditions, competing excitation pathways can produce characteristic spectral modulations and even transient band renormalization [3]. However, experimental studies of coherent optical phenomena in TSSs have remained limited, with only a few reports so far [4, 5].

In this work, we introduced a femtosecond ultrashort-pulse laser into the spin- and angle-resolved photoemission spectroscopy (Spin-ARPES) system developed at the Hiroshima Synchrotron Radiation Center (HiSOR) [6] and performed 2PPE-ARPES measurements on the TSSs of the topological insulator Bi_2Te_3. Using 2PPE-ARPES, we identify two distinct optical excitation pathways in the TSSs of Bi_2Te_3: an off-resonant transition mediated by virtual states [Fig. 1(a)] and a resonant transition via real unoccupied intermediate states [Fig. 1(b)]. Coherent competition between excitation pathways manifests as an intensity modulation featuring a distinct node at a specific kinetic energy in the 2PPE-ARPES spectra [green arrows in Fig. 1(c)]. Photon-energy-dependent measurements reveal that the spectral feature above the node reflects dispersions of unoccupied intermediate states, while that below the node follows those of the occupied TSS [Fig. 2]. This supports an interpretation in terms of competing resonant and off-resonant excitation pathways. Furthermore, temperature-dependent measurements show that a shift of the chemical potential with increasing temperature modifies the intensity of the resonant channel [Fig. 3(a, b)]. As a result, temperature provides a knob for selective on/off control of the resonant excitation pathway [Fig. 3(d, e)]. These results provide microscopic insight into the optical excitation mechanisms of TSSs and highlight the potential for controlling their optical responses, relevant for future spintronic devices.

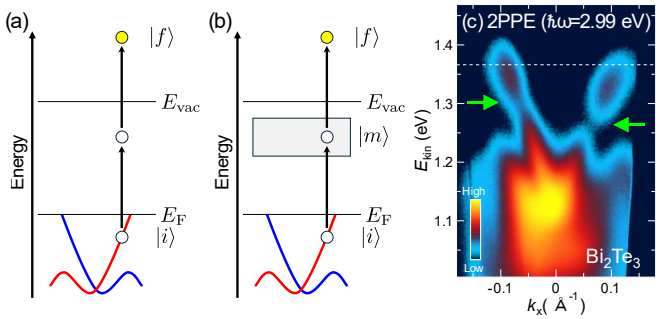

FIGURE 1. (a, b) Schematic illustration of the two competing paths of single-color 2PPE processes: (a) off-resonant transition from the occupied TSS ($|i\rangle$) to the photoelectron final state ($|f\rangle$) via a virtual state, and (b) resonant transition through unoccupied intermediate states ($|m\rangle$). (c) 2PPE-ARPES results at T= 20K. The green arrow marks an intensity node where the 2PPE signal is suppressed.

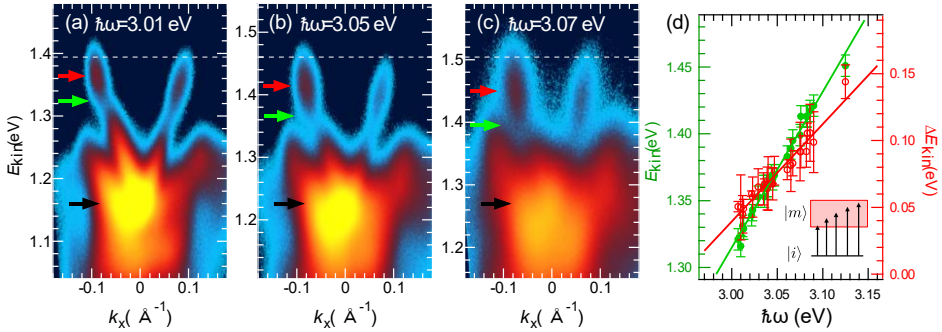

FIGURE 2. (a)-(c) Representative 2PPE-ARPES results acquired at T= 20K with various excitation $\hbar\omega$. The energies at which the intermediate-state bands, the intensity node, and the Dirac point (DP) appear are indicated by red, green, and black arrows, respectively. (d) Plot of the E_{kin} position of the intensity node (green) as a function of $\hbar\omega$, together with the observable energy window of the intermediate-state feature in the 2PPE spectra (red). The solid lines are linear fits to the experimental data, yielding slopes of 1.1±0.1 (green) and 0.7±0.1 (red).

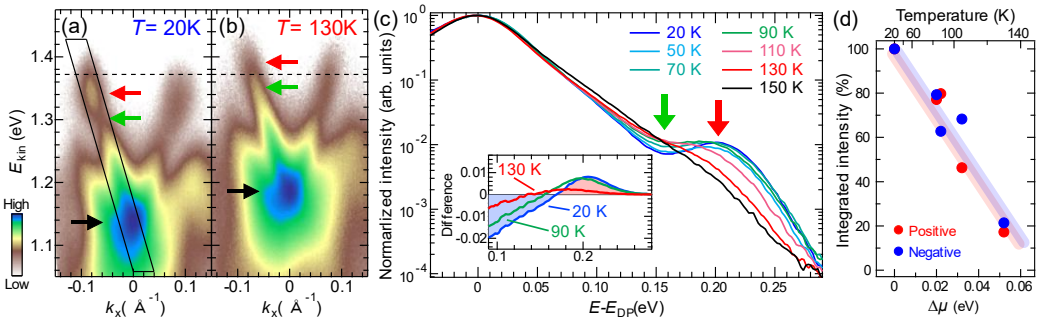

FIGURE 3. (a, b) The representative 2PPE-ARPES results with $\hbar\omega$= 3.00 eV at 20K (a) and 130K (b). The energies at which the intermediate-state bands, the intensity node, and DP appear are indicated by red, green, and black arrows, respectively. (c) The logarithmic plots of the integrated 2PPE signals along the TSS dispersion within the E-k window denoted by the parallelogram in (a). To compensate for the temperature-induced shift of the chemical potential, the horizontal axis is referenced to the DP energy (E-E_{DP}). The red and green arrows indicate the energy positions of the peak and dip intensities. The inset shows the differential intensities with respect to the data at T= 150K where the 2PPE signals of the intermediate state are negligibly small. (d) Normalized area intensities of the positive and negative components extracted from the difference spectra [inset of (c)]. The areas are obtained by integrating both parts and are normalized to their respective values at 20K. The horizontal axis represents the relative shift of the chemical potential with respect to its position at 20K, $\Delta\mu$, estimated from the T-induced shift of E_{DP}. The shaded lines are guides to the eye.

REFERENCES

1. M. Z. Hasan and C. L. Kane, Rev. Mod. Phys. **82**, 3045 (2010).
2. M. Aeschlimann *et al.*, Surf. Sci. **753**, 122631 (2025).
3. M. Reutzel *et al.*, Nat. Commun. **11**, 2230 (2020).
4. K. Kuroda *et al.*, Phys. Rev. Lett. **116**, 076801 (2016).
5. H. Soifer *et al.*, Phys. Rev. Lett. **122**, 167401 (2019).
6. T. Iwata *et al.*, Sci. Rep. **14**, 127 (2024).

Development of Sub-100-fs Time-Resolved Spin-ARPES and Frequency-Domain Analysis of Electronic-Structure Modulation in BiTeBr

Nagi Suzuki[a], Shin Yokoyama[a,b], Ko Sasaki[a,b], Takuma Iwata[a,b], Akio Kimura[a,b,c], Koji Miyamoto[d], Taichi Okuda[b,c,d], Mario Novak[e], and Kenta Kuroda[a,b,c]

[a]*Graduate School of Advanced Science and Engineering, Hiroshima University, Higashi-Hiroshima, Hiroshima 739-8526, Japan*
[b]*International Institute for Sustainability with Knotted Chiral Meta Matter (WPI-SKCM2), Hiroshima University, Higashi-Hiroshima, Hiroshima 739-8526, Japan*
[c]*Research Institute for Semiconductor Engineering, 1-4-2 Kagamiyama, Higashi-Hiroshima, Hiroshima 739-8527, Japan*
[d]*Research Institute for Synchrotron Radiation Science (HiSOR), Hiroshima University, 739-0046 Higashi-Hiroshima, Japan,*
[e]*Department of Physics, Faculty of Science, University of Zagreb, 10000 Zagreb, Croatia*

Keywords: Spin-resolved ARPES, Pump-probe spectroscopy, Electronic structures

The ultrafast control of spin-polarized electronic states using light that leads to modulation of lattice and electronic structures has not yet been firmly established as a distinct strategy in optical spintronics. One promising approach is the photoinduced coherent phonons, which modulate spin-polarized electronic structure by electron-phonon coupling. To establish this route, it is essential to directly capture the ultrafast temporal response of photoinduced electron-phonon coupling and to trace the full temporal evolution of the resulting modulation in spin-polarized electronic states. Here we developed a time- spin- and angle-resolved photoemission spectroscopy (Tr-SARPES) apparatus which achieved temporal resolution sufficient to resolve ultrafast electron-phonon-coupling dynamics (92 fs) by incorporating a femtosecond laser and a pump-probe optical setup into the SARPES instrument at HiSOR [1] and applied it to reveal the ultrafast dynamics of electronic states coupled to coherent phonons excited by femtosecond pulses in the polar semiconductor BiTeBr.

The developed pump-probe optical layout is shown in Figure 1. The setup comprises a laser source and two optical paths: one for the pump and one for the probe. As a laser source, we implemented a regenerative amplifier, delivering 1030-nm pulses with a pulse duration of 190 fs and an average power of 40 W at 100 kHz repetition rate. For Tr-SARPES measurements, 30 W is used, which is carried into an optical parametric amplifier (OPA). This OPA provides tunable pulses covering from 650 to 2500 nm. In this work, we used the signals from OPA at 840 nm with temporal width of 45 fs. A beam splitter splits the IR-beam into pump and probe optical paths. In the probe optical path, ultraviolet probe pulses were generated by second-harmonic generation and subsequent fourth-harmonic generation (FHG) in BBO crystals. After FHG, dispersion was compensated with a prism-pair compressor to optimize probe pulse duration. In the pump optical path, the pump beam was sent through an optical delay stage to control the pump-probe delay time. Finally, the pump and probe beams were recombined using a dichroic mirror to form a collinear beam path and were focused onto the sample inside the ultrahigh-vacuum chamber.

We evaluated the temporal resolution of the Tr-SARPES system using the topological insulator Bi_2Te_3. In the ground state [Fig. 2(a)], no photoemission intensity was observed above the Fermi level (E_F). With pump and probe [Fig. 2(b)], intensity appeared above E_F, originating from unoccupied bulk bands, confirming successful detection of the excited-state electronic structure. We then estimated the instrument response by minimizing material-dependent contributions such as carrier relaxation dynamics. Specifically,

to reduce the influence of relaxation, we analyzed unoccupied states well above E_F [Fig. 2(c)]. By fitting the energy-window-integrated transient intensity, we obtained the pump-probe cross-correlation modeled as a Gaussian [Fig. 2(d, e)] and define the temporal resolution as the FWHM of the fitted Gaussian, yielding 92 fs.

Finally, using this apparatus we tracked the ultrafast dynamics of Rashba-split electronic states in the Rashba-type polar semiconductor BiTeBr and observed pronounced oscillations in the time-dependent photoemission intensity after photoexcitation, attributable to photoinduced coherent phonons.

The development of this apparatus thus unlocks sub-100-fs, time-resolved access to the interplay between lattice motion and spin-polarized electronic structure.

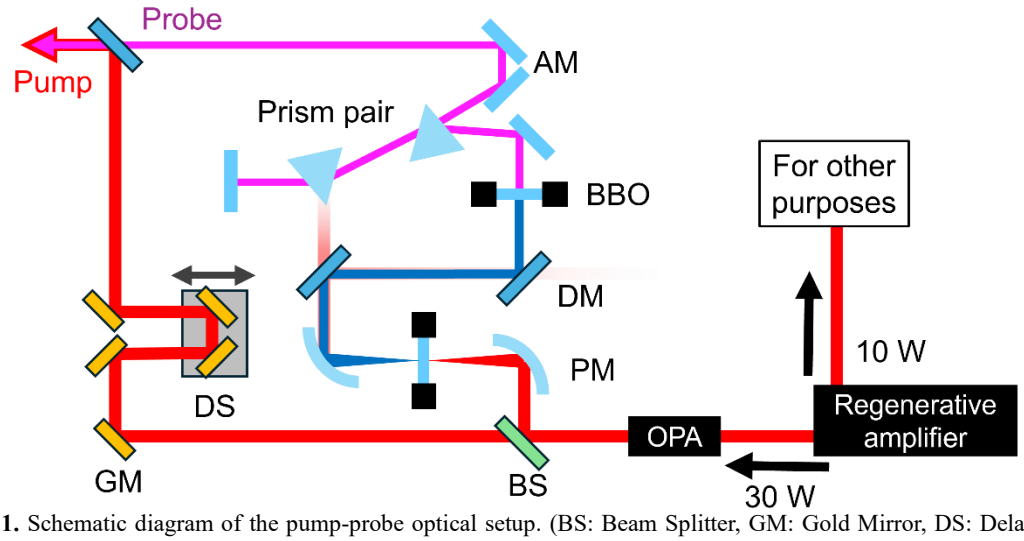

FIGURE 1. Schematic diagram of the pump-probe optical setup. (BS: Beam Splitter, GM: Gold Mirror, DS: Delay Stage, PM: Parabolic Mirror, DM: Dichroic Mirror, AM: Aluminum Mirror)

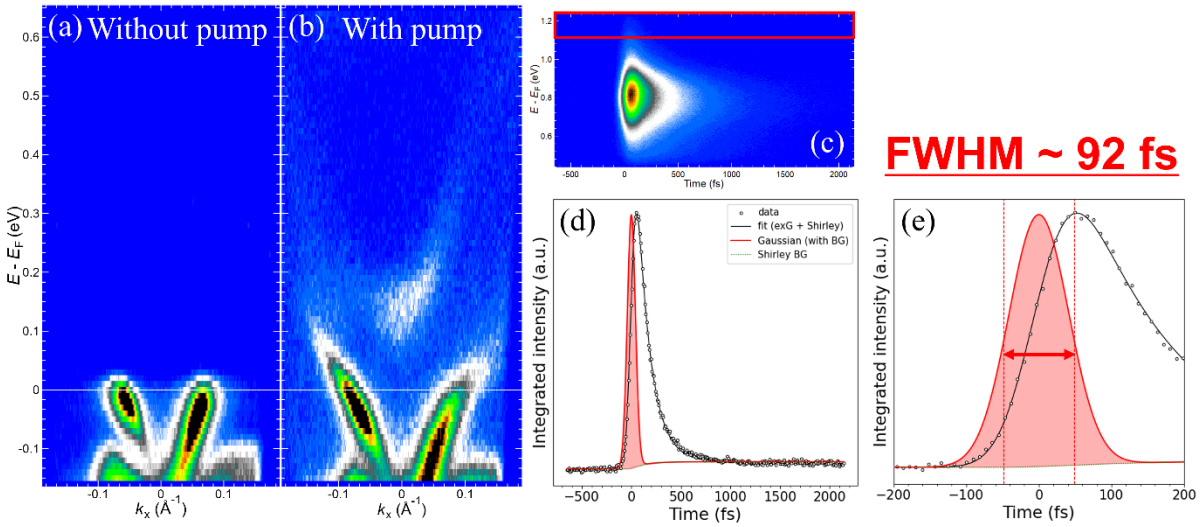

FIGURE 2. (a) ARPES image of Bi_2Te_3 in the ground state observed with the probe beam only. (b) ARPES image of Bi_2Te_3 in the excited state observed with both the pump and probe beams. The measurements were performed at 30 K with a 5.9 eV probe, a 1.48 eV pump, and a pump fluence of 2.9 mJ/cm². (c) Angle-integrated photoemission intensity in the unoccupied band located around 1 eV above the Fermi energy. (d) Observable obtained by integrating the region enclosed by the rectangle in (c), together with its fitting. The fitting function is given by the convolution of a Gaussian representing the input signal of the laser pulse and a response function reflecting the electron lifetime, $f(t) = \Delta I_0 e^{-(t-t_0)/\tau}\Theta(t-t_0)$. The Gaussian determined from the fitted parameters is shown as the red curve. (e) Magnified view of (d).

REFERENCES

1. T. Iwata *et al.*, Sci. Rep. **14**, 127 (2024).

Present Status of Multi-Channel Spin Detector Development

Kazuki Sumida[a], Yuita Fujisawa[a], Koji Miyamoto[a], and Taichi Okuda[a,b,c]

[a]*Research Institute for Synchrotron Radiation Science (HiSOR), Hiroshima University, 2-313 Kagamiyama, Higashi-Hiroshima, Hiroshima 739-0046, Japan*
[b]*International Institute for Sustainability with Knotted Chiral Meta Matter (WPI-SKCM^2), 1-3-1 Kagamiyama, Higashi-Hiroshima, Hiroshima 739-8511, Japan*
[c]*Research Institute for Semiconductor Engineering (RISE), Hiroshima University, 1-4-2 Kagamiyama, Higashi-Hiroshima, Hiroshima 739-8527, Japan*

Keywords: Spin- and angle-resolved photoemission spectroscopy, VLEED spin detector.

Spin- and angle-resolved photoemission spectroscopy (SARPES) is an indispensable technique for investigating the spin-dependent electronic structure of materials, providing direct access to the energy, momentum, and spin of electrons [1]. Since the discovery of Rashba systems and topological materials, the demand for high-efficiency SARPES has steadily increased in condensed matter physics. In particular, very-low-energy-electron-diffraction (VLEED) based spin detectors, which offer approximately two orders of magnitude higher efficiency than conventional Mott-type spin detectors, have become widely implemented [2,3,4].

Recent efforts have extended VLEED-based SARPES toward time-resolved and spatially-resolved measurements [5,6,7]. However, in time-resolved SARPES using two-photon photoemission processes or in nano-scale spatially-resolved SARPES with focused beams, the photoelectron intensity is significantly reduced compared to conventional ARPES. As a result, spin-resolved band structure mapping measurements with single-channel VLEED detectors require prohibitively long acquisition times.

To overcome this limitation, we are developing a reflection-type multi-channel spin detector based on a VLEED scheme at HiSOR. The system consists of a hemispherical electron analyzer followed by a custom-designed spin lens. Photoelectrons preserving the two-dimensional energy-momentum (E_k-θ) distribution are incident on an oxygen-terminated Fe thin-film target, and the reflected electron image is amplified by a microchannel plate and recorded with a CCD camera. This design enables simultaneous spin detection over multiple momentum channels, potentially improving the overall efficiency by more than three orders of magnitude compared to conventional single-channel VLEED detectors.

The spin lens assembly, high-precision power supply system, and control software have been completed, and trajectory optimization of photoelectrons is currently in progress.

REFERENCES

1. T. Okuda, *J. Phys.: Condens. Matter* **29**, 483001 (2017).
2. T. Okuda *et al*., *Rev. Sci. Instrum.* **82**, 103302 (2011).
3. T. Okuda *et al*., *J. Electron Spectrosc. Relat. Phenom.* **201**, 23 (2015).
4. K. Yaji *et al*., *Rev. Sci. Instrum.* **87**, 053111 (2016).
5. R. Z. Xu *et al*., *Rev. Sci. Instrum.* **94**, 023903 (2023).
6. K. Kawaguchi *et al*., *Rev. Sci. Instrum.* **94**, 083902 (2023).
7. T. Iwata *et al*., *Sci. Rep.* **14**, 127 (2024).

Observation of Antiferromagnetic Domains in the "Devil's Staircase" of CeSb using Polarizing Microscopy

K. Sasaki[a, b], T. Takeda[a], K. Watanabe[a], T. Iwata[a, b], A. Kimura[a, b, c], H. S. Suzuki[d], K. Kuroda[a, b, c]

[a] *Graduate School of Advanced Science and Engineering, Hiroshima University, Higashi-Hiroshima 739-8526, Japan*
[b] *International Institute for Sustainability with Knotted Chiral Meta Matter (WPI-SKCM^2), Higashi-Hiroshima 739-8526, Japan*
[c] *Research Institute for Semiconductor Engineering, Higashi-Hiroshima 739-8527, Japan*
[d] *Institute for Solid State Physics, The University of Tokyo, Kashiwa, Chiba 277-8581, Japan*

Keywords: Electronic nematicity, Antiferromagnetic domain, Devil's staircase

Antiferromagnets have long been regarded as difficult to translate into applications because they exhibit no macroscopic magnetization, which makes control by external fields difficult. In recent years, however, the emergence of spintronic functionalities such as magnetic memory effects and current induced magnetic switching has been increasingly reported as a consequence of underlying symmetry breaking associated with antiferromagnetic order. The origins of these phenomena are suggested to involve topological properties and electronic nematicity. In particular, in antiferromagnets, the emergence of electronic nematicity concomitant with antiferromagnetic order causes the electronic system to spontaneously break rotational symmetry and select a preferred direction, resulting in pronounced anisotropy in electronic responses such as charge transport and optical properties. Because external stimuli that impose directional symmetry breaking such as strain, electric fields, and electric currents can couple to the nematic order parameter arising from the antiferromagnetic order and select its orientation, switching controlled by various external fields is expected.

In the antiferromagnet CeSb, which is known to exhibit complex magnetic structure transitions called the devil's staircase and to host more than 14 distinct magnetic structures depending on temperature and magnetic field [1], anisotropy emerges in the 4*f* electron ground state accompanying the phase transitions. This is reported to be accompanied by a large lattice strain reaching about 0.1 % [2] and a reconstruction of the anisotropic electronic band structure [3], suggesting a correlated electronic state with strong coupling among orbital, spin, and lattice degrees of freedom. In contrast, there have been no experimental reports that directly capture domain evolution during the transitions or domain control by external fields.

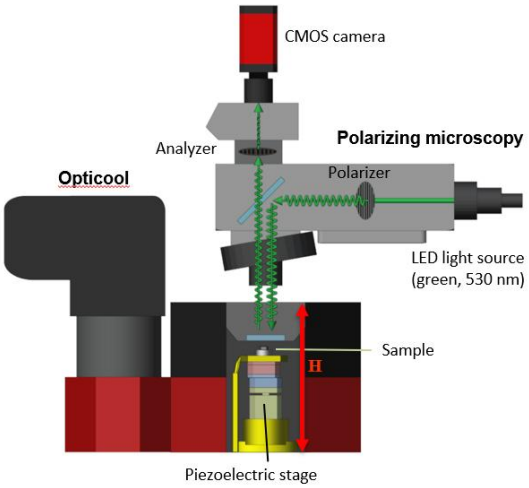

Fig. 1 : experimental setup

In this study, we used a polarization microscope equipped with an LED light source and a cryostat capable of reaching 1.7 K, installed in the HiSOR preparation building, and observed the temperature and magnetic field dependences of the domain structure by using birefringence originating from antiferromagnetic order (Fig. 1).

As a result, below the Néel temperature, we observed three types of magnetic domains reflecting the direction of the magnetic moments. Two are in plane domains shown in red and blue, and one is an out of plane domain shown in white (Fig. 2). Near the transition temperatures reported in previous studies, we confirmed prominent changes in both domain configuration and birefringence intensity. Furthermore, under applied magnetic fields, we observed a process in which domains evolve toward a single domain state near the transition fields. These results visualize domain dynamics associated with the devil's staircase in CeSb and indicate that the development of anisotropy in the electronic state plays a key role.

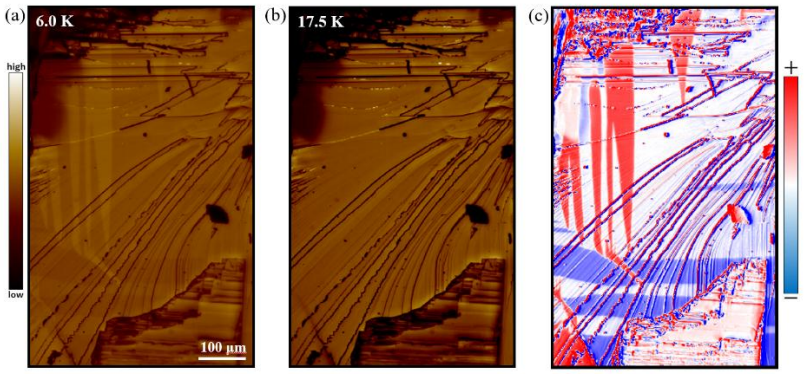

Fig. 2 : Polarized optical microscopy images of the cleaved CeSb (001) surface. (a) Antiferromagnetic phase at $T = 6.0$ K, (b) Paramagnetic phase at $T = 17.5$ K, and (c) difference image between (a) and (b).

REFERENCES

1. J. Rossat-Mignot *et al*., J. Magn. Magn. Mater. **52**, 111 (1985).
2. F. Hulliger *et al.*, J. Low. Temp. Phys. **20**, 269 (1975).
3. K. Kuroda *et al.*, Nature Commun. **11**, 2888 (2020).

Parity-Violating Antiferromagnetic Order Leading to Asymmetric Electronic Band Structure in LaMnSi

T. Iwata[A], K. Shiraishi[A] , T. Aoyama[A], D. Senba[A], T. Takeda[A, C], Y. Fujisawa[D], M. Nurmamat[A] , K. Nakanishi[A], K. Yamagami[E] , Y. Yanagi[F], T. Yamada[F], A. Kimura[A,B,G, H], H. Tanida[F], and K. Kuroda[A,B,H]

[A] *Graduate School of Advanced Science and Engineering, Hiroshima University, 1-3-1 Kagamiyama, Higashi-Hiroshima 739-8526, Japan*
[B] *International Institute for Sustainability with Knotted Chiral Meta Matter (WPI-SKCM²), Hiroshima University, 2-313 kagamiyama, Higashi-Hiroshima, 739-0046, Japan*
[C] *Department of Electrical Engineering and Information Systems, The University of Tokyo, 7-3-1 Hongo, Bunkyo-ku, Tokyo 113-8656, Japan*
[D] *Research Institute for Synchrotron Radiation Science, Hiroshima University, 2-313 Kagamiyama, Higashi-Hiroshima 739-0046, Japan*
[E] *Japan Synchrotron Radiation Research Institute (JASRI), Sayo, Hyogo 679-5198, Japan*
[F] *Liberal Arts and Sciences, Toyama Prefectural University, 5180 Kurokawa, Imizu, Toyama 939-0398, Japan*
[G] *Synchrotron Radiation Research Center, National Institutes for Quantum Science and Technology (QST), 1-1-1 Kouto, Sayo-cho, Sayo-gun, Hyogo 679-5148, Japan*
[H] *Research Institute for Semiconductor Engineering (RISE), Hiroshima University, 1-4-2 Kagamiyama, Higashi-Hiroshima 739-8527, Japan*

Keywords: Electronic structure, Angle-resolved photoemission spectroscopy, Antiferromagnetic spintronics

Spontaneous symmetry breaking modulates electronic states and serves as the microscopic origin of functional properties. For example, spin-split bands in systems with broken time reversal (*T*) or spatial inversion (*P*) symmetry provide a mechanism to manipulate spin degrees of freedom (Fig.1 **a**, **b**). Extending this concept to antiferromagnets, the interplay between crystal and magnetic structures induces specific symmetry breakings [1]. This allows for the emergence of functional properties that can be manipulated via antiferromagnetic order, offering a unique platform for next-generation spintronics [2].

Among these systems, antiferromagnets that preserve combined parity-time (*PT*) symmetry while breaking both *P* and *T* symmetries are attracting particular attention [3]. In these materials, the specific symmetry breaking induces momentum-space asymmetric band structures while retaining spin degeneracy (Fig.1 **c**). Crucially, this electronic modulation permits the emergence of time-non-invariant nonlinear susceptibilities. These susceptibilities are the origin of exotic phenomena such as non-reciprocal transport and nonlinear optical effects. Unlike systems where inversion symmetry is broken merely by the crystal structure, the magnetic symmetry breaking here is intrinsically coupled to the antiferromagnetic order, offering superior controllability of these functional properties through magnetic domain manipulation.

LaMnSi serves as an ideal candidate to realize such a state [4]. It crystallizes in the non-symmorphic space group *P4/nmm*, where two Mn sublattices are related by the *P* operation [red and blue tetrahedron in Fig.2 **a**]. Below the Néel temperature $T_N = 293$ K, the Mn moments form a collinear antiferromagnetic order along the *c*-axis. In this magnetic structure, *P* symmetry is broken because the inversion operation exchanges the sublattices while leaving the axial spin vectors invariant. Nevertheless, the combined *PT*-symmetry is preserved, as the original configuration is recovered by a subsequent *T* operation (Fig.2 **b**). Consequently, LaMnSi is established as a parity-violating antiferromagnet, providing fertile ground to investigate the functional properties driven by the magnetic symmetry breaking.

In this study, we investigated the electronic structure and symmetry breaking in LaMnSi. We performed soft X-ray angle-resolved photoemission spectroscopy (SX-ARPES) at SPring-8 BL25SU [5]. The observed three-dimensional electronic structures showed good agreement with density-functional theory calculations for the antiferromagnetic phase (Fig.2 **d**, **e**). Crucially, this result demonstrates that Mn 3d electrons play a dual role, governing both the magnetic ordering and the itinerant electrical conduction.

Furthermore, we performed optical second-harmonic generation (SHG) measurements to probe the parity-violating antiferromagnetic order. We resolved the time-noninvariant nonlinear optical susceptibility components and tracked their temperature dependence by employing polarization-dependent SHG. This analysis clarified the behavior of susceptibility components specifically derived from the parity-violating antiferromagnetic order. Moreover, scanning SHG microscopy visualized antiferromagnetic domains on the scale of several hundred micrometers. These results establish LaMnSi as a promising platform for exploring functional properties driven by the parity-violating antiferromagnetic order.

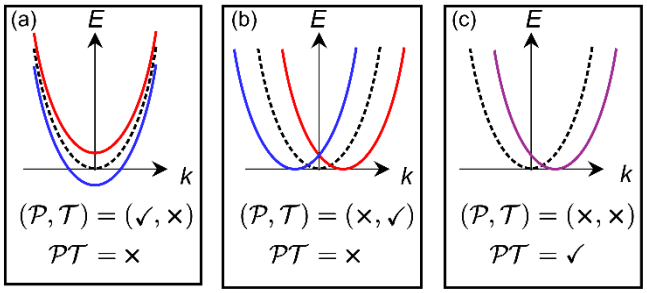

FIGURE 1. Relationship between band structure, symmetry breaking, and nonlinear optical response. (**a**) the symmetric spin splitting, (**b**) the asymmetric spin splitting, and (**c**) the asymmetric band with spin-degeneracy. Red/blue and purple lines denote spin-split and spin-degenerate states, respectively, while dashed curves indicate reference bands with both P and T preserved. The presence (✓) or absence (×) of symmetries are listed at the bottom of each panel.

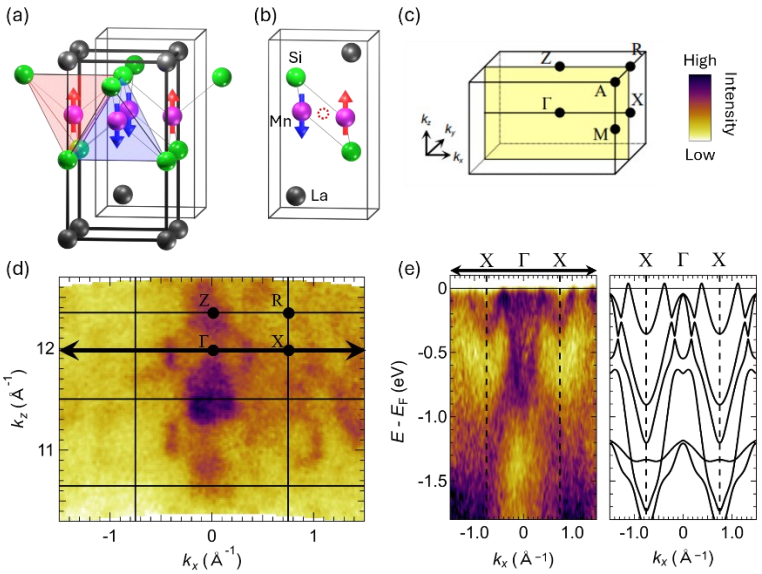

FIGURE 2. Magnetic and electronic structures of LaMnSi. (**a**) Magnetic structure of LaMnSi. Mn moments form a $q = 0$ antiferromagnet with moments aligned along [001] (*c* axis), as indicated by red and blue arrows. Thick lines denote the primitive unit cell. (**b**) The structure is redrawn using the alternative unit cell [thin line in **a**], where the dotted circle highlights the crystallographic inversion symmetry broken by the antiferromagnetic order. (**c**) Brillouin zone with high-symmetry points (**d**) Fermi surface map on the momentum plane denoted by the yellow plane in **c**, which is obtained by varying hu from 400 to 600 eV in steps of 2 eV. (**e**) Left: ARPES image along with Γ -X line indicated the solid arrow in (d). Right: calculated band structures along with Γ -X line for the antiferromagnetic phase.

REFERENCES

1. S. Hayami et. al., J. Phys. Soc. Jpn. **88**, 123702 (2019).
2. T. Jungwirth *et. al*., Nature Nanotechnology **11**, 231-241 (2016).
3. H, Watanabe *et. al*., Phys. Rev. B **96**, 064432 (2017).
4. H. Tanida *et. al*., J. Phys. Soc. Jpn. **91**, 013704 (2022).
5. T. Muro *et. al*., J. Synchrotron Radiat. **28**, 1631-1638 (2021)

Imaging of orbital angular momentum textures in Weyl semimetal using soft x-ray ARPES

D. Senba[a], T. Iwata[a,b], K. Ideura[a], N. Suzuki[a], T. Kai[a], T. Takeda[c], K. Yamagami[d], A. Kimura[a,b,e], M. Novak[f], K. Kuroda[a,b,e]

[a] *Graduate School of Advanced Science and Engineering, Hiroshima University, Higashi-Hiroshima 739-8526, Japan*
[b] *International Institute for Sustainability with Knotted Chiral Meta Matter (WPI-SKCM2), Higashi-Hiroshima 739-8526, Japan*
[c] *Department of Electrical Engineering and Information Systems, The University of Tokyo, 7-3-1 Hongo, Bunkyo-ku, Tokyo 113-8656, Japan*
[d] *Japan Synchrotron Radiation Research Institute (JASRI), Sayo, Hyogo, 679-5198 Japan*
[e] *Research Institute for Semiconductor Engineering, Higashi-Hiroshima 739-8527, Japan*
[f] *Department of Physics, Faculty of Science, University of Zagreb, 10000 Zagreb, Croatia*

Keywords: Soft X-ray, Circular Dichroism, Orbital Angular Momentum

Weyl semimetal, which is a type of topological semimetal, is a material whose electronic band structure features point-like crossings between the conduction and valence spin-split bands. In the vicinity of the crossing point, called Weyl point, electrons behave as massless Weyl fermions, and each Weyl point possesses a definite chirality. Weyl points necessarily appear in pairs with opposite chirality and act as monopoles and antimonopoles of Berry curvature in momentum space.

In Weyl semimetals, Berry curvature is strongly enhanced near the Weyl points, which serves as the origin of various transport and optical phenomena, such as the anomalous Hall effect, negative magnetoresistance arising from the chiral anomaly, and nonlinear optical responses. Therefore, elucidating the distribution of underlying Berry curvature both experimentally and theoretically is of great importance. As a probe of Berry curvatures and its geometries, orbital angular momentum (OAM) texture in momentum space has attracted attention. The OAM texture refers to the momentum-space distribution of the orbital angular momentum of electron wavefunctions, which is closely related to the spin texture and Berry curvature in the presence of spin–orbit coupling. Circular dichroism angle-resolved photoemission spectroscopy (CD-ARPES) enables access to momentum-dependent OAM texture information through the difference in ARPES intensity between left- and right-circularly polarized light.

In this study, we employed bulk-sensitive soft X-ray CD-ARPES -(SX-CD-ARPES) to investigate the prototypical Weyl semimetal TaAs at BL25SU of SPring-8 - [1]. Since Weyl points are formed by crossings of bulk valence and conduction bands, using bulk-sensitive soft X-ray is key for their direct observations. In TaAs, two Weyl points, namely W1 and W2 points exist at k_z values corresponding to photon energies $\hbar\omega$ of 590 eV and 618 eV, respectively. By tuning soft X-ray photons from synchrotron, a clear $\hbar\omega$ dependence was observed in [Fig. 1(a)], reflecting signatures of the three-dimensional bulk dispersions. From this kz band mapping, we disentangled the W1 Weyl points from the three-dimensional band dispersions, and focused on this point with $\hbar\omega$ of 590 eV.

Figure 1(b) represents the Fermi surface mapping on the k_x-k_y at k_z = 12.9 Å^{-1} [line in Fig. 1(a)], taken with circularly polarized x-ray photons. The red and blue dots indicate the positions of the Weyl points, located at (k_x, k_y) = (0.47, ±0.06) and (−0.47, ±0.06) [2], respectively. In this data, the presence of the significant circular dichroism is already seen as an asymmetric intensity along k_y axis.

The SX-CD-ARPES imaging E–k_x cuts at k_y = 0.06 Å^{-1} are shown in Figs 1(c) and (d). The dots in each panel indicate the locations of the Weyl points. Clearly, the sign of the CD signal reverses across the Weyl

point. The CD signal primarily reflects the x-component of OAM according to our experimental geometry. Let us note that the overall CD sign observed in Fig. 1(c) and (d) is reversed.

These results experimentally demonstrate that a pair of Weyl points with opposite topological charges exists, respectively.

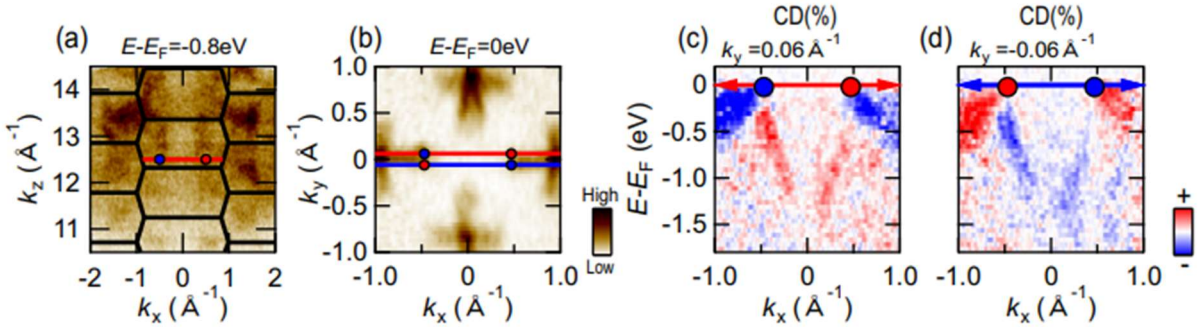

FIGURE 1. (a) k_z mapping of TaAs at $E - E_F = -0.8$ eV. The black line represents the Brillouin zone along the k_z direction. The red and blue dots in the figure indicate the positions of the Weyl points. The red line represents the k_z position (k_z = 12.9) that is accessible with the photon energy of 590 eV used in this experiment. (b) Equal-energy surface map acquired using left circularly polarized light at a photon energy of hν = 590 eV. The red and blue dots in the figure indicate the positions of the Weyl points, which are located at (k_x, k_y) = (0.47, ±0.06) and (−0.47, ±0.06). The red and blue lines represent cuts along k_y = ±0.06, respectively, and intersect the Weyl points. The Weyl points located in the positive and negative k_y regions form a pair. (c)(d) Cut along the red line in (b) at k_y = 0.06 Å^{-1}(c) and k_y = -0.06 Å^{-1}(d). The CD signal reflects the x-component of the orbital angular momentum (OAM), where the red regions indicate positive OAM and the blue regions indicate negative OAM. The blue and red dots in the figure represent the positions of the Weyl points: in panel (c), they are located at (k_x, k_y) = (±0.47, 0.06), while in panel (d), they are located at (k_x, k_y) = (±0.47, −0.06). These correspond to the source and sink monopoles, respectively.

REFERENCES

1. T. Muro *et al*., *J. Synchrotron Rad*. (2021). **28**, 1631-1638
2. B. Q. Lv, N. Xu *et al., Nature Physics.* **11**, 724–727 (2015).

Theoretical Study on Decay Processes Following Core Excitation

Yuika Watari[a] and Osamu Takahashi[b]

[a]*Graduate School of Advanced Science and Engineering, Hiroshima University.*
[b]*Research Institute for Synchrotron Radiation Science, Hiroshima University.*

Keywords: X-ray emission spectroscopy (XES), Density functional theory, Koopmans' theorem, Ionization potential, Auger electron spectroscopy (AES).

This study focused on spectroscopic techniques that incorporate decay processes following inner-shell excitation, which have evolved into methods for analyzing electronic and molecular structures. We improved the theoretical calculation methods for X-ray emission spectroscopy (XES) and Auger electron spectroscopy (AES). Inner-shell hole states have lifetimes of several femtoseconds, and nuclear dynamics during this brief period significantly influence the spectral shape, particularly in molecules containing light elements. Therefore, establishing highly accurate and efficient theoretical methods is essential for the precise interpretation of experimental spectra in general.

For XES theoretical calculations, we propose an improved method based on Slater transition state theory (STS) used to evaluate ionization potentials (IP) [1]. Instead of removing 1/2 electrons from each orbital, as is conventionally done, electrons are uniformly removed from the entire valence electron orbital. This method reduces the number of required SCF calculations from multiple (based on the number of valence electron orbitals) to one. When applied to water molecules, it reproduces experimental peak positions with higher accuracy than the Koopmans' theorem. Furthermore, incorporating the molecular dynamics (MD) of the inner-shell hole state brings the peak intensities closer to the experimental values.

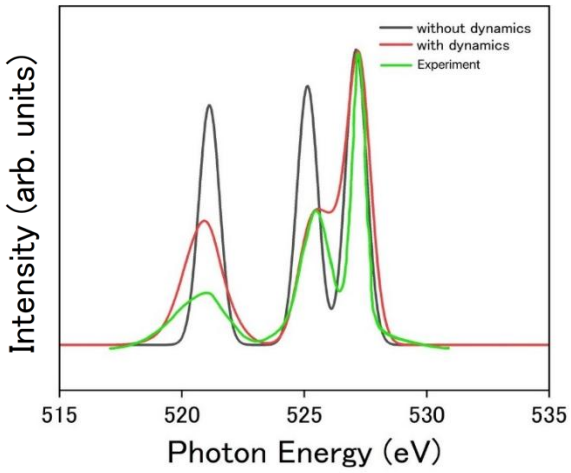

FIGURE 1. XES theoretical spectrum of one molecule of H_2O [2].

Next, for the AES theoretical calculations, we introduced the semiclassical Kramers-Heisenberg (SCKH) equation, which treats inner-shell excitation and Auger decay as a single scattering process, replacing the previously dominant two-step model. This allows the direct incorporation of correlations between the two processes, establishing a framework in which the energy-time evolution from MD is naturally reflected in the spectral width via Fourier transformation. Considering the computational cost and accuracy, the CI method was adopted for the electronic state calculations.

For single water molecule, 20 fs MD simulations of the inner-shell hole state were performed to investigate the required number of velocity and initial structure samples. The results showed that the spectrum converged with approximately 20 velocity samples, while maximizing the number of initial structure samples was crucial. The AES spectrum calculated under the final conditions of 20 velocity samples and 50 initial structure samples successfully reproduced the experimental peak positions. However, an overestimation of the peak intensity originating from the bound orbitals was observed, indicating that expanding the initial structure sampling remains a challenge for future studies.

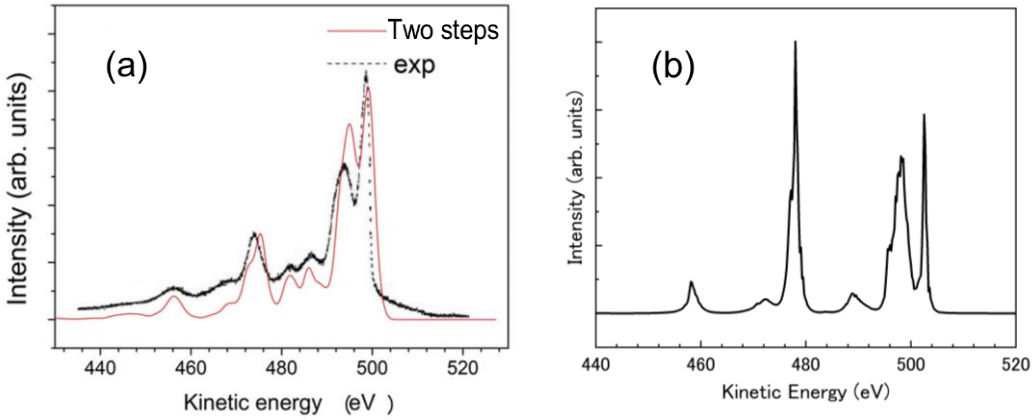

FIGURE 2. AES spectrum of single molecule of H_2O.
(a) Theoretical (two steps model) and experimental spectra[3],
(b) Theoretical spectrum with SCKH method.

In summary, this study established a method for XES that significantly reduces the computational cost while maintaining high accuracy. For the AES, the introduction of the SCKH formula enabled a physically reasonable spectral description. These results provide a new framework for the theoretical analysis of spectroscopic methods, including inner-shell collapse processes, that balances practicality and precision.

REFERENCES

1. Hirao et al. *J. Chem. Phys*., **155**, 034101 (2021).
2. Rubensson et al., *J. Chem. Phys*., **55**, 2317(1985)
3. Takahashi et al. *J. Phys. B: At. Mol. Opt. Phys*., **48**, 204001 (2015)

Analysis of Hydration Structures in Inorganic Salt Solutions using Molecular Dynamics and Molecular Orbital Methods

Ayana Sato [a], Osamu Takahashi [b]

[a] *Chemistry Program, Graduate School of Advanced Science and Engineering, Hiroshima University.*
[b] *Research Institute for Synchrotron Radiation Science, Hiroshima University.*

Keywords: Molecular dynamics (MD) simulation, soft X-ray emission spectroscopy (XES), computational chemistry

Water treatment membranes have traditionally been understood using the molecular sieving principle. However, recent experiments using liquid-crystal polymer membranes have shown that $MgSO_4$ exhibits higher permeability than NaCl, suggesting that ion-selective transport is significantly influenced by the stability of the hydrogen bonds surrounding the ions [1]. X-ray Emission Spectroscopy (XES) further indicated a high structural similarity between the water within the membrane and $MgSO_4$ hydration water; however, the precise nature of these hydration structures remains unclear. This study aims to clarify how ions modify water networks using Molecular Dynamics (MD) simulations and theoretical XES calculations.

MD simulations were performed using GROMACS for NaCl and $MgSO_4$ solutions up to the saturation concentrations. The systems were equilibrated for 2 ns using NVT and NPT ensembles, followed by hydrogen-bond analysis [2] to investigate the water orientation and structural deviations from pure water within each ion's hydration sphere. Furthermore, theoretical XES spectra were calculated for 20-molecule clusters sampled from the MD trajectories, specifically focusing on 1M/4M concentrations and the first hydration spheres of each ion.

Hydrogen bond analysis revealed that the structural modifications were most prominent in the first hydration sphere [2]. For cations, Mg^{2+} showed a significantly higher proportion of hydrogen-donating water molecules than Na^+. As confirmed by the radial distribution functions, the divalent nature of Mg^{2+} results in shorter ion-water distances, which sterically hinders water molecules from acting as hydrogen acceptors. Theoretical XES results showed that increasing the salt concentration broadens the $1b_1'$ peak and increases its intensity, reflecting ion-induced structural distortions in the water network. In NaCl solutions, the $1b_1'$ intensity was higher in the first hydration sphere than that in the bulk. This enhancement is likely due to the formation of linear hydrogen bonds associated with fast dynamics [3], a trend that is more pronounced for Cl^- than for Na^+. While the cations showed little difference between the two salts, the $1b_1'/1b_1''$ relative intensities for the anions shifted significantly. This suggests that SO_4^{2-} interacts with water via slower dynamics than Cl- because of its larger size and greater ion-water distance.

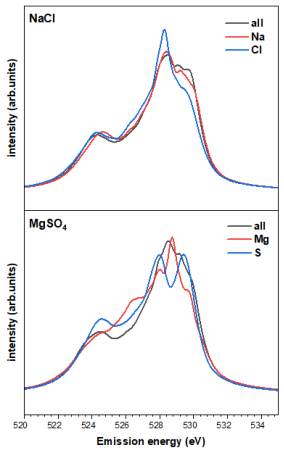

FIGURE 1. XES spectra of NaCl (upper) and MgSO4 (lower) aqueous solutions

REFERENCES

1. R. Watanabe et al., "Ion Selectivity of Water Molecules in Subnanoporous Liquid-Crystalline Water-Treatment Membranes: A Structural Study of Hydrogen Bonding" *Angew. Chem.*, **59**, 23461 (2020).
2. Ph. Wernet et al., "The Structure of the First Coordination Shell in Liquid Water" *Science*. **304** 5678 (2004).
3. O. Takahashi et al., "Interpretation of the X-Ray Emission Spectra of Liquid Water through Temperature and Isotope Dependence" *Phys. Rev. Lett.* **128** 086002 (2022).

Semiclassical Kramers-Heisenberg Calculations of Soft X-ray Emission Spectroscopy at the First Resonant Excitation

Hikari Sato[a] and Osamu Takahashi[b]

[a] *Graduate School of Advanced Science and Engineering, Hiroshima University.*
[b] *Research Institute for Synchrotron Radiation Science, Hiroshima University.*

Keywords: resonant inelastic soft X-ray scattering (RIXS), Computational chemistry

In our laboratory, various X-ray spectroscopic calculations have been performed on liquid systems. In this study, we performed resonant inelastic soft X-ray scattering (RIXS) calculations for liquid methanol, which serves as a prototypical hydrogen-bonded liquid.

In soft X-ray spectroscopy, particularly for systems containing second-row elements, it is essential to consider the dynamic effects of intermediate core-hole states. The Kramers-Heisenberg approximation describes the RIXS process by unifying the absorption of an incident photon and the subsequent X-ray emission associated with valence-core transitions. To account for vibrational effects while keeping the computational costs low, we used the semiclassical Kramers-Heisenberg (SCKH) approximation [1].

$$\sigma(\omega,\omega') = \frac{\omega'^{\Gamma_f}}{\omega\pi}\sum_f \left\langle F_{if}^{+}(\omega,\omega'-\omega)F_{fi}(\omega,\omega'-\omega)\right\rangle \quad (1)$$

$$F_{fi}(\omega,\omega'-\omega) = -i\alpha\sum_n \frac{\widetilde{D}_{ni}(R)}{\omega - E_{ni}(R) + i\Gamma}\left(\int_0^\infty dt'\widetilde{D}_{fn}^{+\prime}(t')e^{i\int_0^{t'} d\tau E_{nf}(\tau)}e^{-i[\omega-E_{ni}(R)]t'}e^{-\Gamma_f t'}e^{i\omega' t'}\right) \quad (2)$$

To model the liquid methanol, we performed classical molecular dynamics simulations and extracted 20 representative molecular cluster models. We then calculated the electronic structures of these clusters and the RIXS spectra using the SCKH method.

The spectrum near the first resonant excitation obtained by theoretical calculations reproduced the peak structure in the experimental values from previous studies [2], confirming the validity of the calculation model.

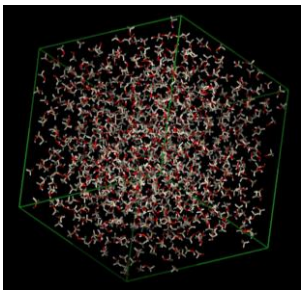

Figure. 1. Liquid methanol model based on MD simulation

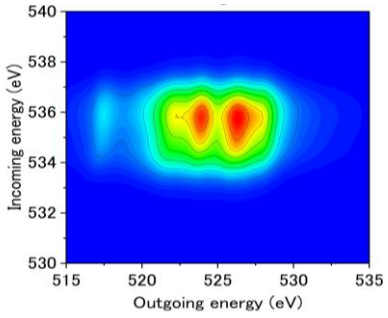

Figure2. RIXS map of the 20-mer in liquid methanol.

REFERENCES

1. M P. Ljungberg, Phys. Rev. B 96, 214302 (2017).
2. S Schreck *et al*, Struct. Dyn.1, 054901 (2014).

The electronic structure of 18-crown-6/acetonitrile/metal salt observed by soft X-ray absorption spectroscopy

Yuki Shiro[a, b], Osamu Takahashi[c], Masaki Oura[b], Masanari Nagasaka[d, e] and Yuka Horikawa[a, b]

[a]*Graduate School of Science and Technology for Innovation, Yamaguchi University 1677-1 Yoshida, Yamaguchi, Yamaguchi 753-8512 Japan*
[b]*RIKEN SPring-8 Center, Soft X-ray Spectroscopy Instrumentation Unit, Hyogo 679-5148 Japan*
[c] *Research Institute for Synchrotron Radiation Science, Hiroshima University 1-3-1 Kagamiyama, Higashi-Hiroshima, Hiroshima 739-8526 Japan*
[d] *Institute for Molecular Science, Myodaiji, Okazaki, Aichi 444-8585 Japan*
[e] *Graduate Institute for Advanced Studies, SOKENDAI, Myodaiji, Okazaki, Aichi 444-8585 Japan*

Keywords: 18-crown-6, X-ray absorption spectroscopy.

Crown ethers are a class of cyclic polyethers known for their ability to selectively encapsulate metal ions based on their molecular size and structure. It is well established that 18-crown-6 preferentially binds potassium ions (K^+), as the ionic diameter of K^+ (0.26 nm) closely matches the cavity size of the ether (0.3 nm). However, this selectivity is primarily observed in aqueous solutions; in the gas phase, complexes formed with smaller metal ions exhibit higher stability. Jing et al. investigated the potential energies of complex formation between 18-crown-6 and alkali metal ions (Li^+, Na^+, K^+, Rb^+, Cs^+) in both aqueous and gas phases using molecular dynamics (MD) simulations and quantum chemical calculations [1]. They reported that while the binding free energy is lowest for K^+ in water—supporting size-match selectivity—the potential energy in a vacuum is lowest for Li^+, indicating that smaller ions are trapped more strongly in the absence of solvent. This discrepancy arises because, in a vacuum, the ether ring distorts to wrap around the ion, maximizing stability for the smallest ion, Li^+ (0.14 nm). In contrast, in aqueous environments, the strong hydration energy of Li^+ prevents the formation of stable 18-crown-6 complexes. These findings demonstrate that the metal ion selectivity of crown ethers cannot be explained solely by the cavity size of 18-crown-6; it requires a comprehensive consideration of total energetic stability, including the solvent environment and the structural role of solvent molecules.

This study aims to elucidate the origin of ion selectivity from the perspective of electronic states. We experimentally investigated the molecular structures and electronic states of crown ether complexes in various solutions. Specifically, soft X-ray spectroscopy was performed on 18-crown-6 systems containing mixtures of different metal ions to observe how variations in ionic composition affect the electronic state of the host molecule. In addition, crystallized samples were also used to confirm the molecular structure.

Soft X-ray absorption spectroscopy (XAS) measurements were performed at SPring-8 BL17SU and UVSOR BL3U. At SPring-8, the generated crystals were placed under vacuum, and absorption spectra were measured using the fluorescence yield method. At UVSOR, measurements were conducted on the supernatant solution pumped into a liquid flow transmission cell.

Theoretical absorption spectra were calculated via Density Functional Theory (DFT) using the deMon2k code. To evaluate the dependence on the encapsulated ion, calculations were performed by substituting the metal ion type while maintaining an identical host geometry (**FIGURE 1**).

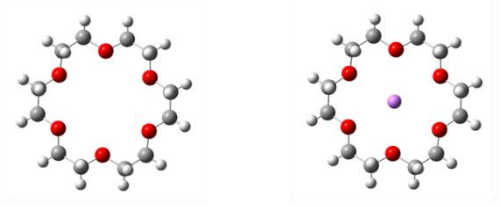

FIGURE 1. Structure of the 18-crown-6/metal ion complex used in the calculation.

The left panel of Figure 2 shows the soft X-ray absorption spectra at the oxygen K-edge for each crystal measured at SPring-8 BL17SU. In addition to the samples containing the four metal salts, a reference spectrum of an 18-crown-6/AN mixed crystal without metal salts is included. Resonance peaks were observed in all samples, exhibiting peak shifts dependent on the valence of the mixed metal ions. However, given the high deliquescence of the crystals and the limited soft X-ray penetration depth (~1 μm), the possibility remains that the spectra reflect 18-crown-6 in a liquid phase on the crystal surface.

The right panel of Figure 2 presents the calculated absorption spectra. The onset position of the main peak shifts to higher energies in the order: metal-free < encapsulated monovalent ion < encapsulated divalent ion. This trend is in qualitative agreement with the experimental shifts, suggesting that the observed peak shifts likely originate from interactions between 18-crown-6 and the metal ions. However, regarding the peak observed near 532 eV in the experiment, only the structure with Mg ions reproduced this feature, while other structures did not. This implies that the ion-containing structures of the 18-crown-6 being measured is not uniform like the structure in Figure 1.

In this presentation, we will report DFT results exploring candidate structures for 18-crown-6/metal ion complexes that account for the 532 eV peak observed at SPring-8. Additionally, we will present results from UVSOR measurements of absorption spectra for 18-crown-6 interacting with ions in the liquid phase.

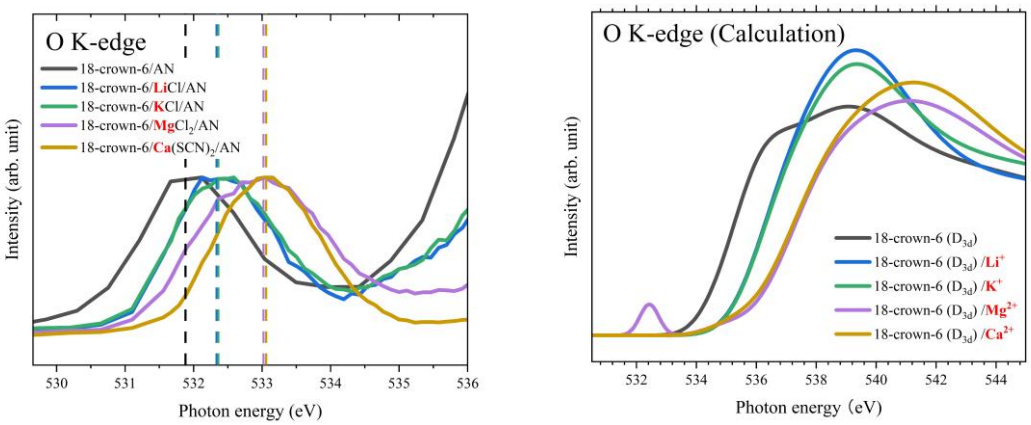

FIGURE 2. Oxygen K-edge soft X-ray absorption spectra of 18C6/AN mixture and 18C6/AN/metal salt mixture (left panel) and calculation results of oxygen K-edge soft X-ray absorption spectra (right panel).

REFERENCES

1. Z. F. Jing *et al. J. Mol. Liq.* **311**, 113305 (2020).

Synchrotron X-ray Studies on Structure and Electronic States of WO_3 Thin Films for Electrochromic Application

Sakshi Tyagi[a], Asokan Kandasami[a], Senthil Kumar Muthusamy[b]

[a]*School of Advanced Engineering, University of Petroleum and Energy Studies, Dehradun, Uttarakhand, India, 248007*
[b] *CSIR- National Physical Laboratory, New Delhi, India, 110012*

Tungsten oxide (WO_3) has gained greater attention for its electrochromic properties in both amorphous and crystalline states, enabling rapid coloration and bleaching times with high coloration efficiency [1]. It is an n-type semiconductor having a wide band gap (2.6-3.0 eV). It exhibits different phases, but it shows exceptional stability in monoclinic and hexagonal phases at room temperature [2]. In this work, WO_3 thin films were prepared using the pulsed laser deposition (PLD) technique with different laser shots, such as 2000 (W_2), 4000 (W_4) and 6000 (W_6), and then were studied for electrochromic applications. It is found that the W_2 film exhibits the highest coloration efficiency of 10.4 cm^2/C.

To study the structural, chemical, and electronic properties of the material at atomic and molecular levels, synchrotron-based grazing-incidence X-ray diffraction (GIXRD) and X-ray photoelectron spectroscopy (XPS) were performed on the PLD-deposited WO_3 thin films at NSSRC, Taiwan. The GIXRD results reveal that these thin films retain the monoclinic phase before and after testing the electrochromic characteristics. The monoclinic phase of WO_3 has a deformed structure and high coloration efficiency. The XPS data were critically analyzed to find the chemical composition and valence band edge of WO_3. W 4f core-level spectra indicate the presence of multiple valence states and oxygen vacancies [3]. Deconvoluted O 1s spectra show the presence of lattice and chemisorbed oxygen in the WO_3 thin films, which again confirms the presence of Oxygen vacancies in the films. The valence band spectra of these oxide thin films show the Fermi level (E_f) at ~3 eV, which indicates the n-type conductivity of the films. In addition, a small broad feature is observed from 0 to 2 eV, which is associated with the presence of oxygen vacancies [4]. W_2 sample shows a highly intense peak from 0 to 2 eV, which is evidence for the presence of oxygen vacancies in the respective film. More oxygen vacancies enhance the electrochromic properties due to the existence of more defects and electronic states.

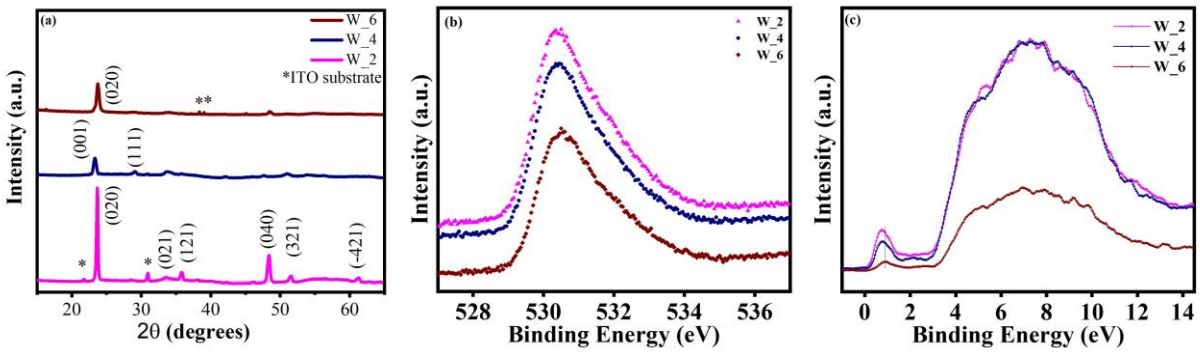

FIGURE. (a) Synchrotron GIXRD spectra, **(b)** O 1s core-level spectra, and **(c)** Valence band spectra of PLD-grown W_2, W_4, and W_6 thin films.

REFERENCES

1. J. Gupta and V. K. Gupta, *Versatility of various tungsten oxide nanostructures towards fostering electrochromic state of the art: a review*, Switzerland: Transition Metal Chemistry, 2025, pp. 345-347.
2. J. Gutpa, H. Shaik, K. N. Kumara and S. A. Sattar, *PVD techniques proffering avenues for fabrication of porous tungsten oxide (WO_3) thin films: A review,* United Kingdom: Materials Science in Semiconductor Processing, 2022, 106534.
3. X.G. Wang, Y.S. Jang, N.H. Yang, L. Yuan and S.J. Pang, *XPS and XRD study of the electrochromic mechanism of WO, films,* Netherlands: Surface and Coatings Technologies, 1997, pp. 82-86.
4. O. Bouvard, A. Krammer and A. Schüler, *In situ core-level and valence-band photoelectron spectroscopy of reactively sputtered tungsten oxide films,* New Jersey: Surface and Interface Analysis, 2016, pp. 660-663.

Analysis of multiple bosonic couplings in the self-energy of the high-Tc cuprate superconductor $La_{2-x}Sr_xCuO_4$ using Bayesian inference

Rikito Saiki[1], Masaharu Nozaki[1], Gunwoo Kim[1], Daiki Ootsuki[2], Shun Katakami[3], Masato Okada[3], Teppei Yoshida[1]

[1]*Graduate School of Human and Environmental Studies, Kyoto University, Sakyo, Kyoto 606-8501, Japan*
[2] *Research Institute for Interdisciplinary Science, Okayama University, Okayama 700-8530, Japan*
[3]*Graduate School of Frontier Sciences, The University of Tokyo, Kashiwa, Chiba 277-8561, Japan*

Keywords: ARPES, kink structure, Bayesian inference

To understand the mechanism of emergence of cuprate high-temperature superconductors, it is essential to clarify the interactions between electrons and bosons. In particular, the kink structure observed by angle-resolved photoemission spectroscopy (ARPES) has been regarded as a strong clue to electron–boson interactions [1–3]. However, there remains ongoing debate as to whether its origin is phonon in nature [2] or arises from magnetic interactions [3].

Lanzara *et al.* reported a universal kink structure appearing around 70 meV in Bi-based and La-based cuprate superconductors and suggested that it originates from electron–phonon coupling to the half-breathing phonon mode [2]. Furthermore, Zhou *et al.* performed high-resolution ARPES measurements on $La_{2-x}Sr_xCuO_4$ (LSCO) and investigated the kink structure in detail. By estimating the Eliashberg function $\alpha^2F(\omega)$ using the maximum entropy method (MEM), they demonstrated that electrons couple not to a single mode but to multiple phonon modes [4].

However, MEM has limitations in estimation accuracy, such as variations in the number and intensity of peaks in $\alpha^2F(\omega)$ depending on the choice of the prior function. In this study, we introduce Bayesian inference and determine the number of peaks by model selection based on the free energy. Figure 1 shows the real part of the self-energy, $\mathrm{Re}\Sigma$ of LSCO (x = 0.03) [5]. As a result, the model with the number of peaks (K = 3) yields both the minimum free energy and the maximum posterior probability, suggesting that three bosonic modes contribute to the kink structure. The three estimated peaks are located at approximately 31 meV, 51 meV, and 67 meV. By comparing these results with the phonon density of states obtained from first-principles calculations for La_2CuO_4 reported in previous studies [6], the physical origins of these bosonic modes can be interpreted as phonon. The peaks at about 51 meV and 67 meV are assigned to a bond-bending mode involving apical oxygen (LO_{2a} mode) and the oxygen bond-stretching phonon (LO_{1a} mode), respectively.

For the low-energy feature around 31 meV, two interpretations have been discussed in the literature. In Ref. [6], this peak is assigned to a low-energy mode (LE mode), whereas other first-principles studies report Cu–O bond-bending (buckling mode) in the energy range of 30–40 meV [7]. Therefore, the 31 meV peak may be attributed either to the LE mode proposed in Ref. [6] or to a buckling mode.

In this presentation, we report the results of a kink-structure analysis based on Bayesian inference and discuss the physical origins of these bosonic modes through comparison with previous studies.

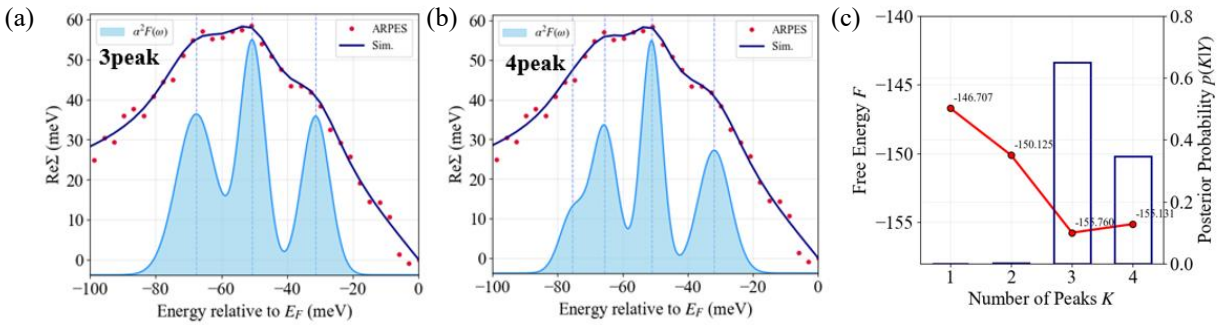

Figure 1.
(a), (b) Results of Bayesian fitting to the nodal-direction ReΣ(ω) of LSCO (x = 0.03) [5], assuming $\alpha^2F(\omega)$ with three peaks and four peaks, respectively.
(c) Results of model selection for the number of peaks (K) based on the Bayesian free energy (F) and the posterior probability (p).

REFERENCES

[1] A. Damascelli *et al*., Rev. Mod. Phys. **75**, 473 (2003).
[2] A. Lanzara *et al*., Nature **412**, 510 (2001).
[3] A. Kaminski *et al*., Phys. Rev. Lett. **86**, 1070 (2001).
[4] X. J. Zhou *et al*., Phys. Rev. Lett. **95**, 117001 (2005).
[5] T. Yoshida *et al*., Phys. Rev. B **80**, 245113 (2009).
[6] B. K. Chang *et al*., Phys. Rev. Research **7**, L012073 (2025).
[7] N. J. Jabusch, P. Dayal, and A. F. Kemper, SciPost Phys. Core **6**, 018 (2023).

Electronic structure of the Mott–Hubbard compound $SrVO_3$ studied by resonant photoemission spectroscopy

Gunwoo Kim[a], Chihiro Inoue[a], Masaaki Higashino[a], Daiki Ootsuki[b], Hiroshi Kumigashira[c], Shigeki Miyasaka[d], and Teppei Yoshida[a]

[a] *Graduate School of Human and Environmental Studies, Kyoto University, Sakyo-ku, Kyoto, Kyoto, 606-8501, Japan*
[b]*Research Institute for Interdisciplinary Science, Okayama University, 3-1-1, Tsushima-naka, Tsushima, Kita-ku, Okayama 700-8530, Japan*
[c]*Institute of Multidisciplinary Research for Advanced Materials (IMRAM), Tohoku University, Sendai 980-8577, Japan*
[d]*Department of Material Science, Graduate School of Science, University of Hyogo, Ako, Hyogo 678-1297, Japan*

Keywords: Vanadium Oxides, Resonant photoemission, Mott-Hubbard system.

$SrVO_3$ (SVO) is a Mott–Hubbard correlated metal in which strong on-site Coulomb repulsion U_{dd} splits the V $3d$ spectral weight into an itinerant coherent (quasiparticle) part and a localized incoherent (Hubbard-band) part. To elucidate the effects of strong electron correlations in many-electron systems, it is essential to investigate the coherent and incoherent components, which have been studied both experimentally [1] and theoretically [2]. In this context, Mossanek *et al.* [3] studied the influence of O $2p$–V $3d$ hybridization on the coherent and incoherent parts; their cluster-model calculations indicated that an O $2p$ contribution to the incoherent feature is crucial to reproduce photoemission spectra [4].

In this work, we investigated the electronic structure of SVO by performing resonant photoemission spectroscopy (RPES) at the V L-edge and the O K-edge, together with local-density-approximation (LDA) calculations. Figure 1 shows V L-edge RPES spectra and the LDA partial density of states (PDOS). By tuning the photon energy from $h\nu = 510.46$ to 519.46 eV, we observe a resonant enhancement of the spectral intensity. A comparison between the spectrum at $h\nu = 519.46$eV and the LDA PDOS reveals correlation-induced features that cannot be reproduced by LDA: a coherent feature (~ 0.17 eV) and an incoherent feature (~ 1.7 eV). In addition, a structure associated with O $2p$ states appears at ~ 3.7 eV, while features at ~ 5.8 and ~ 7.1eV are attributable to O $2p$–V $3d$ hybridized states. At higher binding energies, *LVV* Auger emission and shallow-core-level features are observed.

Figure 2(a) presents O K-edge RPES measured in the photon-energy range around the O K-edge. With increasing photon energy, a *KVV* Auger feature shifts toward higher binding energy (orange dashed line). Figures 2(b) and 2(c) compare the O K-edge x-ray absorption spectrum (XAS) with constant-initial-state (CIS) spectra taken at selected binding energies. The CIS spectra taken at the O $2p$ band and at O $2p$–V $3d$ hybridized-state binding energies closely follow the near-edge XAS peaks, whereas the CIS spectra taken at the coherent and incoherent energies do not. This behavior suggests that the coherent and incoherent features near Fermi level E_F have negligible O $2p$ character.

Finally, as shown in Fig. 2(d), we reproduced the *KVV* Auger line shape extracted from RPES using the Cini–Sawatzky formalism [5-6] combined with the LDA O $2p$ PDOS, yielding an estimate of the O $2p$ on-site Coulomb energy $U_{pp} = 5.6$ eV. While previous work [3] neglected U_{pp} and consequently inferred an O $2p$ contribution near E_F, our results indicate that a non-negligible U_{pp} suppresses O $2p$ states near E_F.

In this presentation, we will report the values of $U_{dd}(U_{pp})$ estimated from V L-edge (O K-edge) RPES and discuss characteristics of the electronic structure of SVO.

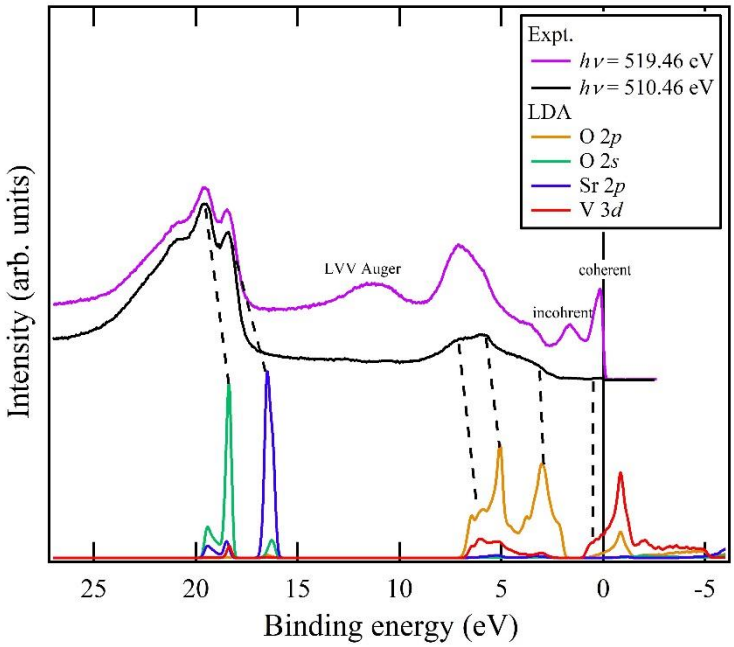

FIGURE 1. Comparison between V *L*-edge RPES spectra and the LDA-calculated PDOS of SVO.

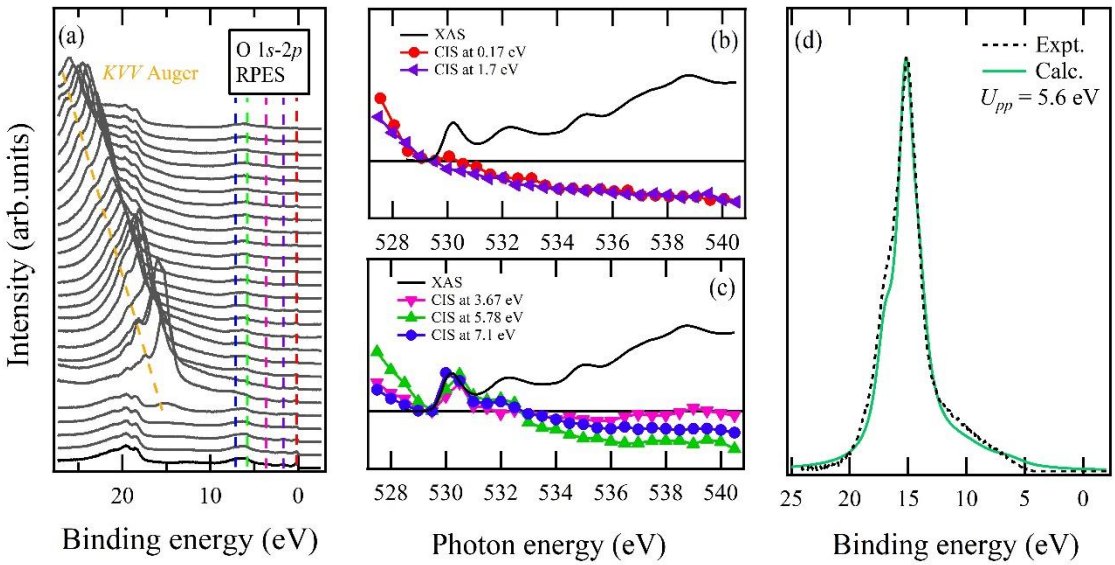

FIGURE 2. (a) O *K*-edge RPES spectra of SVO. (b), (c) Comparison of the O K-edge XAS spectrum with CIS spectra extracted from the RPES data in Fig. 2(a) at selected binding energies (indicated by vertical dashed lines). (d) Comparison of the *KVV* Auger line shape extracted from RPES with the Auger line shape calculated using the Cini–Sawatzky formalism combined with the LDA-calculated O 2*p* PDOS. The value of U_{pp} used in the calculation is 5.6 eV.

REFERENCES

1. S. Aizaki, T. Yoshida, K. Yoshimatsu, M. Takizawa, M. Minohara, S. Ideta, A. Fujimori, K. Gupta, P. Mahadevan, K. Horiba, H.Kumigashira, and M. Oshima, Phys. Rev. Lett. **109**, 056401 (2012).
2. I.A. Nekrasov, K. Held, G. Keller, D.E. Kondakov, T. Pruschke, M. Kollar, O.K. Andersen, V.I. Anisimov, and D. Vollhardt, Phys. Rev. B **73**, 155112 (2006).
3. R. J. O. Mossanek, M. Abbate, T. Yoshida, A.Fujimori, Y. Yoshida, N. Shirakawa, H. Eisaki, S. Kohno, P.T. Fonseca, and F.C. Vicentin, Phys. B **79**, 033104 (2009).
4. K. Morikawa, T. Mizokawa, K. Kobayashi, A. Fujimori, H. Eisaki, S. Uchida, F. Iga, and Y. Nishihara, Phys. B **52**, 13711 (1995).
5. M. Cini, Solid State Communications **20**, 605 (1976); **24**, 681-684 (1977); Phys. Rev. B **17**, 2788 (1978).
6. G. A. Sawatzky, Phys. Rev. Lett. **39**, 504 (1977).

Band structure of chiral magnet Yb(Ni,*M*)$_3$Al$_9$ (*M*=Pd,Pt) observed by ARPES

Y. Murakami[a], Y. Tanimoto[b], Y. Nakashima[b], K. Kimura[b], H. Sato[c], K. Tanaka[d], K. Yamagami[e], S. Nakamura[f], S. Ohara[f]

[a]*Faculty of Science, Hiroshima University, Higashi-Hiroshima 739-8526, Japan*
[b]*Graduate School of Advanced Science and Engineering, Hiroshima University, Higashi-Hiroshima 739-8526, Japan*
[c]*Hiroshima Research Institute for Synchrotron Radiation Science, Hiroshima University, Higashi-Hiroshima 739-0046, Japan*
[d]*UVSOR synchrotron Facility, Institute for Molecular Science*
[e]*Japan Synchrotron Radiation Research Institute*
[f]*Japan Graduate School of Engineering, Nagoya Institute of Technology*

Keywords: chiral magnetic crystal, helical magnetism, angle resolved photoemission spectroscopy

Trigonal $YbNi_3Al_9$ with a chiral crystal structure is of interest as the first chiral magnetic metal discovered among 4*f* electron systems [1]. The localized Yb 4*f* moments are magnetically ordered below T=3.4 K, ferromagnetically aligned within the *c*-plane, and exhibit either left-handed or right-handed helical magnetic structures with a propagation vector $\boldsymbol{q}$=(0, 0, 0.8) along the c-axis [2]. Owing to its chiral crystal structure, spin splitting in the conduction-electron band structure is expected, which is considered to play an essential role in the emergence of chiral magnetism. Furthermore, partial substitution of Ni with the heavier isovalent elements Pd and Pt is anticipated to enhance the spin splitting due to the increased spin-orbit interaction. In this study, we performed vacuum ultraviolet angle-resolved photoemission spectroscopy (VUV-ARPES) and soft X-ray angle-resolved photoemission spectroscopy (SX-ARPES) on $YbNi_3Al_9$ and its 5% substituted compounds, $Yb(Ni_{0.95}Pd_{0.05})Al_9$ and $Yb(Ni_{0.95}Pt_{0.05})Al_9$, to investigate the electronic structure near the Fermi level (E_F). The VUV-ARPES and SX-ARPES measurements were carried out at BL7U of UVSOR-III and BL25SU of SPring-8, respectively. Single crystals used for the measurements were synthesized by the flux-method [3]. First-principles band-structure calculations were carried out using the WIEN2k code [4], and the results were compared with the experimental data.

At $h\nu$ = 24 eV and T = 10 K, VUV-ARPES spectra of $YbNi_3Al_9$ measured with *s*-polarized light along the $\bar{\Gamma}$-$\bar{M}$ direction reveal two hole-like bands crossing E_F and an upward-convex parabolic band centered at the $\bar{\Gamma}$ point. Similar band dispersions were observed for $Yb(Ni_{0.95}Pd_{0.05})Al_9$ and $Yb(Ni_{0.95}Pt_{0.05})Al_9$. Within the experimental accuracy, no clear enhancement of the spin-splitting width was detected upon Pd or Pt substitution, which is likely due to the relatively small substitution level (5%). The Fermi surface of $YbNi_3Al_9$ measured at $h\nu$ = 510 eV and T = 70 K using circularly polarized light consists of at least two sixfold-symmetric hole sheets centered at the $\bar{\Gamma}$ point and electron sheets around the $\bar{K}$ points. The overall band dispersions and Fermi-surface topology are qualitatively reproduced by the band calculations. A comparison with calculations for the hypothetical compound $YbPt_3Al_9$ indicates that the spin splitting is significantly enhanced in the outermost hole band around the $\bar{\Gamma}$ point, suggesting that stronger spin-orbit coupling can substantially modify the conduction-band spin splitting.

REFERENCES

1. S. Ohara, S. Fukuta, K. Ohta, H. Kono, T. Yamashita, Y. Matsumoto and J. Yamaura, JPS Conf. Proc. **3**, 017016 (2014).
2. T. Matsumura, Y. Kita, K. Kubo, Y. Yoshikawa, S. Michimura, T. Inami, Y. Kousaka, K. Inoue and S. Ohara, J. Phys. Soc. Jpn. **86**, 124702 (2017).
3. T. Yamashita, R. Miyazaki, Y. Aoki and S. Ohara, J. Phys. Soc. Jpn. **81**, 034705 (2012).
4. P. Blaha, K. Schwarz, F. Tran, R. Laskowski, G. K. H. Madsen and L. D. Marks, J. Chem. Phys. **152**, 074101 (2020).